



Star Formation in the Magellanic Clouds based on 1.2 mm Continuum Observations

Dissertation

zur Erlangung des Grades

Doktor der Naturwissenschaften

Fakultät für Physik und Astronomie

Ruhr-Universität Bochum

von

Elisa Merkel Ferreira

aus Recife, Brasilien

Bochum 2004

This Ph.D. thesis has been created using LATEX 2 ϵ and the Editor Kwrite from LINUX.
The printed version has been formatted using dvips.

Ph.D. thesis supervisor: Prof. Dr. Rolf Chini

Second referee: Prof. Dr. Ulrich Mebold

For my parents and my grandmother

"The Earth is the cradle of mankind,
but a man cannot stay in the cradle forever."

Konstantin Ziolkowskij

Contents

| | | |
|----------|---|-----------|
| 1 | Introduction | 2 |
| 1.1 | The Magellanic System | 2 |
| 1.1.1 | The Large Magellanic Cloud | 5 |
| 1.1.2 | The Small Magellanic Cloud | 6 |
| 1.2 | Star Formation | 7 |
| 1.3 | The Interstellar Medium | 12 |
| 1.3.1 | Molecular gas | 13 |
| 1.3.2 | Dust | 15 |
| 1.3.3 | Gas-to-dust ratio | 19 |
| 1.4 | Outline of this Current Ph.D. Thesis | 20 |
| 2 | Data and Reduction | 21 |
| 2.1 | Sample Selection | 21 |
| 2.2 | Telescope | 22 |
| 2.3 | Bolometer Array | 23 |
| 2.4 | Submillimeter Observations | 24 |
| 2.5 | MOPSI | 27 |
| 2.6 | Contamination of Continuum Flux | 30 |
| 2.7 | IRAS Data | 31 |
| 3 | Dust Observations in the LMC | 33 |
| 3.1 | Observed Regions in the LMC | 33 |
| 3.1.1 | 30 Doradus | 33 |
| 3.1.2 | Observations in the 30 Doradus central area | 37 |
| 3.1.3 | 30 Doradus southern HII regions | 42 |
| 3.1.4 | Detections and non-detections in the 30 Dor complex | 47 |

| | | |
|----------|--|-----------|
| 3.1.5 | N 44 emission nebula | 49 |
| 3.1.6 | N 113 nebula | 52 |
| 3.1.7 | N 214 nebula | 53 |
| 3.2 | Results | 54 |
| 3.2.1 | Temperatures | 54 |
| 3.2.2 | Masses | 60 |
| 4 | Dust Observations in the SMC | 63 |
| 4.1 | Observed Regions in the SMC | 63 |
| 4.1.1 | N 12 | 64 |
| 4.1.2 | H 15 | 65 |
| 4.1.3 | N 27 | 66 |
| 4.1.4 | N 66 | 67 |
| 4.1.5 | N 76 | 68 |
| 4.1.6 | N 81 | 69 |
| 4.1.7 | N 83 - 84 | 70 |
| 4.1.8 | N 88 | 72 |
| 4.2 | Results | 73 |
| 4.2.1 | Temperatures | 73 |
| 4.2.2 | Masses | 76 |
| 5 | Gas-to-dust Ratio R in the LMC and the SMC | 78 |
| 5.1 | Gas-to-dust Ratio R in the LMC | 81 |
| 5.2 | Gas-to-dust Ratio R in the SMC | 84 |
| 5.3 | R Estimate through Indirect Method | 85 |
| 6 | Star Formation Efficiency in the LMC and the SMC | 87 |
| 6.1 | FIR Luminosity versus Molecular Mass in the LMC | 87 |
| 6.2 | FIR Luminosity versus Molecular Mass in the SMC | 91 |
| 6.3 | Star Formation Efficiency versus Dust Temperature | 91 |
| 6.4 | Star Formation Efficiency from FIR and $H\alpha$ | 93 |
| 6.5 | Final Remarks | 94 |
| 7 | Summary and Outlook | 96 |
| 7.1 | Summary | 96 |

| | |
|--|------------|
| <i>CONTENTS</i> | vii |
| 7.2 Outlook | 97 |
| A Reduction of the Bolometer Data | 99 |
| References | 105 |
| Acknowledgements | 113 |
| Curriculum Vitae | 114 |

Abstract

This thesis reports on results of a large 1.2 mm survey of the Magellanic Clouds. Prominent star forming regions have been investigated for the first time at 1.2 mm with the 37 channel bolometer array SIMBA by using the fastscanning observing technique. The obtained data were reduced with the MOPSI software package. The present thesis concentrates on the detection of cool dust, which may best be found inside the molecular clouds. For this purpose, the investigations were concentrated towards the positions of a sample of CO clouds. The here performed study shows in which way the cool dust exists under the different physical conditions of these dwarf irregular galaxies. Apart from positions and flux densities, spectral energy distributions (SEDs) have been determined allowing, through the fitting of modified Planck functions, the derivation of dust temperatures and dust masses. The gas-to-dust ratios and the star formation efficiencies have been obtained for the detections in this study.

The study comprises 40 dust clouds of which 33 are located in the LMC, while 21 of them being associated with the 30 Dor complex. The eight mosaics in the LMC cover selected areas in the 30 Dor central field and its southern HII regions associated with molecular clouds; these regions have been previously investigated by the ESO-SEST Key Programme: *CO in the Magellanic Clouds*. In addition, a few other HII regions have also been studied. In the SMC, the SIMBA survey was also based on the same ESO-SEST Key Programme towards selected regions in the SW Bar (where a large CO complex is located), in the northern Bar and in the Shapley Wing. All 40 sources investigated in the LMC and SMC have been detected for the first time at 1.2 mm.

The molecular gas-to-dust ratios of the different sources show a high dispersion through the individual regions of both Magellanic Clouds. The variations in the molecular gas-to-dust mass ratio in the LMC show east-west and north-south asymmetries, bimodal behavior and correlation with the cloud size depending on the analyzed region. In the SMC, similarities in two regions of the SW Bar are found. A substantial variation in the star formation efficiency within a galaxy reflects the temporal evolution of star forming regions in molecular cloud complexes or localized bursts of star formation and is very well seen in the LMC. The highest activity stage in the LMC is found in 30 Dor A, while regions outside the 30 Dor complex such as N 44 present on average much lower SFE values. In contrast, all studied regions in the SMC show a fairly low SFE.

Chapter 1

Introduction

1.1 The Magellanic System

The Magellanic System comprises two galaxies, the Large Magellanic Cloud (LMC) and the Small Magellanic Cloud (SMC), the InterCloud or Bridge region and the Magellanic Stream (Fig. 1.1).

The Magellanic Clouds (MCs) are satellite galaxies of the Milky Way located in the southern sky at circumpolar position. They were surely been known since the earliest times by the inhabitants of the Southern Hemisphere. The first preserved mention from the LMC dates from 964 by the Persian astronomer Al Sufi. The name Magellanic Clouds comes from the fact that in 1520, during the first circumnavigation, they were described by the chronicler Pigafetta of Fernao de Magalhaes e Sousa, whose crew used them as a rough navigation tool while sailing through the Southern Hemisphere (Fig. 1.2).

The LMC, the SMC and the Galaxy should not be considered independently. They form a triple system, interacting in such a way that in billions of years the MCs will be completely destroyed by the Milky Way. The fact that the Clouds have a common envelope of neutral hydrogen (HI) indicates that they have been gravitationally bound for long time. It is also in general assumed that these galaxies have been bound to the Milky Way for at least the last 7 Gyr (Westerlund 1997).

They are the nearest dwarf irregular galaxies, members of our Local Group of galaxies, containing millions of stars and possibly planets. Owing to their close proximity, nearly face-on view and small extinction, the MCs have been extensively observed at nearly all wavelengths, making them a very good site to study star formation and interstellar structures in detail. They are valuable for comparison with the quite different conditions in the Milky Way.

The LMC is of type SB(s)m and the SMC of type SB(s)mp (Westerlund 1997) having low luminosities (classes III-V) and are characterized by low dust and low heavy-element abundances as well as by high oxygen-to-carbon ratios in HII regions, high atomic-to-molecular hydrogen ratios and intense radiation at UV and FUV wavelengths.

A complete IR survey of the MCs was first obtained by the Infrared Astronomical Satellite

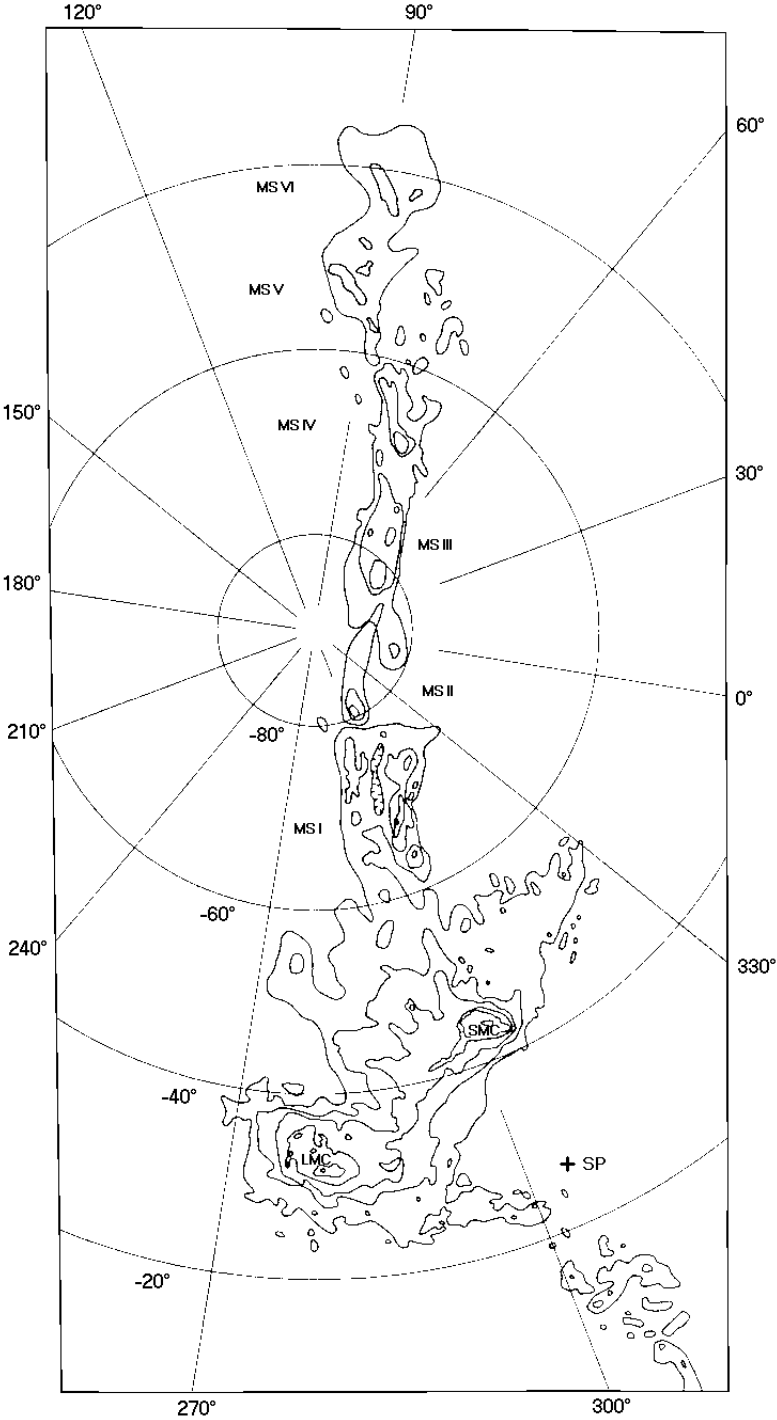


Figure 1.1: HI distribution in the Magellanic System in galactic coordinates (Mathewson & Ford 1984).



Figure 1.2: LMC (bottom left), SMC (top left) and the Milky Way, as seen from Cerro Tololo in Chile (CTIO homepage).

(IRAS) at the wavelengths of 12, 25, 60 and 100 μm . For the LMC 1823 and the SMC 219 infrared sources were listed. They show in general a good correlation with the distribution of HII regions and dark clouds (Schwering 1988). As a result from the analysis of the IRAS data, it may be concluded that the average MCs dust is hotter than that of the Milky Way, due to a high UV interstellar radiation field and a low heavy element abundance in the Clouds.

Kennicutt & Hodge (1986) estimated the total star formation to be 0.14 M_{\odot}/yr and 0.038 M_{\odot}/yr in the LMC and SMC, respectively. The total masses of LMC and SMC are, $2 \times 10^{10} M_{\odot}$ and $2 \times 10^9 M_{\odot}$, respectively (Westerlund 1997). Dufour (1984) found for the oxygen abundance (Galaxy:LMC:SMC) the ratio 1:0.5:0.2 and for the carbon abundance the ratio 1:0.3:0.05. Pei (1992) estimated for the Milky Way, the LMC and the SMC the proportions of the abundance of heavy elements of 1:0.333:0.125, of the strength of the 2175 \AA feature in the extinction curve of 1:0.5:0.125, of the strengths of the FIR extinction of 1:2:3 and of the FUV extinction of 1:2:3. The radial velocity of the LMC is 245 km s^{-1} and that of the SMC 140 km s^{-1} (Savage & de Boer 1981). In the LMC Koornneef (1982) derived $N(\text{HI})/E(\text{B-V}) = 2 \times 10^{22} \text{ atoms cm}^{-2} \text{ mag}^{-1}$ and in the SMC Bouchet et al. (1985) obtained $N(\text{HI})/E(\text{B-V})$ in the range 3.7 to 5.2 $\times 10^{22} \text{ atoms cm}^{-2} \text{ mag}^{-1}$, which correspond, respectively, to a factor of four higher and about eight times the Galactic value.

The dominating feature of the InterCloud region is the bridge of gas connecting the SMC with the LMC, which is a clear evidence for tidal interaction between both galaxies (Mathewson & Ford 1984). The age of many of the stellar concentrations (10 - 25 Myr) in the Bridge region indicates that it is a star forming site (Heydari-Malayeri et al. 2003).

The Magellanic Stream (MS) was discovered in 1973 by Mathewson. This trail, an essentially continuous filament behind the MCs and around the Milky Way, extends about 100° from the InterCloud region, is thought to be about 160000 light years long and is surrounded by very hot gas from the Milky Way's Halo. The MS is composed by discrete clumps of gas that consists primarily of neutral hydrogen originated from the LMC and SMC as a result of the tidal interactions with the Galaxy. No stars are known to be associated with the MS.

1.1.1 The Large Magellanic Cloud

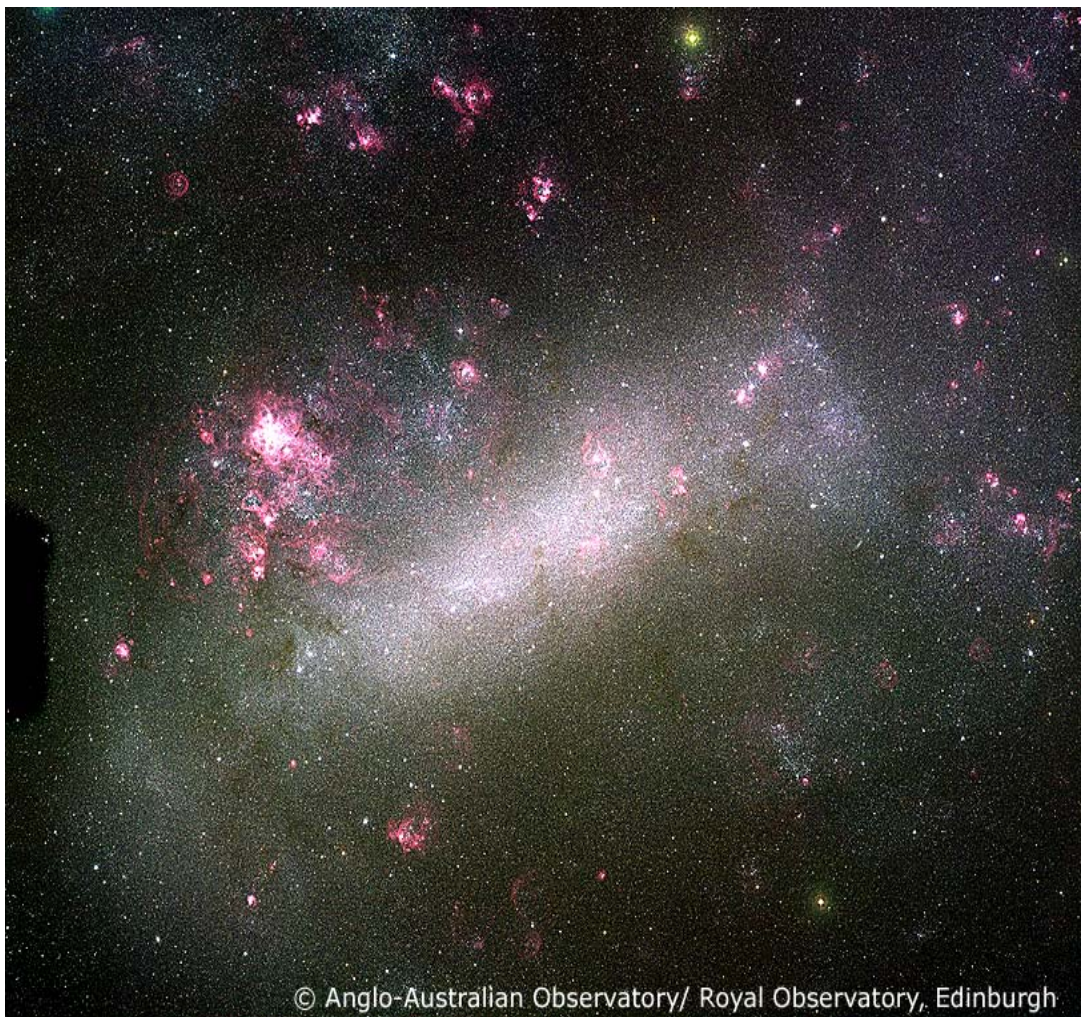


Figure 1.3: The LMC with at its eastern end the star-forming region 30 Doradus.

The LMC, at a distance of 50 kpc, is located in the constellation Dorado (the Goldfish or the Swordfish) and has an optical diameter of about 7° . The basic feature of its structure, determined on the basis of optical and radio observations, is an elongated bar with its major axis in position angle of 120° (Fig. 1.3). This galaxy is full of interesting objects including diffuse and planetary nebulae, globular and open clusters. It was in the LMC that in 1987

was observed the supernova 1987A, the first "nearby" supernova in the last 3 centuries.

An explanation of the in general highly asymmetric distributions of gases in the LMC was given by Fujimoto & Noguchi (1990) as being the encounter between the LMC and the SMC at ~ 0.2 Gyr ago.

The distribution of HI revealed itself to be complicated. Meaburn et al. (1987) concluded that the HI sheets that they had detected and the nine supergiant shells (SGSs), which were observed in the LMC, could be separate consequences of the same process: star formation bursts through supernovae explosions and stellar winds in the expanding perimeters of the SGSs shape them out of the molecular/HI clouds; the successive supernovae explosions and the stellar winds could supply the needed energy for the HI motions away from the LMC plane. Luks & Rohlfs (1992) derived a rotation curve and found the center of rotation of the gas disk which extends over all LMC at 1.2° from the center of the bar. Beyond the gas disk they found another structural feature, the L-component which consists of two large complexes linked by 30 Doradus (30 Dor). Marx-Zimmer et al. (2000) found that in the LMC the HI clouds are either unusually cool ($T \approx 30\text{K}$) compared to the cool phase in the Milky Way ($T = 60\text{K}$) or the cool atomic phase is more abundant in the LMC (35% for $T = 60\text{K}$) relative to the warm neutral medium than in our Galaxy (24% for $T = 60\text{K}$). Excluding the star forming regions 30 Dor and LMC 4, for $T = 60\text{K}$ a similar mixture of warm and cool phases to the Milky Way is found.

Kennicutt & Hodge (1986) measured integrated $\text{H}\alpha$ fluxes in the MCs for several hundred HII regions. The HII regions span a range of 10^4 in luminosity, from compact regions to the 30 Dor complex. The faintest ones can be ionized by single stars and the majority by stellar associations and clusters. The extended networks of filaments in the LMC probably contribute 15% - 25% to the whole $\text{H}\alpha$ luminosity, being comparable to some of the largest HII regions. The 30 Dor complex is the most luminous HII region in the Local Group and it is surrounded by several other HII regions which are also among the brightest in this galaxy. The ionized gas in the 30 Dor is twice as luminous as the whole SMC (Westerlund 1997).

Surveys of CO in the LMC have been undertaken by Cohen et al. (1988) and by the ESO-SEST Key Programme: *CO in the Magellanic Clouds*. These surveys lead to the conclusion that in the 30 Dor area and its southern HII regions the most prominent CO clouds are associated with massive star formation and about 60% of the CO clouds with dark nebulae.

Whiteoak & Gardner (1986) searched for H_2O maser emission in the LMC and other nearby galaxies detecting only four masers towards about 80 HII regions of the LMC. The maser production is considerably lower in the LMC if compared with H_2O observations towards HII regions in our Galaxy, perhaps indicating a lower rate of star formation.

1.1.2 The Small Magellanic Cloud

The SMC, at a distance of 60 kpc, with an optical diameter of 3.5° , is located in the constellation Tucana (the Toucan). The most prominent features determined on the basis of optical and radio observations are an elongated bar with the position angle of 45° and an eastern wing. However the SMC structure is difficult to define. This comes from the fact that being the component with the lowest mass in the triple system SMC-LMC-Milky Way it is the most disrupted by the apparently gravitational nature of the interactions of the system. The

conditions in the SMC are similar to those of the LMC, but more pronounced - e.g. an even lower abundance of heavy elements, an even weaker feature around 2175 \AA in the extinction curve and even higher FIR and FUV extinction strengths.

In the SMC the youngest stars ($\leq 100 \text{ Myr}$) appear to be relatively evenly distributed in the bar and in the wing. Few stellar associations and only one superassociation with a well-defined supergiant shell has been identified, which is located in the wing (Westerlund 1997).

Results obtained from the 21 cm line radiation from neutral hydrogen by Hindman (1964) suggested differential rotation. From the fact that the HI profiles in the SMC were observed with two velocity components (which delineate separate entities, each one with own nebular and stellar population) Mathewson & Ford (1984) proposed that the SMC was torn during the near collision with the LMC at $\sim 0.2 \text{ Gyr}$ ago (Fujimoto & Noguchi 1990) and a large fragment, the Mini-Magellanic Cloud, is now separating from the remnant of the SMC. Other papers also worked on the HI profiles splitting (e.g. Caldwell & Coulson 1986). So the earlier interpretation as a whole rotating galaxy was replaced by the possibility of fragmentation. A 21 cm line mapping of neutral hydrogen of the SMC done by Staveley-Smith et al. (1995) revealed a structure of remarkable complexity with compact knots, filaments and numerous wind-blown shells. Dickey et al. (2000) found in the SMC a much lower abundance of cool phase gas. The abundance is about half that of the solar neighborhood and about one third that of the LMC (Marx-Zimmer et al. 2000). Only the regions with the highest pressures will be pushed into the cool phase. Therefore, in the SMC at cold temperatures and high densities, which in our Galaxy are the domain of only H_2 , the atomic gas may dominate. It may be that in the SMC the molecular phase can only survive at the highest densities, i.e., in the most heavily shielded cores of the densest clouds.

The SMC is, in relation to the LMC, deficient in large nebulae of high surface brightness (Westerlund 1997). The filamentary structure and diffuse emission in the SMC is less prominent than that of LMC, but observations done by Kennicutt et al. (1995) revealed an extended emission in the bar. Also large shells can be seen in the wing confirming results obtained by Torres & Carranza (1987). The latter reported in their $\text{H}\alpha$ observations several partially overlapping velocity groups showing a quite good velocity correlation with neutral gas.

Surveys of CO in the SMC undertaken by Rubio et al. (1991) and by the ESO-SEST Key Programme detected two large complexes, located in the southwestern and northeastern regions of the bar, which are associated with the most intense HI emission from this galaxy. The brightest sources are associated with intense, but small HII regions (Israel et al. 1993).

1.2 Star Formation

No observed star has existed forever. Thus it is needed to investigate how stars form (Fig. 1.4) and evolve.

The first stars were top-heavy ($10^2 - 10^3 M_{\odot}$). As the metallicity increases, the gas fragments down to much smaller clumps. Also the increased opacity of the envelope material leads to a range of stellar masses like those seen in the present-day Universe.

Bimodal star formation is the notion that the birth of low- and high-mass stars may involve

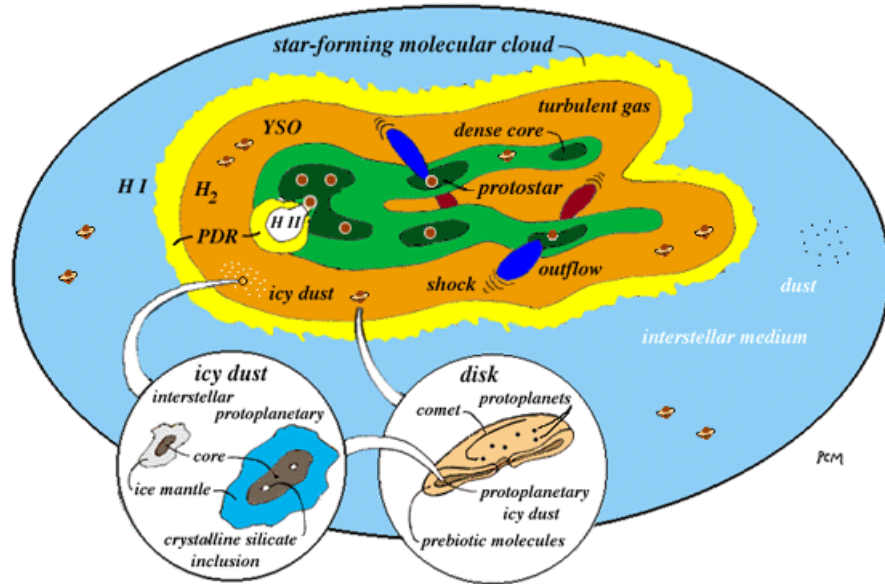


Figure 1.4: Star formation scheme (cfa-www.harvard.edu/sfgroup).

separate mechanisms. Observations show regions of molecular clouds where high- and low-mass stars are forming, and other regions where only the latter ones appear to form.

There are two classes of clouds: Giant Molecular Clouds (GMCs) and Dark Clouds. In general, in the former mainly massive stars (OB Associations) and in the latter mostly low-mass stars are formed. Molecular clouds are dense, cold condensations which are surrounded by less dense and hotter atomic gas (diffuse medium) (Chini 2002). The formation time for massive stars is shorter than for low mass ones. Herbig (1962) speculated that stars of low mass are born before those of high mass. However the idea of a temporal sequence in the formation of stars of different masses remains controversial. Mezger & Smith (1977) indicated that high-mass star formation takes place primarily in large cloud complexes within the spiral arms of the Galaxy whereas low-mass star formation is found to be smoothly distributed throughout the Galactic disk. Solomon & Sanders (1985) divided molecular clouds into cold and warm ones. The first ones do not contain stars earlier than late B and the latter ones are associated with HII regions.

The behavior of the initial-mass function is a possible indicator of the process of bimodal star formation. Scalo (1986) found two local maxima in the mass spectrum, one at $0.3 M_{\odot}$ and another at $1.2 M_{\odot}$. This was obtained for the solar neighborhood, star clusters and nearby galaxies.

Star-forming clouds can be generated by a series of different perturbations, e.g. the passage of spiral density waves, collisions among gas clouds, the energy injection of stars, interactions with other galaxies.

The lower mass limit of a massive star is defined as $8 M_{\odot}$. This limit is established due to three reasons: i) stars with $M < 8 M_{\odot}$ (B3V) do not emit Lyman continuum photons; ii) for initial stellar masses above $8 M_{\odot}$ there is no PMS phase i.e. the star ignites H-burning before

it finishes accumulating its final mass by accretion from protostellar gas, dust envelope or circumstellar disk; iii) $8 M_{\odot}$ is the dividing mass between the initial progenitor mass of white dwarfs and type II supernovae (Zinnecker 2003).

Four main stages of the low-mass star formation in molecular clouds can be established:

- Formation of a slowly rotating cloud core.
- Collapse of the core into a protostar (protostars can be defined as objects in the process of accumulating the bulk of the material, into a stellar-like configuration, they will ultimately contain when they reach the main sequence) and disk, deep within an infalling envelope of material.
- A stellar wind with collimated jets and a bipolar outflow.
- Sweeping away of the circumstellar material to reveal the YSO (the general class of protostellar and pre-main sequence (PMS) stars are called young stellar objects, YSOs) with consolidation of the disk into planets or companion stars.

The energy output of the YSOs is predominantly from reprocessed stellar light, which is originated from the dusty circumstellar environment of cocoons, shells or disks. Before becoming visible at the optical wavelength regime these objects show up as submillimeter and/or infrared sources, which depends on their evolutionary stage (Nielbock et al. 2001).

The birth of stars is also associated with Herbig-Haro (HH) objects, which now are known to be produced by jets from YSOs where the jets strike the ambient medium.

The contraction time to the point where nuclear reactions are set off is about 4×10^7 yr for one solar mass.

The initial conditions for star formation can be defined by the requirement that the thermal energy in the core cannot compensate the gravitational one. Therefore, it will be unstable and the gravitational collapse will happen. This requirement defines a mass that is gravitationally bound, the Jeans mass, which is the minimum mass that the cloud of given density ρ and temperature T must have to be unstable:

$$M_J = 27.8 \sqrt{\frac{T^3}{\rho}}. \quad (1.1)$$

Lada (1987) classified the embedded population of the sources of Wilking & Lada (1983) and Lada & Wilking (1984), where photometry from 1 to 20 μm was obtained. The energy distributions for the observed sources were constructed and three distinct classes of objects were identified. The established classification scheme goes through the definition of the spectral index:

$$a = \frac{d(\log \lambda F_{\lambda})}{d \log(\lambda)}. \quad (1.2)$$

For class I sources $0 < a < 3$, for class II sources $-2 < a \leq 0$ and for class III sources $-3 < a < -2$ (see Fig.1.5).

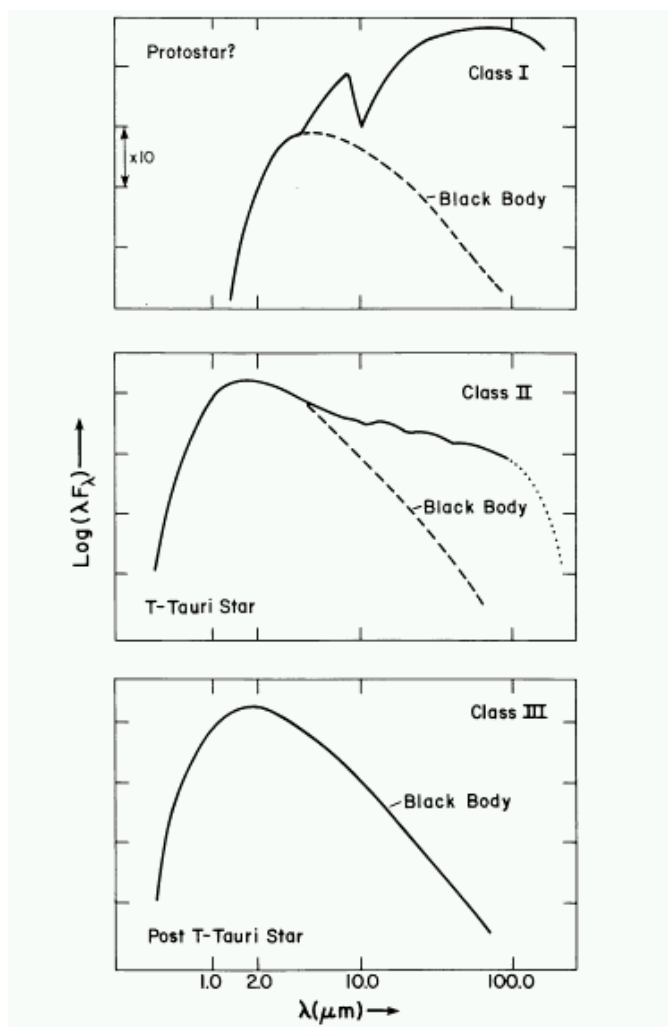


Figure 1.5: Proposed classification scheme by Lada (1987) for the spectral energy distributions (SEDs) of embedded YSOs.

T Tauri stars, class II YSOs by Lada's (1987) classification, are identified by their strong emission lines that include the Balmer lines and CaII H and K, a blue and UV continuum, eruptive variability, strong mass loss and an infrared excess due to thermal emission from dust. They are post-infall and PMS objects and are implicated in the production of Herbig-Haro objects (Hunter 1992).

Class III YSOs have little dust and are blackbody emitters. These are PMS or main-sequence stars (Hunter 1992).

Lada's argumentation is that the 3 classes probably represent an evolutionary sequence in which the enveloping dust and gas is dissipated around the young star from Class I to III.

Chini & Wargau (1998) pointed out by investigating the stellar content of M17 that a visual extinction of $A_v \geq 30$ mag converts any emission of arbitrary temperature into a Class I object, no matter whether the origin is pure stellar radiation or optically thin dust, if the

spectral index is calculated between 2.2 and 5 μm . As the classification of Lada is strongly affected by interstellar extinction Chini & Wargau (1998) introduced the empirical colour criteria $(K - L) > 0.26 (J - K) + 0.25$ and/or $(K - M) > 0.37 (J - K) + 0.80$ that may reliably trace Class I objects in the absence of data longward of 4.8 μm . Due to the fact that these relations are independent of the amount of extinction, they measure directly the emission of circumstellar dust.

Nevertheless, more recent work suggests that the Class I of Lada (1987) may be more evolved than true protostars. Chini et al. (1993) mapping the dark cloud L1652 at 1.3 mm were the first to detect a cold and gravitationally unstable cloud which is a protostar.

Andre, Ward-Thompson & Barsony (1993) define a new class of YSOs, which they called Class 0 to indicate their extreme youth. They propose to define as Class 0 the submillimeter sources which have

$$\frac{L_{\text{bol}}}{L_{1.3}} < 2 \times 10^4 \quad (1.3)$$

that roughly corresponds to $L_{\text{submm}}/L_{\text{bol}} > 5 \times 10^{-3}$. L_{submm} is defined as the luminosity radiated longward of 350 μm and L_{bol} is a source's bolometric luminosity.

Kinematical evidence for infall motions were observed in several Class 0 sources (Lada 1999).

Research in high-mass star formation is not in such an advanced stage of understanding as the low-mass one due to the following: i) high-mass protostars are relatively rare and tend to be more distant than their low-mass counterparts (low-mass star forming regions like Taurus and ρ -Ophiucus are located within 150 pc while the nearest high-mass star forming site - Orion - is about 460 pc away); ii) high-mass stars tend to form in the most opaque environments (so only infrared, submillimeter and radio observations allow the inspection of massive star formation sites) and in highly clustered environments; iii) sites of massive stars are rapidly altered and records of their birth are erased (Bally 2002).

Many massive stars are members of multiple systems. Massive binaries could be the reason for the existence of runaway OB stars, expelled from young clusters. Zinnecker (2003) speculates that at lower metallicity (e.g. LMC and SMC) the fragmentation leads to more and/or wider binaries.

Massive star formation has several observational characteristics: i) massive outflows seen by radio measurements (Maeder & Behrend 2002); ii) disks surrounding massive stars (e.g. IRAS 20126 + 4004 observed from NH_3 line by the VLA) should be short-lived compared to their low mass counterparts as the UV environment in an OB cluster lead to photoevaporation of disks on a time scale of a few 10^5 yr (Yorke & Sonnhalter 2002); iii) high velocity dispersion (e.g. CS line in Orion KL Nebula) (Maeder & Behrend 2002).

There are four main ideas about high-mass star formation:

- Massive stars can form via accretion through a disk in a similar way to the lower mass case. A powerful radiation-driven outflow in the polar directions and a thick disk result from the high luminosity of the central source (Yorke & Sonnhalter 2002).
- Maeder & Behrend (2002) pointed out that the turbulent pressure associated to large

turbulent velocities in clouds imply high accretion rates for massive stars. They proposed that the accretion rate \dot{M}_{accr} grows with the already accreted mass ($\dot{M}_{\text{accr}} \propto M^{1.5}$).

- The collisional build-up of massive stars involve intermediate-mass stars that form through accretion on to initially lower mass protostars. The collisions are probably stopped by the ejection of gas in the core once a star with $M \approx 50 M_{\odot}$ is formed. This scenario was created to avoid the radiation pressure problem (due to the large luminosity of stars with $M > 10 M_{\odot}$ the radiation pressure on dust can halt the collapse and reverse the infall) (Bonnell, Bate & Zinnecker 1998).
- Gas accretion in young stellar clusters was studied by Bonnell et al. (2001). They modelled clusters where gas dominates the gravitational potential in contrast to clusters where stars dominate.

1.3 The Interstellar Medium

The space between the stars is occupied by the interstellar medium (ISM). The ISM is bathed in the universal microwave background, cosmic rays and the magnetic field of its host galaxy. The components are gas and dust grains, which are in various thermal and chemical phases.

About 1% of the total mass of the ISM is constituted by dust grains and contain most of the heavy elements (Knapp 2001). However, there is still little consensus on exactly how much dust resides in galaxies and how it is distributed in relation to the stars. The spatial distribution of dust with regard to other components of the ISM and the stars is highly important in the understanding of several astrophysical phenomena. Dust grains are condensed from gas mainly in the latest stages of stellar evolution and then injected with gas into the ISM. Interstellar dust plays an important role in cooling and heating interstellar gas and catalyzing on their surface certain molecules (e.g. H_2) in cold dense clouds (Watson & Salpeter 1972, Takahashi, Masuda & Nagaoka 1999). While traveling through the ISM, physical and chemical processes alter the properties of interstellar dust (Sandford 1996). Dust grains may be disrupted by mutual collisions and sputtering in shocks, but they grow by accretion of gas and coagulation processes in molecular clouds where star formation takes place (Draine 1985).

The gas is mainly hydrogen, about 10% of the atoms are helium, and a further 0.1% of atoms are carbon, nitrogen and oxygen each. Other elements are even less abundant (Dyson & Williams 1997). Atomic, molecular and ionized gas have been observed.

The gas phases are: molecular medium (MM), cool neutral medium (CNM), warm neutral medium (WNM), diffuse ionized gas (DIG), which is also called warm ionized medium (WIM) (Berkhuijsen, Beck & Walterbos 2000), and hot ionized medium (HIM). The balance between these states is governed by localized heating and cooling processes, along with galaxy-wide pressure variations. These components of the ISM differ in density, temperature, degree of ionization, mass and filling factor. In Table 1.1 the mean electron densities $\langle n_e \rangle$ and temperatures $\langle T \rangle$ for the different ISM gaseous phases are given.

The MM (see next subsection) is best probed by CO emission. The cool neutral phase of the

Table 1.1: Properties of the ISM gaseous phases (Rossa 2001).

| Phase | $\langle n_e[\text{cm}^{-3}] \rangle$ | $\langle T[\text{K}] \rangle$ |
|-------|---------------------------------------|-------------------------------|
| MM | 5.4×10^{-1} | 2×10 |
| CNM | 4×10^{-1} | 1.4×10^2 |
| WNM | 1.6×10^{-1} | 6×10^3 |
| WIM | 8×10^{-2} | 8×10^3 |
| HIM | 3×10^{-3} | 5×10^5 |

ISM can be studied through absorption of HI. The HI is best traced at 21-cm emission in the WNM. The WIM is investigated mainly by $H\alpha$ emission. The hot ionized phase can be observed by X-ray emission and UV absorption of the OVI lines.

1.3.1 Molecular gas

When the diffuse neutral interstellar gas reaches a density of about 100 particles/cm³ molecules can be formed, specially H₂. In the ISM molecular clouds represent the densest and most active phase. The region of high density needs to have enough size to avoid the penetration of the interstellar UV radiation field, so that a dissociation of the molecules does not happen. Other molecules, like CO, can also be formed if H₂ is constituted. Molecular clouds are detected through their radio signature: mostly the spectral lines of CO, but also from molecules like NH₃ and HCN.

Eddington (1937) and Stroemgren (1939) suggested the existence of molecular hydrogen (H₂) in interstellar space. Gould & Salpeter (1963) and Hollenbach, Werner & Salpeter (1971) predicted it could be a large fraction of all hydrogen.

Molecular hydrogen is by far the most abundant molecule in the ISM, followed by carbon monoxide (CO). Being such an important constituent of the ISM in galaxies, the study of H₂ has received great interest. However as a symmetrical molecule there is not a permanent electric dipole moment and so H₂ is very difficult to be detected directly. The H₂ molecule lowest rotational transition within the vibrational $v = 0$ state is the $J = 2 \rightarrow 0$ one, with the $J = 2$ state being 500 K above the ground level, which means that it is hardly populated in molecular clouds unless they are strongly heated (Klein priv. comm.). Therefore, H₂ is seen in emission only from warm or hot gas (e.g. from shock-heated regions). Warm H₂ gas has been observed in emission at IR wavelengths, but the major amount of H₂ is located in cold gas, which is measurable only in far-ultraviolet absorption along individual lines of sight towards bright sources.

CO is a good tracer of molecular gas in galaxies. Its rotational transitions are collisionally excited by H₂ and the transitions which happen between the lowest CO rotational energy levels lie in the submillimeter wavelength range. The most abundant variety of CO isotope, ¹²C¹⁶O, has its transitions located at 115 GHz ($J = 1 \rightarrow 0$), 230 GHz ($J = 2 \rightarrow 1$), etc. The 115 GHz ($\lambda = 2.6$ mm) and 230 GHz ($\lambda = 1.3$ mm) emission lines lie in atmospheric transmission windows (see Fig. 2.3) which makes them easily observable.

ORFEUS (Orbiting and Retrievable Far and Extreme Ultraviolet Spectrometer) far UV

echelle spectra have been used to detect the first H_2 extragalactic absorption lines: in the LMC (de Boer et al. 1998, Richter et al. 1999) and the SMC (Richter et al. 1998). Owing to their proximity, the MCs are the only low-mass galaxies for which comprehensive studies of molecules other than H_2 and CO as well as rare isotopes from the latter have been undertaken (e.g. Heikkilä, Johansson & Olofsson 1999).

Being commonly assumed that star formation requires interstellar clouds to pass through high-density, cool phase, in which most of the hydrogen is in molecular form, studies of star formation seek to determine H_2 amounts. The most common method to measure its amount in the ISM is to estimate it from the abundance of CO. While the rare isotopes $^{13}\text{C}^{16}\text{O}$ and $^{12}\text{C}^{18}\text{O}$ are, respectively, owner of an optical depth typically < 0.3 and optically thin, the main isotope $^{12}\text{C}^{16}\text{O}$ is usually optically thick and so does not provide direct information on column densities. However, empirical relations between CO luminosities and masses of molecular clouds allow its use in an indirect way. This can be written as

$$M(\text{H}_2) = \beta L_{\text{CO}}, \quad (1.4)$$

where the conversion factor β is given in units of $[\text{M}_\odot / (\text{K km s}^{-1} \text{ pc}^2)]$.

Values for the conversion factor β from 3 to 11 $\text{M}_\odot \text{ K}^{-1} \text{ km}^{-1} \text{ s pc}^{-2}$ have been obtained in the Milky Way.

One can define the CO luminosity of a cloud as

$$L_{\text{CO}} = D^2 \int I_{\text{CO}} d\Omega, \quad (1.5)$$

where D is the distance and $\int d\Omega$ the solid angle of the source with the CO luminosity in units of $[\text{K km s}^{-1} \text{ pc}^2]$. The velocity integrated CO intensity is given by

$$I_{\text{CO}} = \int T_{\text{mb}} dv, \quad (1.6)$$

where T_{mb} is the main beam brightness temperature and the integrated CO signal is in units of $[\text{K km s}^{-1}]$.

Consequently the relation between the integrated CO line intensity I_{CO} and the molecular hydrogen column density $n(\text{H}_2)$ is given by

$$n(\text{H}_2) = X I_{\text{CO}}, \quad (1.7)$$

where the conversion factor X is in units of $[\text{cm}^{-2} (\text{K km s}^{-1})^{-1}]$.

Several methods have been worked out to relate the H_2 column density $n(\text{H}_2)$ to the observed CO line intensity I_{CO} for the Milky Way and other galaxies. The used techniques are: i) virial theorem; ii) gamma-ray emissivity; iii) H_2 absorption lines; iv) optically thin molecular lines; v) extinction observations; vi) FIR and HI studies.

A widely used assumption is that the clouds are in virial equilibrium. In this case the observed linewidth of a cloud with mass M_{vir} and radius R is $\Delta v \propto \sqrt{\frac{M_{\text{vir}}}{R}}$. If the contribution of atomic hydrogen and helium is known, the H_2 mass can be deduced from the cloud mass.

High-energy gamma-ray observations in the Galaxy for CO- H_2 calibration were used by Bloemen et al. (1986). The γ -ray intensity is a measure of the product of cosmic-ray density and

total gas density, integrated along the line of sight, practically irrespective to the composition or the physical state of the gas. The relationship is of the form

$$I_\gamma = \varepsilon_\gamma (n(\text{HI}) + 2X I_{\text{CO}}), \quad (1.8)$$

where ε_γ is the γ -ray emissivity per H atom in units of [photon (H atom)⁻¹ s⁻¹ sr⁻¹]. Both ε_γ and X can be estimated from a comparison of the CO, HI and γ -ray maps.

Richter et al. (1999) analyzed H₂ and CO absorption lines towards LH 10 of the N 11 complex in the LMC.

Dickman (1975) was the first who used a comparison of intensities of CO optically thin isotopes and visual extinction.

H₂ column densities towards CO clouds in the LMC, the SMC and other magellanic irregular galaxies were estimated by Israel (1997) from far-infrared surface brightness and HI column density data. The derived H₂ column densities compared to CO data imply that the CO-H₂ conversion factor X depends on the ambient radiation field intensity per nucleon and on the metallicity. The CO to H₂ conversion factor X shows a very close to linear dependence on the former and is inversely dependent on a steep function of metallicity.

From complete maps with low-resolution in the $J = 1 \rightarrow 0$ rotational transition of ¹²CO Cohen et al. (1988) and Rubio et al. (1991) concluded, respectively, for the LMC and the SMC a conversion factor $X_{\text{LMC}} = 6 X_{\text{G}}$ and $X_{\text{SMC}} = 20 X_{\text{G}}$. Rubio, Lequeux & Boulanger (1993) (Part III of the ESO-SEST Key Programme) estimated that the before derived X_{SMC} is a strong upper limit.

The application of a standard CO to H₂ conversion factor assumes similarity of extragalactic and Galactic molecular clouds. This assumption is not very reliable in environments different from those in the Milky Way. Therefore, the first method (virial theorem) is preferable and is adopted in this study.

1.3.2 Dust

Interstellar dust plays an important role in the evolution of the ISM as well as in the processes of star formation and stellar evolution. The dust manifests itself through absorption and scattering of light from stars and external galaxies behind it. There are several possibilities how dust is formed, with the options including supernova explosions of massive stars (Meikle et al. 1993), protostellar nebulae (Herbig 1970) and post-asymptotic giant branch (post-AGB) stars (Whittet 1991).

The sensitive submillimeter maps available from a few nearby galaxies (e.g. Guelin et al. 1993, Sievers et al. 1994) trace the emission from cold dust. Guelin et al. (1993) found in the edge-on Sb galaxy NGC 891, similar to our Galaxy, that the 1.3 mm and the CO brightness profiles are strikingly close. Sievers et al. (1994) found in the nearby spiral galaxy NGC 3627 that the cold dust emission shows a non-uniform distribution and is traced along the two prominent spiral arms. Zhang, Wright & Alexanders (1993) CO map for the same galaxy (a member of the interacting group the Leo Triplet) is almost identical to the Sievers et al. (1994) dust emission map. Therefore, it is clear that cool dust is associated with the molecular gas phase. So an obvious location for cool dust is inside the molecular clouds. The

outer layers of the clouds shield them from the ISRF. The warm dust phase ($25 \text{ K} < T_d < 50 \text{ K}$) resides in the outer layers of the molecular clouds or very near to the newly formed hot stars while the cool phase ($10 \text{ K} < T_d < 25 \text{ K}$) fills most of the volume inside these clouds. Cool dust would turn into hot dust ($T_d > 50 \text{ K}$) upon cloud collapse as it would then be extremely close to newly formed stars. Decomposing the emission spectra Sievers et al. (1994) and Guélin et al. (1993) concluded that 80% - 95% of the dust is in the cool phase (Sauvage 1997).

With the aim to reproduce the observations of interstellar extinction and polarization many different grain models have been proposed. Studies by Mathis, Rumpl & Nordsieck (1977) proposed a graphite-silicate model. This model used bare silicates while later works considered them e.g. coated by hydrogenated amorphous carbon (Duley, Jones & Williams 1989) or composite (Mathis & Whiffen 1989). A coal model of interstellar dust is developed by Papoular et al. (1995), while Sakata et al. (1987) showed one with quenched carbonaceous composite. Further studies like that of Draine (1981) and Draine & Lee (1984) concentrated on the materials used as ingredients of the Mathis, Rumpl & Nordsieck (1977) model. Draine & Lee (1984) predicted temperatures of $\sim 19 \text{ K}$ and $\sim 15 \text{ K}$ for sizes $a = 0.1 \mu\text{m}$ graphite and silicate grains exposed to the interstellar radiation field (ISRF) adopted by Mathis, Mezger & Panagia (1983).

The high flux ratios S_{12}/S_{100} and S_{25}/S_{100} in interstellar clouds as observed by IRAS (Boulanger & Perault 1988), the near and mid-IR resonances seen in emission in different sources and the very high color temperatures ($>1000 \text{ K}$) in reflection nebulae independent of distance to the exciting star (Sellgren et al. 1985) led to a change in the dust concept in use until the early eighties (e.g. Draine 1981) introducing the idea that an additional component of very small dust particles is present in the ISM. Their little size and therefore low heat capacity produces temperature fluctuations resulting in color temperatures much higher than the time averaged temperature of the grain material. Siebenmorgen & Krügel (1992) applied their dust model for the solar neighborhood and other three types of astronomical environments (reflection nebulae, planetary nebula and HII region). This dust model consists of three components: i) classical large grains with sizes $a > 100 \text{ \AA}$ of silicate and amorphous carbon, which are in thermal equilibrium with the ISRF, responsible for the FIR emission and the linear rise in the extinction curve; ii) small particles of graphite ($4 \text{ \AA} < a < 100 \text{ \AA}$) to explain the 2175 \AA extinction bump and the MIR emission; iii) polycyclic aromatic hydrocarbons (PAHs) that produce the near and mid-IR bands, part of the underlying continuum and are good candidates to explain the non-linear extinction rise in the FUV. They obtained that small particles of graphitic carbon have a spectrum peaking at 30 to 50 μm and often dominate over the large particles at $\lambda \leq 30 \mu\text{m}$. Where the large grains are cool ($\simeq 20 \text{ K}$) they account even for the 60 μm emission, while the PAHs dominate the spectrum in the wavelength range $5 < \lambda < 14 \mu\text{m}$.

The Milky Way, the LMC and the SMC are the only galaxies with observed interstellar extinction curves. The most notable differences are the strength in the feature around 2175 \AA and the level of the FUV extinction. The FUV rise in the Galaxy:LMC:SMC system increases from the Galaxy to the SMC while by the 2175 \AA bump it is the opposite (Sauvage 1997). Variations in the extinction curves are caused by variations in the size distribution and/or chemical composition of the dust grains. Fig. 1.6 shows the Galactic mean extinction curve (Savage & Mathis 1979) from the NIR to the FUV and results for the LMC (Koorneef

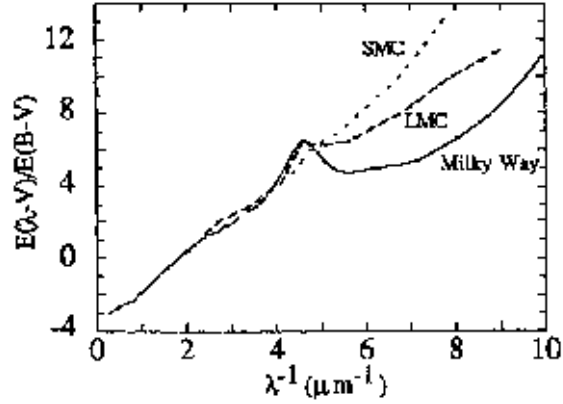


Figure 1.6: Extinction curves for the Galaxy, the LMC and the SMC (Sauvage & Vigroux 1991).

& Code 1981) and for the SMC (Bouchet et al. 1985). The fact that the small grains are less present in the MCs than in our Galaxy is not only indicated by the sequential decrease from the Milky Way to the SMC in the strength of the 2175 Å feature. It is also indicated by the 12 μm radiation in the MCs furnished by IRAS observations, which is very low due to the high UV interstellar radiation field. The differences between the 60 μm/100 μm versus 12 μm/25 μm color-color diagrams of the MCs and the Milky Way also indicate differences in the properties of the dust grains (Westerlund 1997).

The following calculations precede the derivation of the emitting dust mass.

From the radiative transfer equation of the thermal emission of dust the net flux emitted by the dust is obtained. The equation of radiative transfer is given by

$$\frac{dI_\nu}{ds} = -\iota_\nu I_\nu + j_\nu, \quad (1.9)$$

where I_ν [erg s⁻¹ cm⁻² Hz⁻¹ sr⁻¹] is the intensity, ds the distance element, ι_ν [cm⁻¹] the absorption coefficient and j_ν [erg s⁻¹ cm⁻³ Hz⁻¹ sr⁻¹] the emissivity.

The optical depth is written as

$$\tau_\nu(s) = \int_{s_0}^s \iota_\nu(s') ds'. \quad (1.10)$$

Another important quantity is the source function defined as

$$\Sigma_\nu = \frac{j_\nu}{\iota_\nu}. \quad (1.11)$$

With Eq. (1.10) and (1.11) Eq. (1.9) can be integrated:

$$I_\nu(\tau_\nu) = \Sigma_\nu(1 - \exp(-\tau_\nu)), \quad (1.12)$$

where $I_\nu(\tau_\nu = 0)$ is nulled.

Dust particles in interstellar clouds in equilibrium of heating and cooling reemit a continuous spectrum resembling a thermal spectrum characterized by a temperature T_d . In this case $\Sigma_\nu = B_\nu(T_d)$, where $B_\nu(T_d)$ denotes the Planck function at temperature T_d . For optically thin ($\tau_\nu \ll 1$) emission, $1 - \exp(-\tau_\nu) \rightarrow \tau_\nu$.

Therefore, the approximation

$$I_\nu(\tau_\nu) = B_\nu(T_d)\tau_\nu \quad (1.13)$$

is valid.

The net flux emitted by the dust can be written as

$$S_\nu = B_\nu(T_d) \int \tau_\nu(s) d\Omega, \quad (1.14)$$

where $\int d\Omega$ is the solid angle of the source.

The optical depth τ_ν is expressed as

$$\tau_\nu(s) = \int_0^D \kappa_{d,\nu}(s) ds = \kappa_{d,\nu} \int_0^D \rho_d(s) ds, \quad (1.15)$$

where D is the distance of the source, $\kappa_{d,\nu}$ [$\text{cm}^2 \text{g}^{-1}$] the absorption coefficient per gram of dust (opacity) and ρ_d [g cm^{-3}] the mass density of dust.

One also finds

$$\int_0^D \rho_d(s) ds = \frac{M_d}{D^2 \Omega}, \quad (1.16)$$

where M_d is the total dust mass.

So equation (1.14) becomes

$$S_\nu = \kappa_{d,\nu} B_\nu(T_d) M_d D^{-2}. \quad (1.17)$$

To determine the value of the dust mass M_d the dust temperature T_d has to be well established. The latter is determined as a color temperature from multi-wavelength observations. Longer wavelengths are more sensitive to colder dust. The coldest component of the dust is decisive for the total content of the interstellar matter. So measurements of the far-infrared (FIR) and submillimeter wavelength emission are a convenient method to determine the dust mass. The FIR/submillimeter part of the spectrum is fitted by modified Planck curves of the form $\nu^m B_\nu(T_d)$.

Therefore, from the last equation follows

$$\frac{S_{\nu_1}}{S_{\nu_2}} = \frac{\kappa_{d,\nu_1} B_{\nu_1}(T_d)}{\kappa_{d,\nu_2} B_{\nu_2}(T_d)} = \frac{\nu_1^m B_{\nu_1}(T_d)}{\nu_2^m B_{\nu_2}(T_d)}, \quad (1.18)$$

where ν_1, ν_2 are two observation frequencies.

Assuming a mixture of silicate and amorphous carbon grains with a mass ratio $m_{\text{Si}}/m_{\text{C}} = 1.5$ with optical constants of $m = 3.4 - 0.04i$ for silicate and $m = 12 - 4i$ for amorphous carbon, one finds absorption efficiencies $Q_{1200}(\text{Si}) = 0.86a$ and $Q_{1200}(\text{C}) = 2.13a$. Therefore comes the absorption coefficient $\kappa_{1200} = 0.37 \text{ cm}^2$ per gram of dust, with a [cm] being the grain radius. The before mentioned value of κ_{1200} is adopted in this study. At this wavelength the absorption coefficient is independent of the grain radius. The factor κ_{1200} is probably equal in all galaxy types because of the similar formation of dust in old stars and supernovae, but different radiation fields could play a role in the processing of the grains making it distinct.

The submillimeter spectrum of a cool cloud can be fitted by a value of $m \sim 1$ at $\lambda < 200 \mu\text{m}$ to $m \geq 2$ by $\lambda \sim 1000 \mu\text{m}$ (Hildebrand 1983). In this study $m = 2$ (Reach et al. 1995, Schlegel, Finkbeiner & Davis 1998, Stanimirovic 1999) is adopted.

1.3.3 Gas-to-dust ratio

The gas-to-dust ratios in the MCs are very useful to determine the importance of dust on cosmological scales e.g. for distance determination. As the MCs have lower abundances of heavy elements and dust than our Galaxy, they may resemble galaxies at high redshifts, which are presumably in early stages of the chemical enrichment.

In the last subsection how to obtain the dust masses was explained.

The total gas mass can be defined as

$$M_{\text{g}} = \frac{S_{\nu} D^2}{\kappa_{\text{ism},\nu} B_{\nu}(T_{\text{d}})}, \quad (1.19)$$

where $\kappa_{\text{ism},\nu}$ [$\text{cm}^2 \text{ g}^{-1}$] is the absorption coefficient per gram of interstellar matter.

Dividing the total gas mass M_{g} by the dust mass M_{d} from Eq. (1.17) and, if the contribution of atomic hydrogen and helium is known, the H_2 mass $M(\text{H}_2)$ can be deduced such that

$$M(\text{H}_2) = R M_{\text{d}}. \quad (1.20)$$

Assuming the Galactic values for carbon and silicate as $[\text{C}]/[\text{H}] = 3 \times 10^{-4}$ and $[\text{Si}]/[\text{H}] = 3 \times 10^{-5}$ the molecular gas to dust ratio R is about 150 for the Milky Way.

From Eq. (1.4) and (1.20) one can derive

$$\frac{L_{\text{CO}}}{M_{\text{d}}} = \frac{R}{\beta} \quad (1.21)$$

with $L_{\text{CO}}/M_{\text{d}}$ in units of [$\text{K km s}^{-1} \text{ pc}^2 \text{ M}_{\odot}^{-1}$].

Using the thermal dust emission at 1.2 mm the former equation yields

$$\frac{L_{\text{CO}}}{L_{\text{dust}}} = \frac{R}{\beta \kappa_{\text{d},1200} B_{1200}(T_{\text{d}})} \quad (1.22)$$

with L_{dust} in units of [Jy Mpc^2].

1.4 Outline of this Current Ph.D. Thesis

This work presents the observations and results from 1.2 mm continuum measurements in the Large Magellanic Cloud (LMC) and the Small Magellanic Cloud (SMC).

The sample of the regions in the LMC and the SMC in which the dust investigation was conducted is described in Chapter 2. How the data was reduced (the step by step data reduction procedures are shown in Appendix A) and also the telescope and the bolometer used for the observations are presented.

Chapter 3 presents the individual LMC regions that were studied, as well as the results of the dust continuum emission. The derived dust temperatures and dust masses are also shown.

For the SMC the same work performed for the LMC in Chapter 3 is presented in Chapter 4.

In Chapter 5 the derived dust masses in the LMC and the SMC are compared with CO measurements, which have been taken from several authors. The aim of this comparison is to determine the gas-to-dust ratio.

The observed dust continuum emission together with IRAS data is used to determine the FIR luminosity in Chapter 6. Along with the CO data, this enables to trace the star formation efficiency of the investigated regions in both galaxies.

Chapter 7 gives a brief summary of the results presented in this work.

Chapter 2

Data and Reduction

2.1 Sample Selection

In principle it would be desirable to have a whole survey of the MCs in the 1.2 mm continuum emission to an extent similar to what has already been done by IRAS in the infrared and in CO with the NANTEN telescope, installed at the Las Campanas Observatory in Chile (Fukui et al. 1999). Such procedure would furnish a perfectly suited distribution of the cold dust component in these galaxies. However, this is impractical for only one Ph.D. thesis, then all the necessary observations cannot be gathered and reduced in a reasonable amount of time. In spite of this limitation, the study here presented is the first attempt to observe in large scale the MCs continuum emission at 1.2 mm.

The sample selection procedure followed two criteria: first, focus the 1.2 mm observations on regions with relatively intense CO emission and, later, make a more extended survey of the MCs.

The CO emission observations (e.g. Cohen et al. 1988) undertaken in the LMC revealed a concentration in molecular clouds associated with 30 Doradus. In the other regions of the LMC the emission is confined to small clouds with a small surface filling factor. Johansson et al. (1998) mapped fields centered on the 30 Dor nebula as well as on the southern part of the 30 Dor complex, containing the HII regions N 158C, N 159 and N 160. By comparing typical Galactic clouds to Magellanic objects which are biased in favor of the stronger CO sources, Israel et al. (1993) concluded that, in the LMC, velocity-integrated ^{12}CO and ^{13}CO emission are lower than in the Milky Way by at least a factor of three and, in the SMC, they are lower by at least a factor of ten. They also observed less as prominent as the 30 Dor complex, but still quite massive CO complexes associated with HII regions such as N 44. The N 44 CO clouds are among the brightest ones in the LMC as well as the ones associated with the HII regions N 113 and N 214.

Two large CO complexes are located in the SMC - one in the northeast and the other in the southwestern region of the bar. In the former region the CO emission is weaker than in the latter one. Rubio et al. (1991) made maps showing that the southwestern complex can be separated into at least two components. Rubio et al. (1993) performed observations of two extended regions in the SW bar of the SMC, which are parts of the two components

previously identified. These authors also studied some isolated molecular clouds in the SW region such as LIRS 36 (N 12) and LIRS 49 (N 27). Both are associated with relatively compact HII regions, somewhat stronger than Orion A.

The 1.2 mm continuum observations of the LMC undertaken in this work concentrate on coordinates taken from the regions mentioned before. The observations of the SMC were done towards bright HII regions in the SW Bar (N 12, N 27), in the main body (N 66) and in the Shapley Wing (N 81, N 83-84, N 88) (Table 2.1).

Table 2.1: List of selected regions.

| Object* | reference of CO | Galaxy |
|-------------------|-------------------------|--------|
| 30 Dor A (N 157A) | Johansson et al. (1998) | LMC |
| 30 Dor B (N 157B) | Johansson et al. (1998) | LMC |
| 30 Dor C | Johansson et al. (1998) | LMC |
| N 158C | Johansson et al. (1998) | LMC |
| N 159 | Johansson et al. (1998) | LMC |
| N 160 | Johansson et al. (1998) | LMC |
| N 44 | Israel et al. (1993) | LMC |
| N 113 | Israel et al. (1993) | LMC |
| N 214 | Israel et al. (1993) | LMC |
| N 12 | Israel et al. (1993) | SMC |
| H 15 | Israel et al. (1993) | SMC |
| N 27 | Israel et al. (1993) | SMC |
| N 66 | Israel et al. (1993) | SMC |
| N 76 | Israel et al. (1993) | SMC |
| N 81 | Israel et al. (1993) | SMC |
| N 83-84 | Israel et al. (1993) | SMC |
| N 88 | Israel et al. (1993) | SMC |

* Positions and sizes of the sources: see tables in Chapters 3 and 4, respectively, for the LMC and the SMC.

2.2 Telescope

The observations were performed at the Swedish-ESO Submillimetre Telescope (SEST), the only large submillimeter telescope in the Southern Hemisphere. It is a 15 m diameter telescope situated in the Chilean Andes at the ESO site of La Silla ($70^{\circ}44'04''$ W, $-29^{\circ}15'34''$) at an altitude of 2400 m, which can operate at wavelengths down to 0.8 mm. The SEST (Fig. 2.1) is a Cassegrain antenna designed by engineers of the Institut de Radio Astronomie Millimetrique (IRAM) with an alt-azimuth mount. It is similar to the telescopes of the millimeter interferometer on Plateau de Bure, but on a fixed base. The main reflector is an axisymmetric paraboloid and the subreflector is a hyperboloid that has a diameter of 1.5 m. The telescope reflector surface is within $65 \mu\text{m}$ rms of the ideal paraboloid and the pointing accuracy in azimuth and elevation is approximately $3''$ rms.

The main technical features and observing system of the SEST can be found in Booth et al. (1989) as well at www.la.eso.org/lasilla/Telescopes/SEST/.



Figure 2.1: The 15 m Swedish-ESO Submillimetre Telescope (SEST) at the ESO site of La Silla, Chile (SEST homepage).

2.3 Bolometer Array

SIMBA, acronym for SEST IMaging Bolometer Array (Fig. 2.2), is a 37-channel bolometer array with a central frequency of the spectral bandpass of 250 GHz, corresponding to a wavelength of 1.2 mm and operates at 300 mK. This working temperature is achieved by an evacuated multi-layer cryostat. The cooling is provided by a closed cycle liquid ^3He reservoir, surrounded by ^4He and N_2 insulation layers, both liquid. The receiver comprises 37 horn antennae which are arranged in a hexagonal structure with a pixel-to-pixel separation of $44''$. The hexagonal structure is used in order to achieve the best possible spatial coverage, which is about $4'$ on the sky.

SIMBA, which is the first bolometer array in the Southern Hemisphere, had its first observing use on the 15 m SEST in June 2001. It was built by the Max-Planck-Institut für Radioastronomie (MPIfR) in Bonn, Germany, in collaboration with the Astronomisches Institut der Ruhr-Universität Bochum (AIRUB), Germany. The half power beamwidth (HPBW) of each SIMBA array channel is about $23''$ which provides a linear resolution of about 6 pc at the

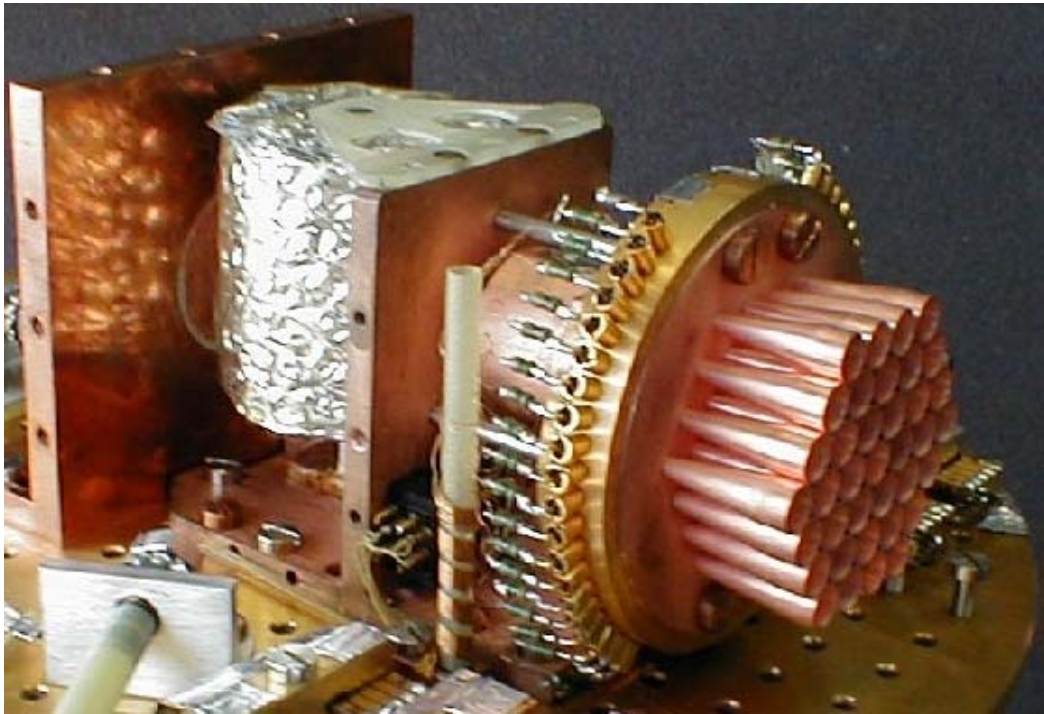


Figure 2.2: Close-up of the 37 horns (SIMBA Observers Handbook, 2002).

distance of the LMC and about 7 pc at the distance of the SMC.

Bolometers, cooled to at least 300 mK, are presently the most sensitive continuum receivers in the wavelength range between 0.3 and 3.0 mm (Kreysa, Beeman & Haller priv. comm.). The success of arrays in comparison with a single channel instrument comes from the fact that in the presence of sky-noise, the noise is partially correlated across the array, thus making possible the development of sky-noise reduction algorithms. Also a fixed spatial relationship exists between the beams making the registration of individual beam maps more precise than if they had been recorded sequentially with a single beam instrument. The introduction of submillimeter imaging arrays such as SIMBA turned possible the mapping of cold interstellar grains with high sensitivity and good spatial resolution.

The history of the development, the general aspects and a description of the bolometer arrays used on large telescopes for carrying out sensitive continuum measurements are presented in Thum et al. (1992) and Kreysa et al. (1998).

2.4 Submillimeter Observations

The submillimeter wavelength range is adopted to be between 0.2 and about 3 mm (Chini 1989) (in Fig. 2.3 the few spectral windows where the observations are possible are shown). Astronomical observations from ground based telescopes at submillimeter wavelengths are strongly affected by fluctuations of the atmospheric emission. A common method used to solve this problem is the dual beam technique. In this case a wobbling secondary mirror

is used which alternatively points the beam to two adjacent positions on the sky. This technique has some disadvantages: i) a fast, precisely moving mirror is a technical challenge, particularly for large telescopes; ii) the mechanics of wobbling mirror usually allows only a certain direction of movement; iii) it is a source of vibrations that can interfere in the signals of highly sensitive bolometers; iv) small asymmetries can lead to large offsets, due to different optical paths for each beam (Reichert et al. 2001).

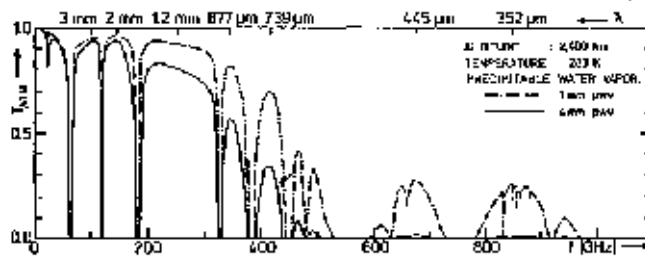


Figure 2.3: Atmospheric transmission as a function of wavelength and water vapor for an altitude of 2400 m.

Fast scanning is a new observing technique for submillimeter astronomy from ground based telescopes (details in Reichertz et al. 2001). Instead of wobbling the secondary mirror with a fixed frequency of a few Hz to filter the atmospheric contribution, the detector outputs are sampled at much higher rate without a modulation by the secondary mirror. As in multichannel bolometers all beams receive atmospheric emission simultaneously, the skynoise suppression is done by the data reduction through the correlation analysis between the detector pixels. The idea of fast scanning is to convert the spatial frequencies of the sky into the detector frequency band. The frequency passband is given by:

$$G_\nu = \frac{1}{(1 + 1/(i2\pi\nu\tau_{\text{amp}}))(1 + i2\pi\nu\tau_{\text{bol}})}, \quad (2.1)$$

where $\tau_{\text{amp}} = RC$ is the time constant of the high pass filter at the amplifier of the bolometer given by the product of the resistor R and the capacitor C and $\tau_{\text{bol}} = C_{\text{H}}/G_{\text{T}}$ is the effective thermal time constant of the bolometer given by the ratio between its heat capacity C_{H} and the thermal conductance G_{T} of the thermal link.

This observing mode was developed because of various reasons, one of them being the fact that a wobbling secondary mirror is not available on every telescope where continuum observations are of interest. And this is the case of the SEST. Therefore, all observations for this work were made in fast scanning mode which even allows to create large maps. SIMBA permits a variety of map sizes and scan speeds. The scans were separated in elevation by $8''$ (approximately a third HPBW). A typical map of $900'' \times 392''$ in size having an average sensitivity of 30-40 mJy/beam and $80''/\text{s}$ as scan speed takes 15 minutes of integration time, including a 30% overhead. Integration times varied between this and 45 minutes per map. The spatial sampling can be optimized by co-adding single maps taken at different hour angles. This procedure is done as the hexagonal array design creates gaps in the spatial coverage of the observed area and the fast scanning mapping mode may cause strip-line

artefacts in the map, especially at mediocre and variable weather conditions (Fig. 2.4 shows the configuration of the 37 channels used for the fast scanning mode).

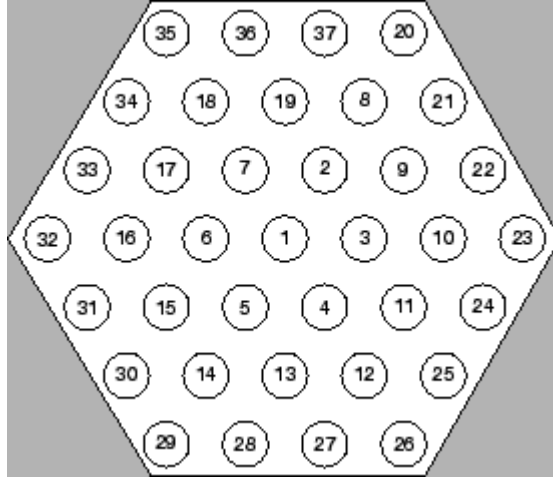


Figure 2.4: Arrangement of the SIMBA bolometer channels of the DC biased/ AC coupled configuration used for the fast scanning observing mode (the distance between the channels 23 and 32 is $4.5'$) (SIMBA Observers Handbook, 2002).

Pointing and focus were done using a planet or a strong continuum source (e.g. Eta Carinae) about every three hours. Pointing is necessary in order to determine the appropriate offset correction to the telescope coordinates and align the telescope with the celestial coordinate system. The pointing accuracy was in the order of $3'' - 5''$. Focusing is necessary to achieve the best spatial resolution and provide the highest signal-to-noise ratio possible. A focused telescope results in the narrowest spatial flux distribution of a point-source with the highest peak flux. The sky emission was measured regularly at different elevations every two hours in order to obtain the atmospheric opacity. The determined atmospheric transmission by sky dips was in general $\tau_{1.2\text{mm}} \approx 0.1 - 0.2$. As the thermal dust emission is usually hard to detect, the selected regions were mapped several times to obtain a considerable integration time and consequently increase the average sensitivity of the observations. The mapping of a selected region was performed in distinct time schedules, preferentially before and after the culmination. This was undertaken to avoid scanning effects in the final map.

The observations were carried out by Dr. Marcus Albrecht, Zita Banhidi and myself during July and October 2001 and June, September and November 2002.

During June, August and October 2002, Dr. Lars E. B. Johansson observed several areas of the SMC and generously allowed the use of the raw data in this study.

The number of maps is distinct between the several regions due to the not constant observing conditions during the several observing periods.

2.5 MOPSI

The data reduction of the 1.2 mm measurements taken at the SEST was performed by using the MOPSI (Mapping On - Off Pointing Skydip Imaging) software package. MOPSI is a data reduction and analysis software particularly developed for the IR and submillimeter wavelengths mapping data, which has been created and is being frequently improved by Dr. R. Zylka of the Institut de Radioastronomie Millimetrique (IRAM) from Grenoble, France.

The sequence of steps of the data reduction are explained below:

- MOPSI cannot read the raw fits files. Therefore, they are converted with the `simbaread` software, which has been programmed by Dr. Roland Lemke and Dr. Marcus Albrecht (AIRUB).
- Before getting into the data reduction the `tau.TAUS` file, which contains the derived opacity, should be prepared. The opacity file is created by `simbaread`. The performed skydips provide the zenith opacity allowing to correct the measured flux as the signal intensity is changed by the airmass it has passed through the atmosphere.
- The reduction procedure must be written in a file with the extension MOPSI, e.g. `reduce.MOPSI`. The main data reduction steps comprise despiking, deconvolution, gain elevation correction, the correction for atmospheric extinction, the subtraction of a proper baseline, skynoise reduction, conversion of the number of counts to mJy/beam and the reduction routine is constituted of the following commands (see Appendix A for more details)(SIMBA Observers Handbook, 2002):
 - *del dc*: the total power channels (38 to 40) are deleted because they are included in the raw data only for information about atmospheric conditions during the measurement.
 - *init gfit*, *init histo*, *init spike*: the buffer containing, respectively, earlier Gaussian fits, list of previous commands and information about the blanked region is emptied. Spikes can originate from cosmic rays or electronic discharges. Spikes must be eliminated as they can be responsible for noise or mimic real emission.
 - *base t 5*: baseline fit to the whole time series with a polynomial of the indicated order. Long term fluctuations in the sky background radiation and electronical instabilities are the most important causes for baseline drifts. Their influence is removed or minimized by the baseline subtraction.
 - *corr ge*: correction for the gain-elevation variation of the telescope. The gain elevation correction is applied to recover the optimal shape of the telescope dish as it undergoes distortion because of gravitational influence. This deformation is elevation dependent.
 - *set mask*: stores the blanked data in the spiker buffer.
 - *> 5 rms*: masks or blanks spikes. In this case they are defined as data exceeding values of 5 times the rms noise. Despiking can damage strong sources, but in this work the detected sources are all weak in individual maps.
 - *< -5 rms*: the same as above for negative spikes.

- *interpolate blanks*: interpolates the blanks produced during the despiking. These gaps are filled with values, which are interpolated from neighboring data points.
- *mask*: re-establishes the original blanked data from before the despiking. This is necessary, as the interpolation also affects blanked data that have not previously been spikes e.g. produced by tracking errors during the turning of the telescope at the end of a subscan.
- *base r az < 1e9 > -1e9*: defines the area of the base range in the channel maps. The whole area is chosen for a first look by defining an azimuth range in arcseconds large enough to cover a complete subscan.
- *pol 1111*
base r out sys equ: another option to define a base range usually applied to extended sources: a polygon matching the source is loaded first. This polygon is usually created from a reduced map after a preliminary reduction stage with a simple base range. The base range is set to the map area outside the polygon. Since it has been produced in equatorial coordinates, *sys equ* must be added. When reducing a mosaic of several maps, the polygon is understood relative to the final mosaic. In order to use the correct bit of the polygon to each of the individual maps, the keyword `pro <hh:mm:ss.s> <dd:mm:ss>` must be added representing the center of the mosaic.
- *base l 0*: baseline fit with a constant value. It is applied to each individual subscan in the map. Only order 0 fits are used before *deconv* as wrong results can appear by other orders.
- *set mask*
deconv
mask: the deconvolution of the bolometer signal restores the real source signal. It is executed to get back to the original Gaussian shape of the beam on a point source. This happens because the fast scanning makes it necessary to use AC coupling of the channels, which is actually a RC high pass filter at the input of the amplifier, in order to reduce the noise at low frequencies. Therefore, a band pass is created which changes the incoming signal. The bolometer signal must be deconvolved with a function matching the electronics. The mask command removes possible edge artifacts caused by the deconvolution.
- *tau tau 20000*: the correction for atmospheric extinction is done with the already created tau.TAUS file. In order to prevent an interpolation of the opacity over a too extended amount of time, the search can be restricted to a time difference around the observed map in seconds.
- *corr ext*: is the actual correction procedure, which interpolates the opacity from the selected skydips for every data point in the map by multiplying it by the correction factor $(\exp(-\frac{\tau}{\sin h}))$, where τ is the zenith opacity and $(\sin h)^{-1}$ is the airmass at the elevation h .
- *base l 4*: another baseline fit, now at higher order. The order chosen also sets the order of the baseline fit in the following skynoise reduction procedure.
- *store weight rms2 az < 1e9 > -1e9* or *store weight rms2 out sys equ*: the weight of each channel is stored according to its noise level. The region where the noise

is calculated should be kept identical to the base range.

- *snf ... run*: encloses the skynoise reduction. The atmospheric fluctuations contribute to the noise and some bolometer channels should experience the same modifications in the flux. By eliminating this correlated noise the signal-to-noise ratio of the submillimeter source is increased. The atmospheric contribution can be removed by using neighboring channels of the bolometer array, where some channels did not scan the source at the same moment than the others, because there is a strong correlation of the sky emission in the different channels. The atmospheric noise is then removed by subtracting from the signal of the channels where the source is present the signal of the ones in which this is not the case. The strong correlation of the atmospheric signal in neighboring bolometer channels together with fast and simultaneous sampling in the fast scanning mode is responsible for the fact that the atmospheric noise can be removed very well. The basic *snf* options are given by:
 - * *it 5 0*: number of iterations for the calculation of the correlated skynoise. There are 2 modes of skynoise filtering that can be used. Usually only the first one is taken, which is iterated 5 times. The whole process converges typically after 5 iterations.
 - * *> 5 rms < -5 rms*: despiking like at the beginning. It removes spikes previously hidden in the noise, but which show up after the noise subtraction.
 - * *r 1 900*: defines a search range for correlating channels. Given are an inner and an outer radius in arcseconds from the channel that is going to be corrected. An inner radius of 1'' is defined to exclude self-correlation. The inner radius must be adjusted to the source geometry. This value should be increased to exceed the inner ring of bolometers for not compact sources.
 - * *best 6*: selects only the 6 channels with the best correlation to calculate the noise to subtract.
 - * *no source*: switches off the calculation of the source distribution regarding all parts of the map equally. This option is used when shape and position of the source are still unclear. Later on, a source model with *source-model.gdf* is created. In that case *sb* is added for single beam observations.
- *convert*: puts all single channel maps together according to their noise weight and does the transformation into equatorial coordinates. The iterative version starts with *convert comm* and concludes the command block with *quit*. The iterative version is also used to co-add single maps and so the final map is obtained.
- The flux calibration i.e. the transformation from counts into physical quantities (here Jy) is performed by using a source with known intensity. In this work, Uranus is used. The observing mode was the same as for the MC sources to avoid sensitivity inconsistencies. The distance of a planet varies with time, which affects the source strength. The value of the planet distance is obtained through interpolation from distances available in The Astronomical Almanac. The intrinsic emission is fairly stable and dependent on the surface temperature. Only in rare cases weather phenomena on them (e.g. sandstorms on Mars) can lead to wrong flux estimates. By furnishing the topocentric distance, the telescope, the time of observation, the frequency and the beam

size to the program Planet in MOPSI, the temperature is provided and the flux of the calibrator is derived. The calibrator maps were reduced as the MC sources, but no *despiking* and no *snf* were used and only low order baseline fits were applied. The first should not be done as planets are strong sources and the signal can be destroyed. The resulting maps will be very noisy, but for calibration this is not a problem. Only in the unlikely case of weak or non-detection, *snf* and higher baseline fit after deconvolution are necessary. Conversion factors of (120 ± 16) , (110 ± 14) , (71 ± 11) , (71 ± 11) , (68 ± 9) , (65 ± 10) and (69 ± 3) counts/(mJy beam⁻¹) were derived for July 2001, October 2001, June 2002, August 2002, September 2002, October 2002 and November 2002, respectively. Therefore, the resulting absolute flux density uncertainty ranges from 4% to 15%.

After a preliminary reduction a small amount of bad raw data was eliminated and the whole reduction process of data analysis (rms, S_{peak} , S_{int}) could be started. The rms noise in a map was calculated from regions where no obvious millimeter sources are present. The peak flux density S_{peak} is defined as the maximum value at a given position. The integrated flux density S_{int} was derived considering the source's signal inside the 3σ contour. The diameter was never smaller than the beam size. The rms error is about 5%. The uncertainties in the MOPSI reduction process and the subsequent analysis are estimated to be approximately 10%.

2.6 Contamination of Continuum Flux

The 1.2 mm emission observed with the SIMBA bolometer may originate in principle from thermal dust, free-free and synchrotron emissions as well as molecular lines within the bolometer bandwidth (50 GHz). Table 2.2 gives the list of typical spectral lines, whose rotational transitions can potentially be responsible for continuum flux contamination. But only in rare occasions, the measured continuum flux has a contribution coming from spectral line emission which is non-negligible - that means more than a few percent. Only in such cases, the measured values should be corrected for line contamination.

Table 2.2: List of typical molecular transition lines covered by the SIMBA bolometer.

| Wavelength (bolometer) | molecular line | ν [GHz] | λ [μm] |
|----------------------------|------------------------|-------------|-----------------------------|
| 1200 μm (SIMBA) | ¹² CO(2-1) | 230.5 | 1300 |
| | ¹² CS(5-4) | 244.9 | 1225 |
| | HCN(3-2) | 265.9 | 1130 |
| | HCO ⁺ (3-2) | 267.6 | 1120 |
| | HNC(3-2) | 272.0 | 1100 |

Braine et al. (1995) found that the line contribution to the total continuum flux is given by the ratio

$$\frac{S_{\text{line}}}{S_{\text{total}}} = \frac{2k\nu^3 c^{-3} \int_{\text{line}} T_{\text{mb}} dv \int_{\text{beam}} 2\pi r \exp(-4 \ln 2 (r^2/\theta^2)) dr}{S_{\nu} \Delta\nu_{\text{bol}}} \quad (2.2)$$

$$\frac{S_{\text{line}}}{S_{\text{total}}} = \frac{2k\nu^3 c^{-3} 2\pi\theta^2 / (8 \ln 2) \int_{\text{line}} T_{\text{mb}} dv}{S_{\nu} \Delta\nu_{\text{bol}}} \quad (2.3)$$

$$\approx 2.73 \times 10^{-9} \frac{\nu^3 \theta^2 \int_{\text{line}} T_{\text{mb}} dv}{S_{\nu} \Delta\nu_{\text{bol}}}, \quad (2.4)$$

where k is the Boltzmann constant, ν [GHz] the frequency of the spectral line, $\int_{\text{line}} T_{\text{mb}} dv$ [K km s⁻¹] the line intensity, θ the half power beamwidth (HPBW) of the bolometer in arcseconds, S_{ν} [mJy] the integrated flux density and $\Delta\nu_{\text{bol}}$ [GHz] the bolometer bandwidth. For $\nu = 250$ GHz, $\theta = 23''$ and $\Delta\nu = 50$ GHz at the SEST this leads to a contribution of

$$\frac{S_{\text{line}}}{S_{\text{total}}} \approx 0.450 \frac{I_{\text{CO}(2-1)}}{S_{1200}}. \quad (2.5)$$

The contribution of other lines in the bolometer bandwidth are negligible compared to the total observed flux.

The synchrotron ($S_{\nu} \propto \nu^{-0.6}$) and the free-free emission ($S_{\nu} \propto \nu^{-0.1}$) at 250 GHz make up, specially the latter, a non-negligible contribution in several HII regions of the MCs. This conclusion is based on the comparison of the SIMBA data with the radio continuum measurements of the same regions of Haynes et al. (1991) and, in the case of one region (30 Dor A), on the comparison with the radio data of Peck et al. (1997).

2.7 IRAS Data

The MCs have been observed at four wavelengths (12, 25, 60 and 100 μm) by IRAS during the all-sky survey. IRAS derived fluxes have a dispersion of about 15%. The images made by combining the IRAS survey scans furnish $\sim 5'$ of angular resolution in the MCs for all four wavelength bands. This map production, by averaging the partly overlapping data samples, is called co-addition and among the results obtained with this technique is the IRAS Sky Survey Atlas, so-called ISSA (Wheelock et al. 1994). High-resolution images of the MCs from the IRAS survey data base have been constructed through a maximum entropy algorithm by Braun et al. (1998).

The HIRAS program (Bontekoe, Koper & Kester 1994) was used to obtain the high-resolution IR maps of the MCs from the IRAS all-sky survey data. This program uses the Pyramid Maximum Entropy (PME) method - an application of the maximum entropy software package MemSys5 (Gull & Skilling 1991) - in order to construct reliable images at a resolution approaching the diffraction limit of the IRAS telescope. In the PME algorithm the image is constructed in a number of parallel images, containing respectively 1 by 1, 2 by 2, 4 by 4, 8 by 8 pixels, etc up to the final pixel number. Each image covers the whole map area and represents a certain correlation length or resolution size. The images are combined into a single image and its entropy is calculated as the sum of the entropies of the individual images. Maximizing the entropy assures that large scale structure is preferentially constructed in a channel image with large pixels. The angular resolution of the MC maps constructed through the MemSys5 algorithm is increased by a factor of about three, when compared to the co-addition method, that means an average of $\sim 1.4 - 1.5'$, while the large scale structures are also conserved.

For more details on IRAS data calibration and pre-processing see Assendorp et al. (1995) and Bontekoe, Koper & Kester (1994).

The positions and fluxes of the high-resolution 100 μm IRAS images of the MCs obtained through the maximum entropy method by the former cited researchers were used together with the 1.2 mm data to determine the dust temperature and mass of the sources sampled (see Chapters 3 and 4). The 12, 25 and 60 μm data were used together with the 100 μm and 1.2 mm ones to obtain the FIR luminosity L_{FIR} (see Chapter 6).

Chapter 3

Dust Observations in the LMC

3.1 Observed Regions in the LMC

Nine regions in the LMC were selected as part of the 1.2 mm continuum emission measures and observed with SIMBA at the SEST during July and October 2001 and September, October and November 2002.

The CO emission of the LMC revealed that it is concentrated in a huge complex of molecular clouds associated with 30 Dor. Therefore, six of the selected regions belong to the Central or the Southern parts of the 30 Doradus Complex which were studied in CO by Johansson et al. (1998). The N 44 complex, the N 113 and the N 214 nebulae were also investigated.

In this chapter a description of the individual regions with positive detections as well as the results of the 33 detected sources are presented.

The positions for the epoch 2000.0 for the 21 sources of the 30 Dor complex are given in Columns 2 and 3 of Table 3.1. Column 4 lists the major and minor axes (pc) and Column 5 presents the area (pc²). The corresponding measured peak (mJy/beam) and integrated flux densities (mJy) at 1.2 mm are presented in Columns 6 and 7, respectively. For the 12 sources of the other LMC regions the same is displayed in Table 3.4.

3.1.1 30 Doradus

There are only few irregular and spiral galaxies with giant HII regions and luminous stellar clusters as spectacular as 30 Doradus, also called N 157 (Henize 1956), DEM 263 (Davies, Elliott & Meaburn 1976) and Tarantula Nebula (Fig. 3.1), in the LMC.

The Tarantula Nebula is the only extra-galactic nebula that can be seen with the unaided eye. Its structure consists of a bright core, a highly condensed cluster of extremely young blue stars, and an extended outer region dominated by intersecting arcs of ionized hydrogen. However, the precise boundary is difficult to be established. This extended complex contains many regions that show signs for recent and ongoing star formation. The estimated diameter is 15' (200 pc), much larger than any known region in the Galaxy, containing several thousand OB stars and more than $8 \times 10^5 M_{\odot}$ of ionised gas, with a central cluster diameter of 40 pc

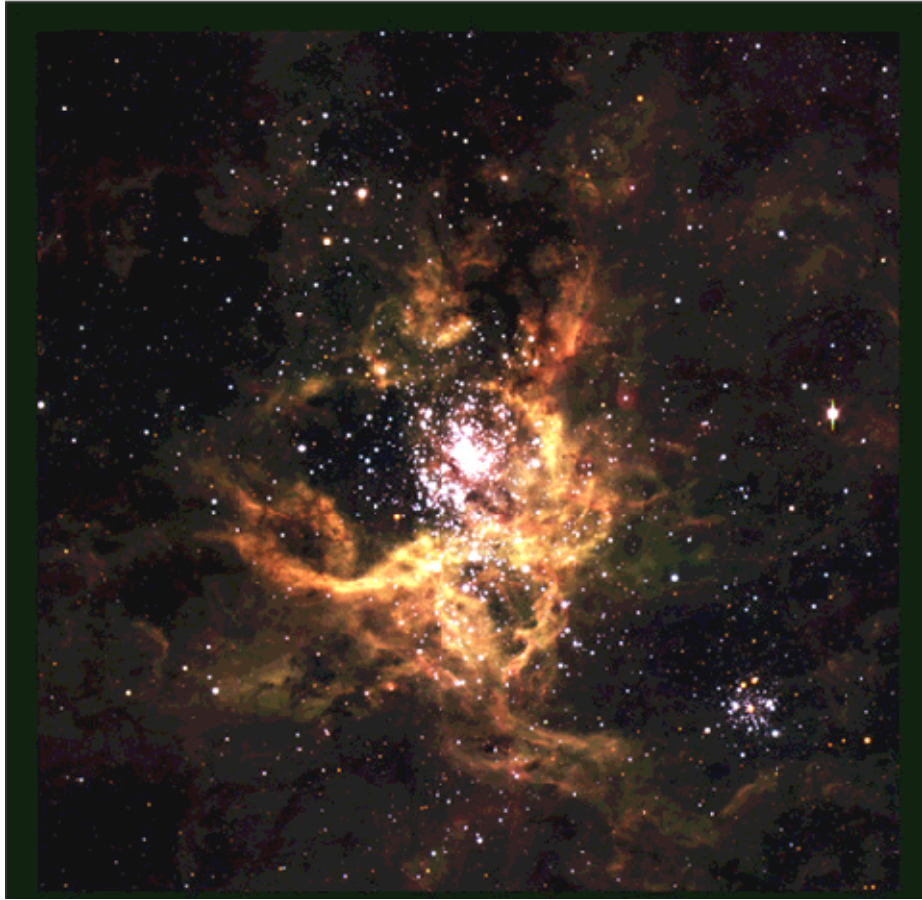


Figure 3.1: Tarantula Nebula in the LMC (VLT astronomical photos from ESO).

(Walborn 1991). The bolometric luminosity of the inner 4.5 pc cluster's core is $\sim 8 \times 10^7 L_{\odot}$ (Malamuth & Heap 1994). Filamentary structures known as SGS LMC 2 and SGS LMC 3, respectively, are located to the east and west of the central nebula N 157.

The 30 Dor region is very rich in HII, HI, CO and dust. The dust seen as FIR emission has been observed with IRAS (12, 25, 60 and 100 μm). The most luminous stars in the central cluster of 30 Dor have reached the WN (Wolf-Rayet stars with enhanced N abundance) stage, indicating an age of $(2-3) \times 10^6$ yr (Walborn et al. 1999). The excitation source of the ionized gas in the 30 Dor nebula is the rich cluster R136 (HD 38268) in its core. Melnick (1985) concluded that R136 contains enough hot luminous stars to provide the Lyman continuum photons required to explain the ionization of the HII region with no need for the presence of an exotic object in the cluster's core. R136 is an unusually high concentration of massive and bright O, B and Wolf-Rayet (WR) stars (Brandl et al. 1997). The total mass in stars $\geq 2.8 M_{\odot}$ is $2.0 \times 10^4 M_{\odot}$ at a radius of 4.7 pc (Hunter et al. 1995). The most luminous - and presumably the most massive - stars in the R136 region are the individual components of R136a. Their ZAMS masses are probably around 50 M_{\odot} (de Marchi et al. 1993).

Elliott et al. (1977) obtained photographs in $H\alpha$, $H\beta$, [OIII], [NII] and 5672 \AA continuum for the region in question. They concluded that the 30 Dor HII region is produced by ionization

fronts eating into neutral material with small scale nebulous filaments in the nebula's core being bright rims on the interfaces between the neutral and the ionized matter. The $H\alpha$ luminosity in the boundary of the 30 Dor A region found by Kennicutt et al. (1995) is 5.7×10^{39} erg/s. 30% of the LMC flux comes from a region of radius $30'$ centered on 30 Dor and more than half within a $90'$ radius (Kennicutt et al. 1995).

Fitzpatrick & Savage (1984) found that all 30 Dor stars appear to be reddened by $E(B-V) \approx 0.12$ with an extinction law similar in wavelength dependence to those derived in previous investigations of LMC reddening. Several of the stars are additionally reddened by $E(B-V) \approx 0.18$ with an extinction law qualitatively similar in wavelength dependence to the law found in the Orion region. The explanation raised was a two-component model featuring a layer of "LMC foreground dust" which affects all stars and a deeper layer of "nebular dust" which affects some of the stars. The 2175 \AA extinction bump is present in both the LMC-type and the nebular-type extinction laws. The bumps' wavelength positions and their profiles are indistinguishable from the Galactic one. The strengths of the bumps are 20%-30% weaker than for the Milky Way curve. A regional variation of the extinction in the LMC is not supported by several studies such as Nandy et al. (1981). Hill et al. (1993) observed that most stars within the high surface brightness area centered near R136 have low nebular extinction ($E(B-V) < 0.03$), while stars outside this area typically have $E(B-V) < 0.3$. Dust grains following the nebular extinction curve may have been expelled from the central regions of 30 Dor by stellar winds, or stars in the outer regions may be behind or within dust clouds. Greve, Castles & McKeith (1991) derived the average extinction $\langle A_v \rangle = 1.35 \pm 0.10$ mag in the direction of 30 Dor.

Several studies such as Hyland et al. (1992) identified candidate "protostars" in the region. NIR (JHK) images taken by Rubio, Roth & Garcia (1992) show that, though the overall appearance of 30 Dor coincides with the optical morphology, several highly reddened objects are found. Some of them correspond to "protostars" already reported in the literature while others seem to be tracers of recent massive star formation.

There are indications that two regions of 30 Dor have different IMF (initial mass function) slopes: in the SE region the IMF is fitted by the slope $\Gamma = -1.7$, whereas in the NW region (including R136), where most of the recent star formation activity takes place, the curvature problem dominates and the most massive bins might be not completely included. The latter can have one or two reasons: i) WR stars are omitted because if they were added it would make a considerable impact since there are so few stars in the most massive bins; ii) O stars with temperatures determined only by photometry may have been placed in too low mass bins (Parker & Garmany 1993). The intermixed stellar population of the inner region of 30 Dor of M supergiants and WN and OB stars suggests that at least two major bursts of star formation have occurred in the last 10 Myr (Westerlund 1997).

The giant HII region has a complex kinematics with the velocity field being dominated by a large number of expanding structures which are often organized in hierarchical networks. Also several shells expanding at high velocities were identified. The latter and the network coincide with extended X-ray sources which are probably associated with supernova remnants (SNRs) from the OB associations. Wang & Helfand (1991) presented a detailed X-ray emission analysis of the 30 Dor star formation complex finding a strong correlation between X-ray, radio and optical morphologies. The entire complex can be understood if the huge molecular

Table 3.1: Axes, area, peak and integrated flux densities of the 30 Dor complex sources measured from the (sub)millimeter maps. The peak flux density is defined as the maximum value at the given position.

| Source | α_{2000} [h m s] | δ_{2000} [° ' "] | axes ^{a)} [pc] | area ^{b)} [pc ²] | S_{peak} ^{c)} [mJy/beam] | S_{int} ^{d)} [Jy] |
|--------------|----------------------------|----------------------------|----------------------------|--|---|--|
| 30Dor MMS 1 | 05:38:32.9 | -69:02:14 | 33 x 19 | 463 | 224 ± 31 | 1.3 ± 0.2 |
| 30Dor MMS 2 | 05:38:47.6 | -69:04:50 | 56 x 48 | 1810 | 880 ± 123 | 8.8 ± 1.4 |
| 30Dor MMS 3 | 05:38:36.3 | -69:05:30 | 35 x 11 | 311 | 480 ± 67 | 2.0 ± 0.3 |
| 30Dor MMS 4 | 05:38:32.8 | -69:06:13 | 32 x 30 | 701 | 624 ± 87 | 3.7 ± 0.6 |
| 30Dor MMS 5 | 05:38:42.2 | -69:07:15 | 30 x 17 | 308 | 176 ± 25 | 0.8 ± 0.1 |
| 30Dor MMS 6 | 05:37:28.0 | -69:08:45 | 9 x 9 | 64 | 66 ± 9 | 0.1 |
| 30Dor MMS 7 | 05:37:46.5 | -69:10:05 | 17 x 12 | 120 | 132 ± 18 | 0.4 ± 0.1 |
| 30Dor MMS 8 | 05:37:49.0 | -69:11:03 | 21 x 17 | 239 | 198 ± 28 | 0.7 ± 0.1 |
| 30Dor MMS 9 | 05:35:36.0 | -69:12:15 | 12 x 11 | 75 | 108 ± 15 | 0.2 |
| 30Dor MMS 10 | 05:35:49.6 | -69:12:50 | 25 x 8 | 157 | 108 ± 15 | 0.5 ± 0.1 |
| N158 MMS 1 | 05:39:08.4 | -69:30:07 | 20 x 13 | 204 | 150 ± 21 | 0.6 ± 0.1 |
| N158 MMS 2 | 05:39:02.9 | -69:30:33 | 22 x 10 | 173 | 150 ± 21 | 0.5 ± 0.1 |
| N158 MMS 3 | 05:39:15.5 | -69:30:39 | 32 x 17 | 330 | 240 ± 34 | 1.2 ± 0.2 |
| N159 MMS 1 | 05:40:04.9 | -69:44:34 | 50 x 37 | 1144 | 342 ± 48 | 3.7 ± 0.6 |
| N159 MMS 2 | 05:39:36.0 | -69:45:25 | 22 x 19 | 265 | 414 ± 58 | 1.2 ± 0.2 |
| N159 MMS 3 | 05:39:38.1 | -69:46:09 | 37 x 26 | 489 | 306 ± 43 | 1.3 ± 0.2 |
| N159 MMS 4 | 05:39:28.5 | -69:47:13 | 19 x 15 | 200 | 108 ± 15 | 0.4 ± 0.1 |
| N160 MMS 1 | 05:39:45.1 | -69:38:35 | 37 x 20 | 610 | 504 ± 71 | 2.1 ± 0.3 |
| N160 MMS 2 | 05:39:39.2 | -69:39:00 | 32 x 24 | 715 | 324 ± 45 | 2.0 ± 0.3 |
| N160 MMS 3 | 05:40:24.6 | -69:40:12 | 19 x 15 | 174 | 108 ± 15 | 0.3 |
| N160 MMS 4 | 05:40:10.2 | -69:40:32 | 15 x 11 | 130 | 90 ± 13 | 0.2 |

a) Both axes were obtained considering the signal starting at 3σ .

b) In general, the sources have an irregular shape.

c) The uncertainty of S_{peak} comes from the errors in the conversion factors and in the rms (Chapter 2).

d) For the errors of S_{int} see in Chapter 2 the uncertainties of the conversion factors (calibration) and of the MOPSI (reduction and analysis).

cloud, which embeds supergiant shell SGS LMC 2, swept through the LMC after the collision with the SMC ~ 0.2 Gyr ago (Fujimoto & Noguchi 1990) and arrived at its current position about 50 Myr ago. The leading edge stopped in the 30 Dor position, possibly because of a collision between SGS LMC 2 and SGS LMC 3. The expansion stop towards the west caused the formation of a ridge of HII regions south of 30 Dor. Such ridge contains dust, hydrogen, CO, plasma which emits diffuse X-rays and also has multiple signs of ongoing star formation. N 158C, N 159 and N 160 in the southern region outstand among the star forming giant HII regions (Westerlund 1997). De Boer et al. (1998) propose as star formation scenario in the LMC an external trigger. In its motion through the halo of our Galaxy, the LMC gas is compressed at the leading edge. Star formation is triggered in the gas that is being compressed at the leading edge due to the bow-shock of the LMC. The favored location is at

the SE side. Near the leading edge of the LMC is located the high pressure X-ray emitting area (pressure more than 10 times the average of the rest of the galaxy in question), which is aligned and adjacent to the molecular spur that extends southward of 30 Dor. It seems reasonable that these clouds have or will have in the near future stars forming at a very high rate.

3.1.2 Observations in the 30 Doradus central area

The 1.2 mm emission in the central field of 30 Dor, measured during July and October 2001, overlaid on a DSS2-red plate is shown on Fig. 3.2. The coincidences with dark nebulae (DN) (Hodge 1988) in the 30 Dor central field and their Lynds opacity class are listed in Table 3.2.

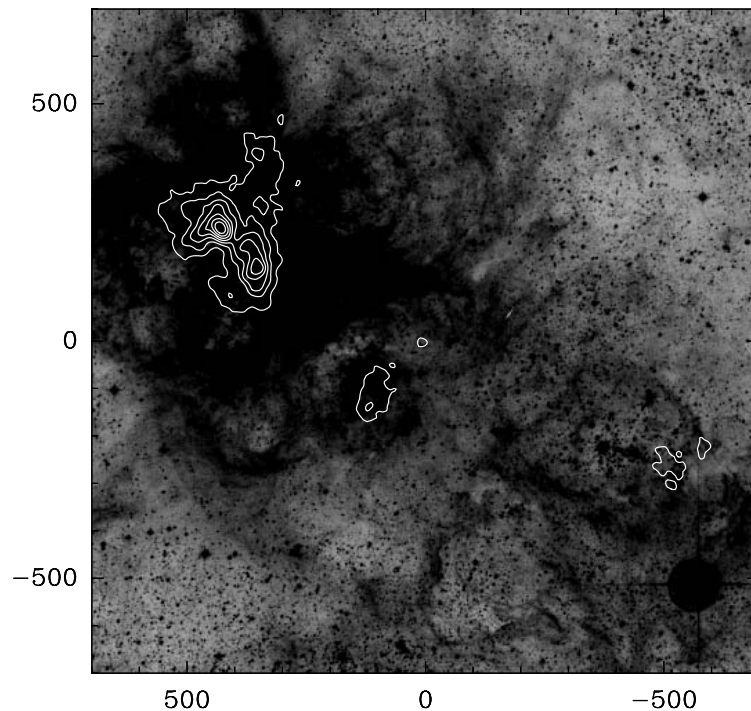


Figure 3.2: 30 Dor central field 1.2 mm emission overlaid on the DSS2-red plate from the ESO Online Digitized Sky Survey. Field center is 05:37:27.0 -69:08:50 (J2000) and the offset is in arcsec. Contours are 60 mJy/beam to 900 mJy/beam in steps of 120 mJy/beam. North is up and east is left. The contours in the upper left belong to 30 Dor A, in the center to 30 Dor B and in the lower right to 30 Dor C.

30 Doradus A

30 Dor A coincides with the stellar association LH 100 (Lucke & Hodge 1970). Other common designations for the 30 Doradus core include: NGC 2070 (Hodge & Wright 1967) and N 157A

Table 3.2: 30 Dor central area 1.2 mm sources and line-of-sight associated dark nebulae (Hodge 1988).

| 30Dor sources | D. N. | Lynds class |
|---------------|------------|-------------|
| 30Dor MMS 1 | 87 | 2 |
| 30Dor MMS 2 | 88, 93, 95 | 5, 5, 5 |
| 30Dor MMS 3 | 84, 85 | 5, 5 |
| 30Dor MMS 4 | 84, 85 | 5, 5 |
| 30Dor MMS 5 | 84, 85 | 5, 5 |
| 30Dor MMS 6 | 64, 67 | 5,4 |
| 30Dor MMS 8 | 77 | 3-5 |
| 30Dor MMS 9 | 49 | 3* |
| 30Dor MMS 10 | 49 | 3* |

* Only part of its extension is studied.

(Henize 1956).

Fig. 3.3 shows the 1.2 mm contour map of the 30 Dor A region centered on the emission nebula N 157A with the contours starting at 3σ . The SIMBA detections show an Ω - shaped region encircling R136. The final map, rms of 16 mJy/beam, has been created from 17 single maps with a total integration time of about 8.5 hours. It shows five dust clouds (30 Dor MMS 1 - 5) well in agreement with the contours of $^{12}\text{CO}(1-0)$ (Johansson et al. 1998) and $^{12}\text{CO}(2-1)$ (Rubio 2002). Extended emission is also detected in the SIMBA measures (about 10% of the S_{int} observed in 30 Dor A, $S_{\text{int}} \simeq 1.9$ Jy). It is located between 30 Dor MMS 1 and 2, and presents lower contours than the five dust clouds. However in the CO(1-0) and CO(2-1) contours there are no extended emission between 30 Dor-06 (30 Dor MMS 1) and 10 (30 Dor MMS 2).

The group of (sub)millimeter sources stretches out over $4'20'' \times 6'20''$ and is located in the immediate vicinity of the stellar cluster R136 which dominates the visual appearance.

Infrared images (Schwering 1988) show a bright extended emission associated with the SIMBA sources. Hyland et al. (1992) discovered four "protostellar" objects from NIR observations, three of which are located in the northeastern quadrant, and the other in the western one. All the four are associated with dense knots in the nebular arcs and have luminosities of $(1-5) \times 10^4 L_{\odot}$ and masses of 15-20 M_{\odot} . The "protostars" turned out to be the brightest in the numerous stellar IR sources found with subsequent instrumentation (e.g. Rubio et al. 1998).

30 Dor MMS 2 - the strongest detected source in the present study - is located north of R136 and coincides with the radio source MDM 72 detected in the 1.4 GHz survey, carried out with an angular resolution of $7''$ by Marx, Dickey & Mebold (1997), which can be identified with the 6 cm radio continuum source MC 74 from McGee, Brooks & Batchelor (1972) ($4'$ resolution). The associated molecular cloud is called 30 Dor-10 (Johansson et al. 1998) and has one of the highest CO intensities between the sources of the 30 Dor central field, N 158 and N 160 which were detected by SIMBA. Rubio et al. (1998) detected a great number of IR sources through JHK observations in the MMS 2 region - their northeast field (part of it

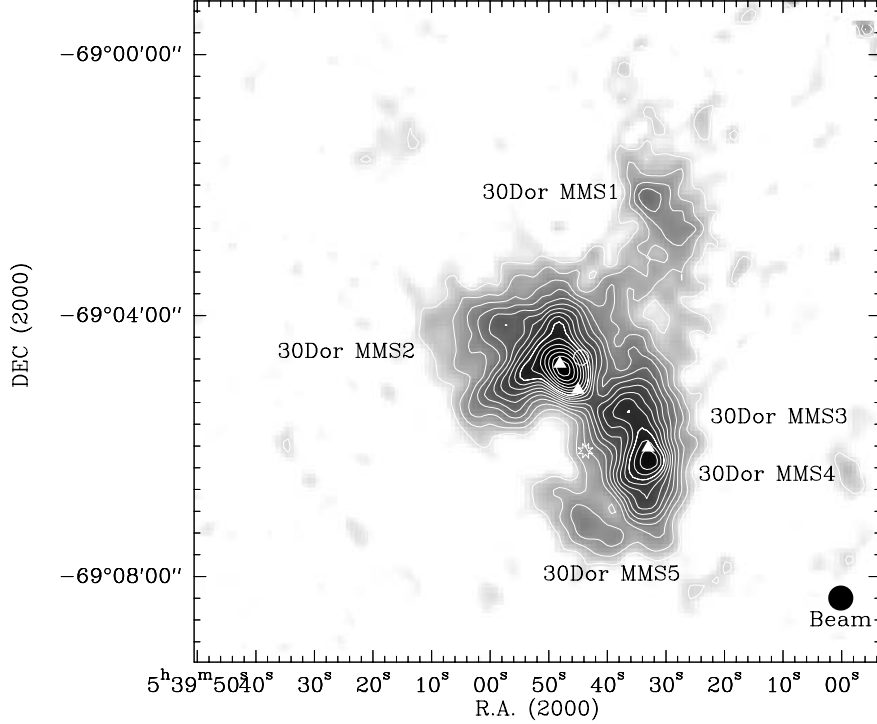


Figure 3.3: 30 Doradus A in 1.2 mm continuum obtained with a resolution of about $23''$ (HPBW). Contours are 48 mJy/beam (3σ) to 480 mJy/beam in steps of 48 mJy/beam and 480 mJy/beam to 900 mJy/beam in steps of 60 mJy/beam. The circle marks the position of the radio source MDM 72 (Marx, Dickey & Mebold 1997), the triangles at the center, east and west, respectively, that of Knots 1, 2 and 3 (Walborn & Blades 1987, Walborn 1991) and the star that of the stellar cluster R136.

is also in 30 Dor MMS 3) - indicating that the formation of a new stellar generation has been triggered by the massive central cluster R136. The limiting magnitudes of the observations performed by Rubio et al. (1998) were 17 - 18. In addition, the 22-GHz H_2O maser 0539-691 (Whiteoak & Gardner 1986) and the SNR 0539-69.1 (Forest, Spenny & Johnson 1988) seem to be associated with 30 Dor MMS 2. Walborn & Blades (1987) found two early O-type stars - within the range O3 - O6V - apparently involved in dense nebular knots in the northeastern quadrant of 30 Dor A. Knot 1 lies on the brightest ridge of nebulosity in the entire HII region, while Knot 2 lies within the positional error of the H_2O maser.

30 Dor MMS 4 - the second strongest SIMBA source in this region - is located west of R136 and coincides with another population of IR sources of Rubio et al. (1998) - their west field (part of it is also in 30 Dor MMS 3). Walborn (1991) reported a third essentially identical stellar/nebular knot to those found by Walborn & Blades (1987). Knot 3 is located immediately west of R136.

Walborn & Blades (1997) increased to 11 the number of early O stars embedded in dense

nebular knots, classified O3 - O6 V closely associated spatially to the IR sources of Rubio et al. (1998).

30 Dor MMS 5 is the weakest source in the region shown in Fig. 3.3. Brandner et al. (2001) presented the detection of candidate class I sources and Herbig Ae/Be T-Tauri stars in the 30 Dor nebula, one of them located to the south of R136.

The H₂O maser, the early O stars embedded in dense nebular knots, the "protostars" of Hyland et al. (1992) and the IR sources of Rubio et al. (1998) changed the view of the 30 Doradus A as a well evolved HII region to a scenario that its evolution is a two-stage starburst. The region where these very young massive stars may be just emerging from their protostellar cocoons is in an earlier evolutionary stage than the central region surrounding R136.

30 Doradus B

30 Dor B (NGC 2060 - Hodge & Wright 1967) is located on the southwest periphery with a distance of about 7' from the 30 Doradus nebula's core and coincides with the stellar association LH 99 of Lucke & Hodge (1970). That this region contains a rich population of early O stars was first shown in the extensive survey of Schild & Testor (1992).

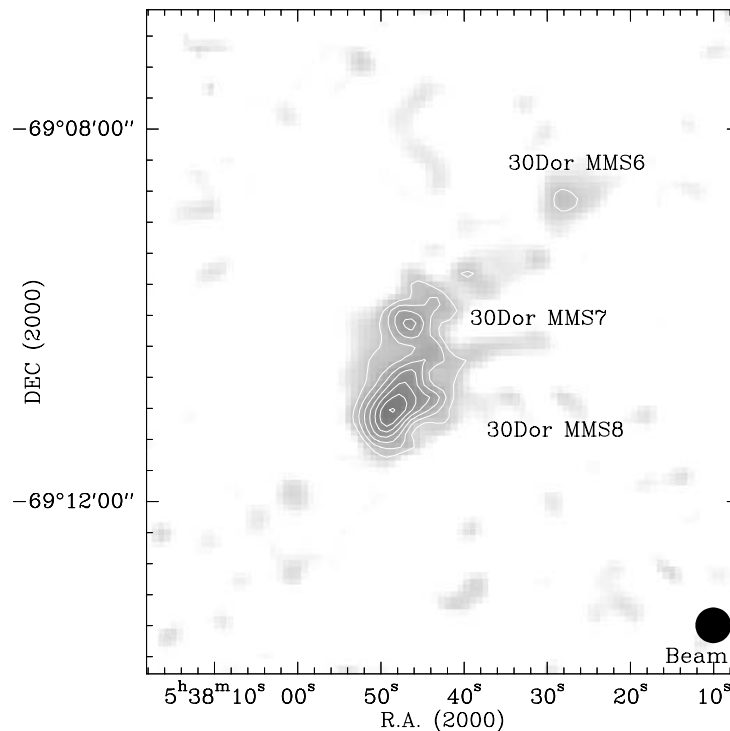


Figure 3.4: 30 Doradus B area in 1.2 mm continuum obtained with a resolution of about 23'' (HPBW). Contours are 66 mJy/beam (3σ) to 198 mJy/beam in steps of 22 mJy/beam.

Fig. 3.4 displays the 1.2 mm contour map and is centered on the emission nebula N 157B

(Henize 1956) with the contours starting at 3σ . The final map has a rms of 22 mJy/beam and was created from nine single maps with a total integration time of about 4.5 hours. The contour map shows three well-defined dust clouds (30 Dor MMS 6 - 8). Two of them are in agreement with the contours of two CO sources (Johansson et al. 1998). The other dust detection is in between.

30 Dor MMS 8 - the strongest (sub)millimeter source in the N 157B area - has an elongated morphology. Together with the source 30 Dor MMS 7 it is associated with SNR 0538-69.1 (Forest, Spenny & Johnson 1988). Marshall et al. (1998) found a 16 ms X-ray pulsar associated with this supernova remnant.

30 Doradus C

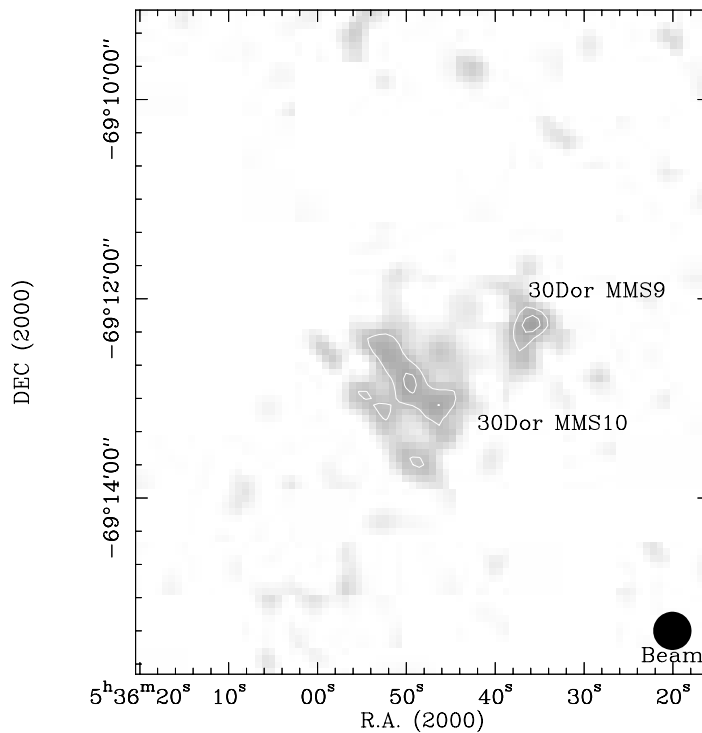


Figure 3.5: 30 Doradus C area in 1.2 mm continuum obtained with a resolution of about $23''$ (HPBW). Contours are 81 mJy/beam (3σ) to 108 mJy/beam in steps of 27 mJy/beam.

Located further west of 30 Dor A and 30 Dor B, at the outer edge of the 30 Dor nebula (distance to the center of 240 pc), 30 Dor C (NGC 2044 - Hodge & Wright 1967) coincides with the stellar association LH 90 (Lucke & Hodge 1970) that contains several tight clusters of OB stars. It is peculiarly rich in WR stars and has been investigated by several authors (e.g. Lortet & Testor 1984, Schild & Testor 1992). Chu & Kennicutt (1988) identified the SNR 0536-69.2 as falling within the boundary of the OB association LH 90. However, Chu (1997) suggested that SNR 0536-69.2 is caused by one or more SNRs shocking the inner walls of the superbubble blown by LH 90. Walborn et al. (1999) concluded that the age of NGC

2044 is 1 - 1.5 Myr. The 6 cm radio continuum source MC 69 (McGee, Brooks & Batchelor 1972) also coincides with 30 Dor C.

Figure 3.5 shows the 1.2 mm emission of the complex region 30 Dor C near SN 1987A with the contours starting at 3σ (rms of 27 mJy/beam). It has been created from eight single maps with a total integration time of about four hours. The contour map shows that there are two well-defined dust clouds in the area (30 Dor MMS 9 - 10).

30 Dor MMS 10 - the strongest SIMBA source in this region - has a clearly elongated morphology. Comparing with the contours of $^{12}\text{CO}(1-0)$ (Johansson et al. 1998) the 30 Dor MMS 10 is associated with two CO sources.

3.1.3 30 Doradus southern HII regions

N 158, N 159 and N 160 are part of the chain of HII regions south of the central area of 30 Dor. The 1.2 mm emission in the southern field was measured during July 2001. Overlaid on a DSS2-red plate this emission is shown in Fig. 3.6.

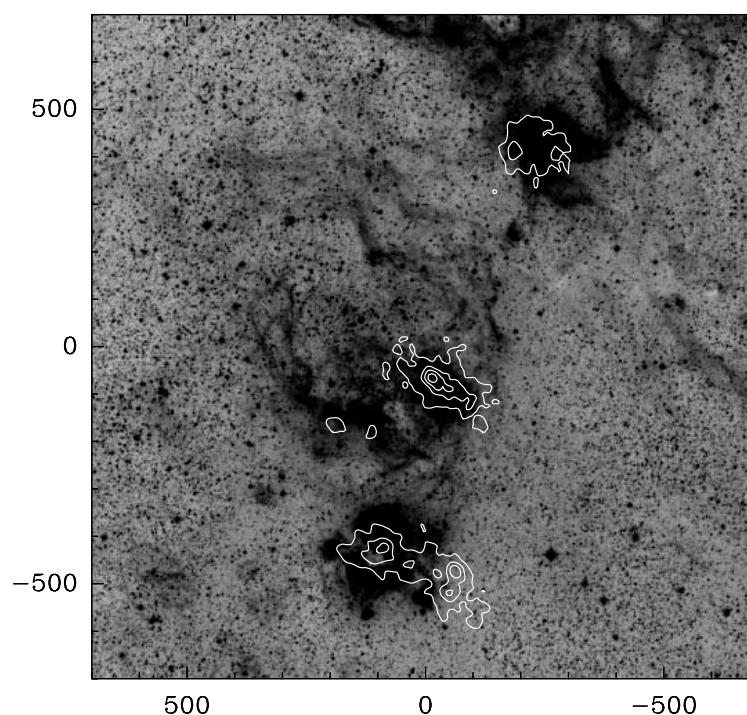


Figure 3.6: Southern field 1.2 mm emission overlaid on the DSS2-red plate from the ESO Online Digitized Sky Survey. Field center is 05:39:50.0 -69:37:40 (J2000) and the offset is in arcsec. Contours are 60 mJy/beam to 540 mJy/beam in steps of 120 mJy/beam. North is up and east is left. The contours seen from north to south belong to the sequence N 158, N 160 and N 159.

N 158C

Located about $20'$ south of the nucleus of 30 Doradus, N 158 (Henize 1956) is the northernmost in this chain. Also called DEM 269 by Davies, Elliott & Meaburn (1976) this bright HII region covered by the SIMBA observations coincides with the stellar association LH 101 in Lucke & Hodge (1970) (NGC 2074 - Hodge & Wright 1967) and with MC 75 (McGee, Brooks & Batchelor 1972, from 6 cm observations). LH 101 is dominated by unevolved and evolved O-type massive stars thus suggesting that this region is an active site of very massive star formation. It consists of at least two age groups, one with an age of ≤ 2 Myr and the other one aged 3 - 6 Myr (Testor & Niemela 1998).

Fig. 3.7 displays the 1.2 mm emission, with the contours starting at 3σ , showing three dust clouds (N 158 MMS 1 - 3) with an elongated morphology. The contour map has been created from 12 single maps during a total integration time of about 6 hours. The final map has a rms of 30 mJy/beam. The dust contours of all three sources are in agreement with the contours of $^{12}\text{CO}(1-0)$ (Johansson et al. 1998).

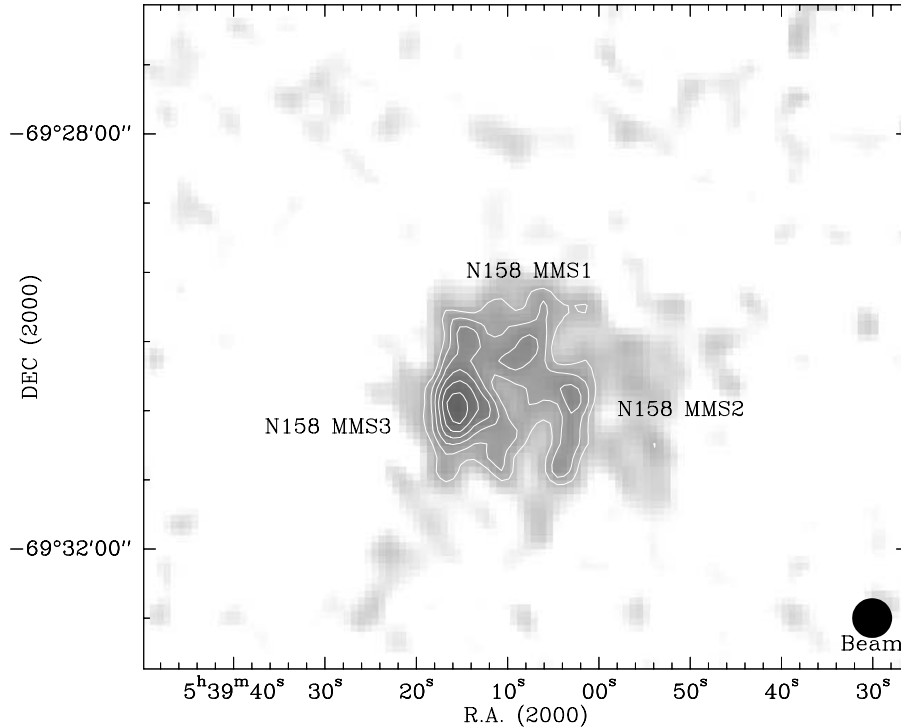


Figure 3.7: The southern HII region N 158C in 1.2 mm continuum obtained with a resolution of about $23''$ (HPBW). Contours are 90 mJy/beam (3σ) to 300 mJy/beam in steps of 30 mJy/beam.

N 158 MMS 2 - the weakest SIMBA source in this area - is associated with the dark nebula 94 which is of the Lynds opacity class 3 - 5 (Hodge 1988).

N 158 MMS 3, associated with the dark nebula 108 (Lynds opacity class 1 - Hodge 1988), is

the strongest SIMBA source in this area. Jones et al. (1986) detected two faint sources in the NIR associated to the position of this source. Also associated to N 158 MMS 3 is the IR detection LI-LMC 1490 (Schwering & Israel 1990), which is a blend of two components.

N 159/N 160

This complex, first cataloged by Henize (1956), is one of the best studied LMC star forming regions in molecular and atomic transitions (e.g. Heikkilä, Johansson & Olofsson 1999). These nebulae are two of the brightest HII regions in the immediate vicinity of the 30 Dor central area and are located $\sim 40'$ to its south. Davies, Elliott & Meaburn (1976) give them in their emission line nebulae survey the numbers 271 and 284, respectively.

The N 159/N 160 region has three different and spatially well separated areas:

- The northern part associated with the N 160 nebula, where massive star formation is well evolved and the parent clouds have been mostly photodissociated and dissipated.
- The central region associated with the N 159 nebula, which is undergoing strong star formation activity but is still involved in molecular gas. This region includes two giant molecular clouds (GMCs) known as N 159E and N 159W.
- The southern region featuring the molecular cloud N 159S (Bolatto et al. 2000). The latter cloud is the beginning of the 30 Dor CO ridge region, a ~ 900 pc long spur extending southward of the 30 Dor nebula (Kutner et al. 1997, Sorai et al. 2001).

The brightest component in N 159 is the nebula N 159A (Henize 1956), which contains in its center the star called DD 13. According to Heydari-Malayeri & Testor (1982) DD 13 may be a tight cluster. Deharveng & Caplan (1991) presented 14 O - B2 stars in the HII region N 159A and concluded that it is ionized by a pair of stars of spectral types O5V (or O6V) and O7V (or O8V). They also showed the existence of two distinct age groups in the N 159A region: a young stellar population and an older one made of giants, aged 10^9 yr or more.

$3'$ NE of N 159A is located the high excitation compact ($\sim 6''$) HII "blob" (HEB) N 159-5. It was the prototype of this category of nebulae (Heydari-Malayeri & Testor 1982).

Scalise & Braz (1981) discovered an H₂O maser in the direction of N 159. The N 159 region contains the high mass X-ray binary source LMC X-1 (Rapley & Tuohy 1974, Johnston et al. 1978).

Boreiko & Betz (1991) observed the CII emission towards 17 positions (from which seven were in N 159, two in N 160, one in N 158 and five others in the 30 Dor central area) in the LMC. They found a good spatial correlation between FIR continuum and CII emission, as expected when the dust emission comes from a relatively dense region near early-type stars.

The correlation between locations of strong CII and CO emission is poor. Boreiko & Betz (1991) pointed out that no CII emission was detected in N 159 where the ¹²CO(1-0) line has been mapped by Booth et al. (1989) and none in N 160A where ¹²CO(2-1) was observed by Israel et al. (1986). The absence of significant CII emission approximately $5.5'$ south of N 159 may be explained by star formation in the 30 Dor complex propagating southward with the current activity most intense near N 159. Until the activity extends further south the CO in the region will remain cold and with no newly formed OB stars, CII will not be abundant.



Figure 3.8: $H\alpha$, $[O III]$ and $H\beta$ color composite image from the HII region N 160A taken with the WFPC2 on board HST. The field size is $67'' \times 67''$ (Heydari-Malayeri homepage).

The N 159 complex consists of three CII major peaks surrounded by weaker emission. The westernmost peak coincides with N 159A. In N 159 the eastern and western peaks have respectively 15 pc and somewhat smaller displacements from the CO maxima. The central one has no associated CO emission at all. In N 159 the eastern and western radio peaks coincide with the CII peaks. The central radio peak is about 20 pc of the central CII peak. N 160 has a bright CII peak surrounded by a large region of lower surface brightness. In N 160 the CII peak is displaced about 15 pc NE from the CO maximum. The N 160 radio core is displaced by another 15 pc further NE from the CII peak (Israel & Maloney 1993).

The N 159 region covered by the SIMBA observations coincides with the stellar association LH 105 of Lucke & Hodge (1970) (NGC 2078 - Hodge & Wright 1967).

Rubio, Roth & Tapia (1990) found in N 159 15 IR sources through J, H and K images, thus indicating that the region is a site of active star formation. Several of these objects have IR colors which are typical of re-emission by dust. Also IR extended emission is seen surrounding a compact IR cluster containing 4-5 sources.

The region N 160, as covered by the SIMBA observations, contains the OB association LH 103 which embodies 41 blue stars (Lucke & Hodge 1970, Lucke 1974). MC 76 (McGee, Brooks & Batchelor 1972, from 6 cm observations) (NGC 2080 - Hodge & Wright 1967 - also nicknamed the Ghost Head Nebula) is a strong radio continuum source associated with the optical nebula N 160A (Henize 1956), which is the brightest component in the N 160 complex.

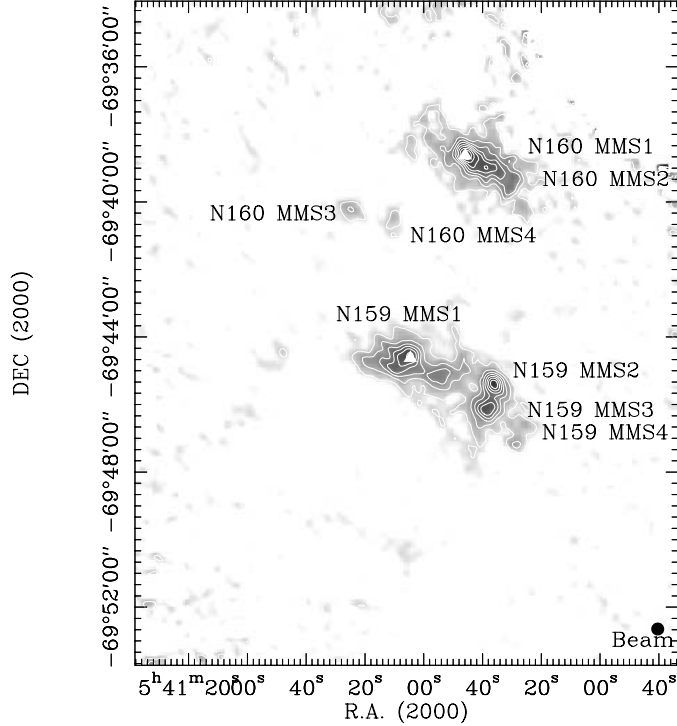


Figure 3.9: The southern HII region N 159 and N 160 in 1.2 mm continuum obtained with a resolution of about $23''$ (HPBW). Contours are 54 mJy/beam (3σ) to 540 mJy/beam in steps of 54 mJy/beam. The triangles in N 160 and N 159 mark the positions of the radio sources MDM 75 and MDM 78, respectively (Marx, Dickey & Mebold 1997).

Two other HEBs found in the LMC are associated to N 160A. One of them is apparently powered by a massive star (at least O7.5 - O8V) (Heydari-Malayeri et al. 2002).

Through observations in the NIR and MIR, Epchtein, Braz & Sevre (1984) reported the detection of a probable "protostellar" object in N 160A near a 22-GHz H_2O maser, which is called 0540-696 (Whiteoak & Gardner 1986). An OH maser at 1.665 GHz (ground-state) was observed in N 160A by Caswell & Haynes (1981). $50''$ SW of the peak of the HII region N 160A Caswell (1995) detected an OH maser at 6.035 GHz which is at the location of a 3 mJy continuum radio source, probably a weak HII region. It is similar to several Galactic objects.

Heydari-Malayeri et al. (2002) carried out photometry of the brighter than 21 mag stars towards the HII region N 160A at 2911, 4090, 4669 and 5479 \AA with the Hubble Space Telescope (HST). They also obtained the $\text{H}\alpha/\text{H}\beta$ Balmer decrement which shows that the dust is rather "patchy" with the content increasing westward (Fig. 3.8).

Fig. 3.9 displays the 1.2 mm map of the N 159/N 160 complex showing eight dust clouds (N 159 MMS 1 - 4 and N 160 MMS 1 - 4). This figure, with the contours starting at 3σ , has been created from 34 single maps during a total integration time of about 17 hours and the

rms of the final map was 18 mJy/beam.

Huggins et al. (1975) first detected CO ($J = 1 - 0$) emission in the LMC in N 159. The dust contours of the sources N 159 MMS 1 (N 159E), N 159 MMS 2 - 3 (N 159W) and N 159 MMS 4 (N159-2) are in agreement with the contours of $^{12}\text{CO}(1-0)$ (Johansson 1991, Johansson et al. 1998) and $^{12}\text{CO}(2-1)$ (Bolatto et al. 2000). The (sub)millimeter sources N 160 MMS 1 - 2 show an elongated morphology and their dust contours are in agreement with the contours of $^{12}\text{CO} (1 - 0)$ (Johansson et al. 1998) and $^{12}\text{CO} (2 - 1)$ (Bolatto et al. 2000).

N 159 MMS 1 - the strongest SIMBA source in the N 159 region - shows an elongated morphology and coincides with the radio source MDM 78 detected in the 1.4 and 2.4 GHz surveys by Marx, Dickey & Mebold (1997), which can be identified with the 6 cm source MC 77 (McGee, Brooks & Batchelor 1972). Using ROSAT X-ray observations Chu et al. (1997) resolved the SNR 0540-697 in this region. Gatley et al. (1981) and Jones et al. (1986) reported from NIR observations the existence of a "protostellar" object which is located near the position of N 159 MMS 1.

N 159 MMS 3 is the second strongest SIMBA source in the N 159 region. Schwering & Israel (1990) observed the complex in IR and revealed the detection LI-LMC 1501, which is a blend of two components, in the direction of N 159 MMS 2 - 3. Jones et al. (1986) also reported the existence of a "protostar" which is located near the position of N 159 MMS 3. This "protostar" is probably associated to one of the sources of the IR cluster in Rubio, Roth & Tapia (1990).

N 160 MMS 1, the strongest (sub)millimeter source in the N 160 region, coincides with the radio source MDM 75 detected in the 1.4 and 2.4 GHz surveys by Marx, Dickey & Mebold (1997) (other identification: MC 76).

3.1.4 Detections and non-detections in the 30 Dor complex

Table 3.3: Non-detections and corresponding 1σ rms noise.

| Source | σ_{1200} [mJy/beam] | Source | σ_{1200} [mJy/beam] |
|-----------|-------------------------------|-----------|-------------------------------|
| 30 Dor-01 | 21 | 30 Dor-23 | 22 |
| 30 Dor-03 | 22 | 30 Dor-24 | 22 |
| 30 Dor-04 | 22 | 30 Dor-31 | 16 |
| 30 Dor-05 | 16 | 30 Dor-32 | 16 |
| 30 Dor-07 | 22 | 30 Dor-33 | 16 |
| 30 Dor-08 | 22 | N 159-1 | 18 |
| 30 Dor-14 | 16 | N 159-S | 18 |
| 30 Dor-16 | 16 | N 159-3 | 18 |
| 30 Dor-18 | 22 | N 160-6 | 18 |

The continuum observations that have been carried out towards 30 Dor and its southern HII regions lead to the following results: for 38 sources of CO observed, chosen between the

detections from Johansson et al. (1998), 20 have dust continuum data. The detections were described in the former subsections, while Table 3.3 lists the subsample of the non-detections.

In the 30 Dor central area there are several molecular clouds with relative weak CO features (e.g. 30 Dor-33) as well as others with strong ones (e.g. 30 Dor-08) which presented no detection in the 1.2 mm continuum observations.

In the N 159 area the CO line emission peaks at N 159-W, N 159-E and N 159-S with N 159-1 and 3 being among the SIMBA non-detections.

The most prominent CO sources studied by Johansson et al. (1998), with the exception of the N 159-S molecular cloud, are associated with massive star formation. This is shown by the association with star formation tracers such as star clusters, dark nebulae, protostellar objects, OH and H₂O masers, supernova remnants and 6 cm radio sources. On the contrary, N 159-S lacks signs of ongoing star formation activity and appears to be a cold, more quiescent cloud. The absence of dust in this region is one more evidence of this scenario.

In the N 160 area the strongest CO feature is denoted N 160-4 by Johansson et al. (1998) and around this position the dust detections are concentrated. N 160-6 is a molecular cloud far more south.

In order to have a more conclusive idea of the (sub)millimeter continuum features of the non-detection areas, a deeper integration would be necessary.

Table 3.4: Axes, area, peak and integrated flux densities of the N 44, N 113 and N 214 sources measured from the (sub)millimeter maps. The peak flux density is defined as the maximum value at the given position.

| Source | α_{2000} [h m s] | δ_{2000} [° ' "] | axes ^{a)} [pc] | area ^{b)} [pc ²] | S_{peak} ^{c)} [mJy/beam] | S_{int} ^{d)} [Jy] |
|------------|----------------------------|----------------------------|----------------------------|--|---|--|
| N44 MMS 1 | 05:22:28.4 | -67:54:43 | 22 x 22 | 314 | 110 ± 15 | 0.7 ± 0.1 |
| N44 MMS 2 | 05:22:01.7 | -67:57:53 | 33 x 30 | 782 | 390 ± 55 | 2.0 ± 0.3 |
| N44 MMS 3 | 05:22:11.2 | -67:58:31 | 22 x 22 | 389 | 310 ± 43 | 1.4 ± 0.2 |
| N44 MMS 4 | 05:23:07.8 | -67:59:59 | 28 x 17 | 432 | 70 ± 10 | 0.5 ± 0.1 |
| N44 MMS 5 | 05:23:14.4 | -68:00:37 | 20 x 16 | 224 | 70 ± 10 | 0.3 |
| N44 MMS 6 | 05:22:52.3 | -68:04:18 | 31 x 22 | 481 | 200 ± 28 | 1.1 ± 0.2 |
| N44 MMS 7 | 05:22:15.8 | -68:04:34 | 18 x 10 | 148 | 50 ± 7 | 0.1 |
| N113 MMS 1 | 05:13:17.5 | -69:22:30 | 38 x 33 | 755 | 420 ± 25 | 2.2 ± 0.2 |
| N113 MMS 2 | 05:13:34.4 | -69:23:02 | 20 x 13 | 209 | 80 ± 5 | 0.3 |
| N113 MMS 3 | 05:13:50.7 | -69:23:35 | 11 x 9 | 66 | 30 ± 2 | 0.1 |
| N214 MMS 1 | 05:39:48.1 | -71:08:31 | 18 x 10 | 141 | 40 ± 6 | 0.1 |
| N214 MMS 2 | 05:39:54.1 | -71:10:00 | 38 x 29 | 650 | 136 ± 22 | 0.8 ± 0.1 |

a) Both axes were obtained considering the signal starting at 3σ .

b) In general, the sources have an irregular shape.

c) The uncertainty of S_{peak} comes from the errors in the conversion factors and in the rms (Chapter 2).

d) For the errors of S_{int} see in Chapter 2 the uncertainties of the conversion factors (calibration) and of the MOPSI (reduction and analysis).

3.1.5 N 44 emission nebula

The interstellar complex called N 44 by Henize (1956) and DEM 150, 151 and 152 by Davies, Elliott & Meaburn (1976) has formed on the edge of a cloud of neutral atomic and molecular gas several hundreds of parsecs across (Meaburn & Laspias 1991). Located near the kinematical (radio) center of the LMC it is an example of a well-studied emission nebula (Fig. 3.10) of the galaxy in question. It contains an assortment of compact HII regions, filaments and shells of all sizes as well as the three OB associations: LH 47, LH 48 and LH 49 (Lucke & Hodge 1970) with their stars energizing the FIR emission detected by IRAS. The presence of HII regions as well as FIR emission indicates recent star formation in the N 44 region. The region is rich in bright emission arcs with the most prominent forming a giant interstellar shell, located in the central region of N 44, which is 70 x 50 pc across and surrounds the OB association LH 47 which contains 40 blue stars (Lucke & Hodge 1970, Lucke 1974). Diffuse HII regions are located in the surroundings and filaments to the east, compact HII regions encompassing LH 49 to the south, a large faint shell to the west, faint filaments to the north, a luminous, compact HII region around LH 48 on the northeast rim of the main shell as well as a great number of small, bright single-star HII regions in the outskirts of N 44 (Kim et al. 1998).



Figure 3.10: B, V and H α color composite photos centered near N44 with the Wide Field Imager (WFI) (ESO press release June 1999).

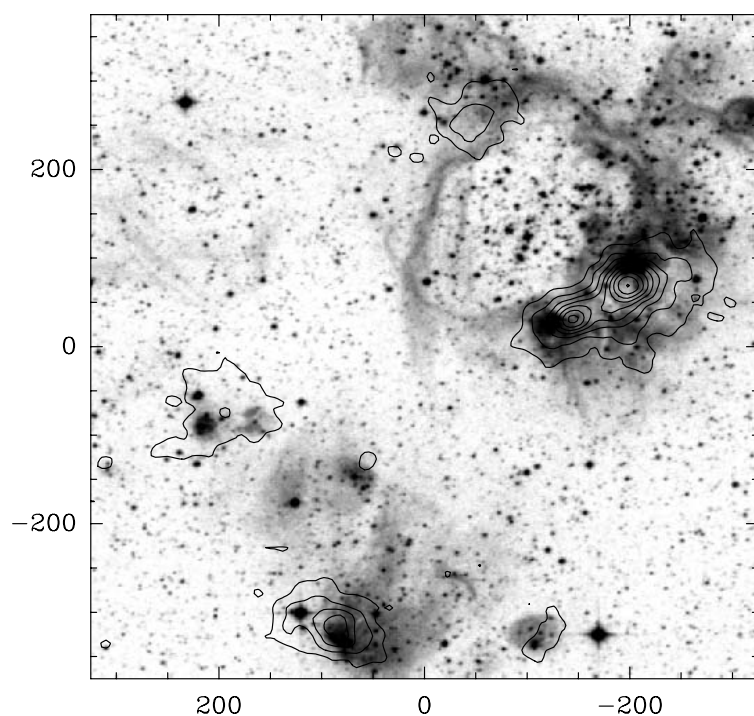


Figure 3.11: N 44 1.2 mm emission overlaid on the DSS2-red plate from the ESO Online Digitized Sky Survey. Field center is 05:22:38.0 -67:59:00 (J2000) and the offset is in arcsec. Contours are 30 mJy/beam to 390 mJy/beam in steps of 45 mJy/beam. North is up and east is left.

Oey & Massey (1995) examined in detail with UBV photometry the stellar population of LH 47/48. The stellar content is essentially Salpeter, therefore being unlikely an exotic population. They found an age distribution which suggests the action of propagating star formation. Regions exterior to DEM 152 have ages < 5 Myr, whereas the interior population have an age ranging up to some 10 Myr (an age estimate of 2 - 4 Myr for LH 47/48 provides only a lower limit for the superbubble's age). With an older population inside DEM 152 and a younger one outside the following scenario is favored: the supershell originates by a roughly symmetrical expansion, which triggers the formation of the younger stellar population on the west side. SNR 0523-679, centered at 05:23:06 -67:53:15 (J2000), is at NE of the emission nebula N 44I (Henize 1956). X-ray observations demonstrated substantial SN activity in LH 47.

Fig. 3.11 displays the detected 1.2 mm emission in the N 44 nebula overlaid on a DSS2-red plate. Fig. 3.12, created from 10 single maps with a total integration time of about 5 hours, shows the 1.2 mm continuum map of the N 44 emission nebula with the contours starting at 3σ (rms of 10 mJy/beam). The contour map shows that there are seven dust clouds (N 44 MMS 1 - 7).

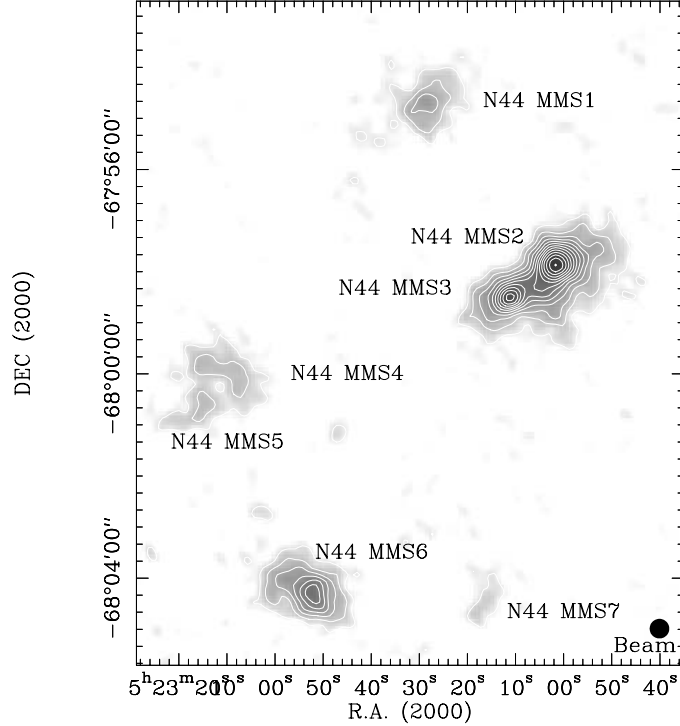


Figure 3.12: The N 44 area in 1.2 mm continuum obtained with a resolution of about $23''$ (HPBW). Contours are 30 mJy/beam (3σ) to 390 mJy/beam in steps of 30 mJy/beam (observations in September 2002).

The detected sources N 44 MMS 1 - 7 coincide, respectively, with the optical emission nebulae N 44I, B, C, L, E, D and GK from Henize (1956).

This region covered by the SIMBA measurements coincides with several stellar associations (Lucke & Hodge 1970): N 44 MMS 1 with the stellar association LH 48 (NGC 1937 - Hodge & Wright 1967), N 44 MMS 2 - 3 (respectively, the strongest and the second strongest (sub)millimeter sources in the N 44 area) with LH 47 (NGC 1929 - Hodge & Wright 1967) and N 44 MMS 6 with LH 49. The N 44 region also matches with 6 cm radio continuum sources in McGee, Brooks & Batchelor (1972): the dust clouds N 44 MMS 2 - 3 with the radio source MC 32 and N 44 MMS 6 with MC 33. The dust contours of the sources N 44 MMS 2 - 3 are in very well agreement with the contours of ^{12}CO (1 - 0) (Chin et al. 1997) and ^{12}CO (2 - 1) (Johansson 2002). The ^{12}CO (1 - 0) peak velocity agrees with the systemic velocity of the HI and HII emission (Kim et al. 1998). Coincident, respectively, with the emission nebulae N 44BC and N 44D, Schwering & Israel (1990) revealed the IR detections LI-LMC 880 and LI-LMC 911. The possibilities to characterize N 44C are: i) radiative ionization by a central star of 7×10^4 K; ii) neutron star or black hole which produce an X-ray photo-ionized nebula (Meaburn & Laspias 1991, Hubble news release 2002-12).

3.1.6 N 113 nebula

N 113, so called by Henize (1956), is projected on the southern part of the LMC Bar (West-erlund 1997). Davies, Elliott & Meaburn (1976) give this region the number 104 in their emission line nebulae survey. This region covered by the SIMBA observations coincides with the stellar association LH 35, which embodies 10 blue stars (Lucke & Hodge 1970, Lucke 1974) (NGC 1874 - Hodge & Wright 1967), and with the 6 cm radio continuum source MC 24 (McGee, Brooks & Batchelor 1972).

Fig. 3.13 displays the detected 1.2 mm emission in the N 113 nebula overlaid on a DSS2-red plate and Fig. 3.14 shows the 1.2 mm emission map of the region with the contours starting at 3σ . The final map, rms of 10 mJy/beam, has been created from 10 single maps with a total integration time of about 4 hours. The contour map shows three well-defined dust clouds (N 113 MMS 1 - 3).

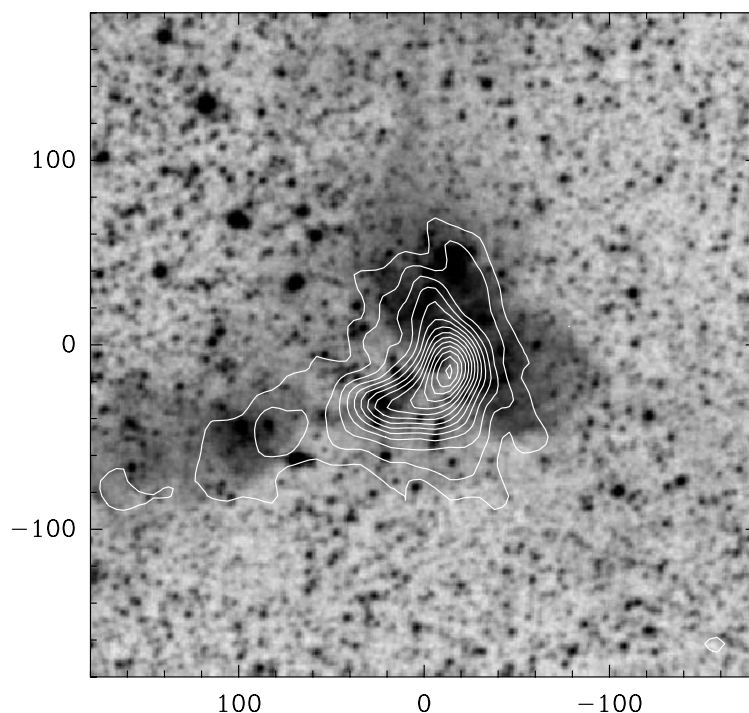


Figure 3.13: N 113 1.2 mm emission overlaid on the DSS2-red plate from the ESO Online Digitized Sky Survey. Field center is 05:13:19.0 -69:22:20 (J2000) and the offset is in arcsec. Contours are 30 mJy/beam to 420 mJy/beam in steps of 30 mJy/beam. North is up and east is left.

N 113 MMS 1 is the strongest (sub)millimeter source in the N 113 area. In the direction of this source is located in IR LI-LMC 635 (Schwering & Israel 1990). Whiteoak & Gardner (1986) reported the detection of a H₂O maser, 0513-694B (by far the brightest in the LMC) which seems to be associated with N 113 MMS 1. Brooks & Whiteoak (1997) detected a

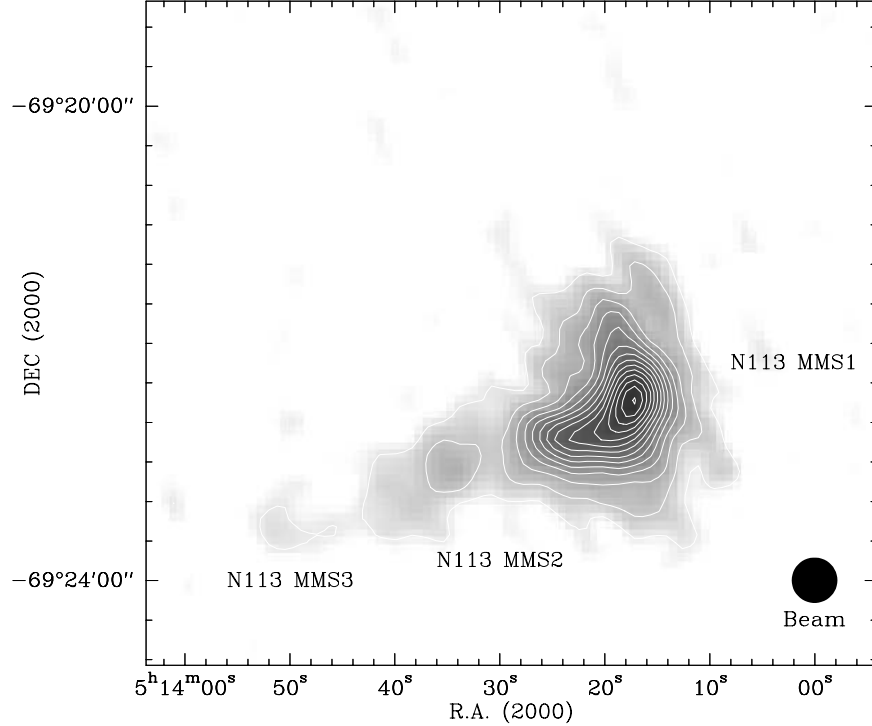


Figure 3.14: The N 113 area in 1.2 mm continuum obtained with a resolution of about $23''$ (HPBW). Contours are 30 mJy/beam (3σ) to 420 mJy/beam in steps of 30 mJy/beam (observations in November 2002).

ground-state OH maser in this cloud region. N 113 MMS 1 is associated with the dark nebula 20 which is of the Lynds class 1 (Hodge 1988).

3.1.7 N 214 nebula

This nebula, called N 214 by Henize (1956) and DEM 274 by Davies, Elliott & Meaburn (1976), is located towards the southern end of the ~ 900 pc long molecular spur which extends southward of 30 Dor.

Fig. 3.15 displays the detected 1.2 mm emission in the N 214 nebula overlaid on a DSS2-red plate. Fig. 3.16 displays the 1.2 mm emission map of the region, with the contours starting at 3σ , showing two well-defined dust clouds (N 214 MMS 1 - 2) with a clearly elongated morphology. The contour map has been created from 19 single maps during a total integration time of about 9 hours. The final map has a rms of 8 mJy/beam.

N 214 MMS 2 is the strongest (sub)millimeter source in this area. Schwering & Israel (1990) observed the complex in IR and revealed the detection LI-LMC 1521 in the direction of this SIMBA source.

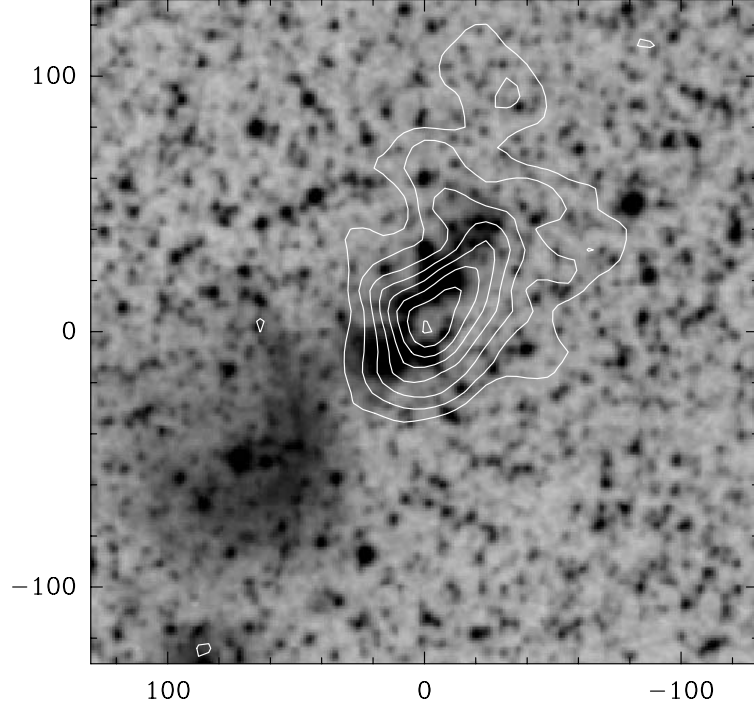


Figure 3.15: N 214 1.2 mm emission overlaid on the DSS2-red plate from the ESO Online Digitized Sky Survey. Field center is 05:39:54.1 -71:10:00 (J2000) and the offset is in arcsec. Contours are 24 mJy/beam to 136 mJy/beam in steps of 16 mJy/beam. North is up and east is left.

3.2 Results

3.2.1 Temperatures

In Chapter 2 it was already mentioned that the 1.2 mm emission might be a superposition of thermal dust emission, molecular lines, synchrotron and/or free-free emission.

In order to estimate the CO contribution two procedures were used: i) In those cases where $^{12}\text{CO}(2-1)$ measurements were available the contribution could be determined directly. ii) For the remaining clouds, where only $^{12}\text{CO}(1-0)$ was available, an intensity ratio I_{2-1}/I_{1-0} was used. The ratio is ~ 1 for the 30 Dor complex as derived from the observations of Johansson et al. (1998); this is in agreement with the value found by Sorai et al. (2001) - who observed (guided by the Cohen et al. (1988) survey, in the $J = 1 \rightarrow 0$ transition) in the $^{12}\text{CO}(2-1)$ transition at lower resolution several positions throughout the LMC disk. The ratio derived by Sorai et al. (2001) for the inner clouds (< 2 kpc from the kinematic center) is also ~ 1 , area which includes N 44 and N 113. The CO data used were from Johansson et al. (1998) (30 Dor complex), Johansson (2002) (N 44) and Israel et al. (1993) (N 113 and N 214). The corresponding contamination is negligible: 20, 6, 5, 11, 52, 19, 33, 18 and 16 mJy,

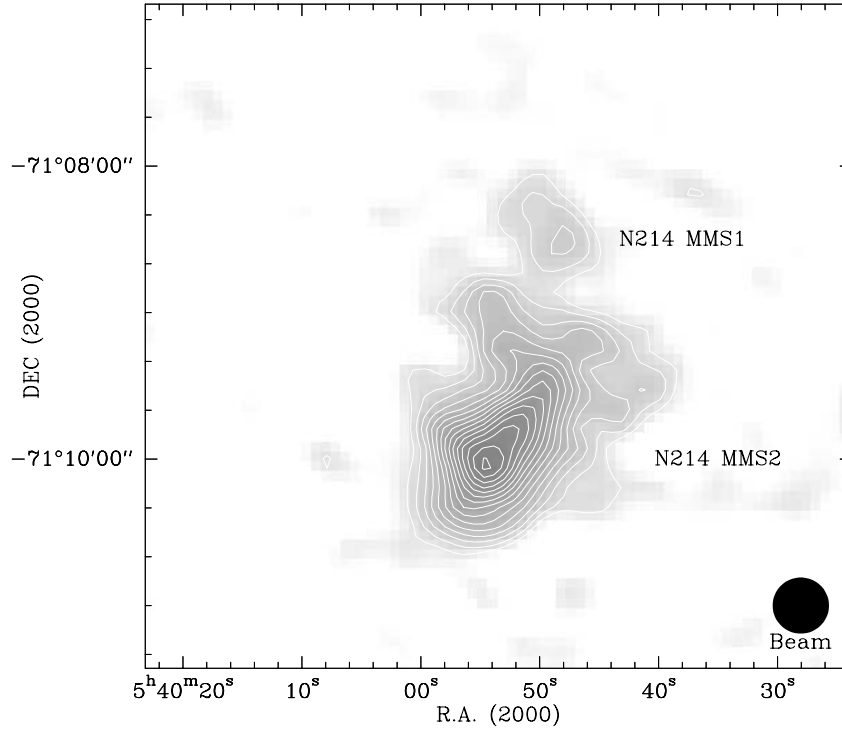


Figure 3.16: The N 214 area in 1.2 mm continuum obtained with a resolution of about $23''$ (HPBW). Contours are 24 mJy/beam (3σ) to 136 mJy/beam in steps of 8 mJy/beam (observations made in October 2002).

respectively, for 30 Dor A, B, C, N 158, N 159, N 160, N 44, N 113 and N 214.

The contribution of other lines like CS, HCN and HCO^+ , as mentioned in Chapter 2, is negligible.

Hendrick & Reynolds (2001) studied 11 SNRs in the LMC to constrain the maximum energies of electron acceleration as some SNRs show evidence for synchrotron emission. But the SNRs located in the regions mapped with SIMBA were not studied by them.

Mills, Turtle & Watkinson (1978) suggested that the emission from the 30 Dor region is entirely thermal i. e. they identified no widespread non-thermal component, apart from the background radiation from the LMC itself. The small amount of non-thermal emission is localized in a number of discrete objects.

The radio data in Peck et al. (1997) from the 30 Dor A area (they measured 14 Jy at 5 GHz with a spatial resolution of $15''$) can be an evidence for a flat spectrum in the radio wavelength regime. However, this does not necessarily mean that the flat spectrum continues to the (sub)millimeter one.

The no observation of dust is a scenario not expected from theory and previous observation results, because cool dust is associated with the molecular rather than the atomic gas phase

and to localize it inside molecular clouds is very probable (see Chapter 1 for more details).

Table 3.5: IRAS fluxes for regions in the LMC.

| Region | S_{IRAS} [Jy] | | | |
|-------------------|------------------------|--------------------|--------------------|--------------------|
| | 12 μm | 25 μm | 60 μm | 100 μm |
| 30 Dor MMS 1 - 5 | 194.4 ± 29.2 | 1089.9 ± 163.5 | 3419.9 ± 513.0 | 3637.8 ± 545.7 |
| 30 Dor MMS 6 - 8 | 2.4 ± 0.4 | 8.7 ± 1.3 | 83.1 ± 12.5 | 102.6 ± 15.4 |
| 30 Dor MMS 9 - 10 | 0.9 ± 0.1 | 1.6 ± 0.2 | 18.0 ± 2.7 | 37.2 ± 5.6 |
| N 158 MMS 1 - 3 | 1.8 ± 0.3 | 4.6 ± 0.7 | 48.2 ± 7.2 | 123.4 ± 18.5 |
| N 159 MMS 1 - 4 | 26.4 ± 4.0 | 110.7 ± 16.6 | 588.1 ± 88.2 | 766.5 ± 115.0 |
| N 160 MMS 1 - 2 | 5.1 ± 0.8 | 13.5 ± 2.0 | 188.8 ± 28.3 | 316.5 ± 47.5 |
| N 160 MMS 3 - 4 | 0.6 ± 0.1 | 1.4 ± 0.2 | 18.9 ± 2.8 | 28.5 ± 4.3 |
| N 44 MMS 1 | 2.7 ± 0.4 | 7.9 ± 1.2 | 64.3 ± 9.6 | 87.2 ± 13.1 |
| N 44 MMS 2 - 3 | 8.2 ± 1.2 | 31.4 ± 4.7 | 185.5 ± 27.8 | 284.2 ± 42.6 |
| N 44 MMS 4 - 5 | 3.2 ± 0.5 | 6.5 ± 1.0 | 52.0 ± 7.8 | 85.4 ± 12.8 |
| N 44 MMS 6 - 7 | 1.8 ± 0.3 | 2.0 ± 0.3 | 29.7 ± 4.5 | 67.6 ± 10.1 |
| N 113 MMS 1 - 3 | 9.9 ± 1.5 | 37.7 ± 5.7 | 203.5 ± 30.5 | 310.3 ± 46.5 |
| N 214 MMS 1 - 2 | 5.3 ± 0.8 | 10.8 ± 1.6 | 66.0 ± 9.9 | 145.2 ± 21.8 |

Table 3.6: Contamination and corrected dust fluxes for regions in the LMC (with extended emission).

| Region | S_{ff} [Jy] | S_{dust} [Jy] | Region | S_{ff} [Jy] | S_{dust} [Jy] |
|-------------------|----------------------|------------------------|-----------------|----------------------|------------------------|
| 30 Dor MMS 1 - 5 | 9.8 ± 0.9 | 8.7 ± 3.1 | N 44 MMS 1 | - | 0.7 ± 0.1 |
| 30 Dor MMS 6 - 8 | 0.8 ± 0.1 | 0.5 ± 0.2 | N 44 MMS 2 - 3 | 2.0 ± 0.2 | 1.4 ± 0.6 |
| 30 Dor MMS 9 - 10 | - | 0.7 ± 0.1 | N 44 MMS 4 - 5 | - | 0.8 ± 0.1 |
| N 158 MMS 1 - 3 | 1.4 ± 0.1 | 0.9 ± 0.4 | N 44 MMS 6 - 7 | 0.8 ± 0.1 | 0.4 ± 0.2 |
| N 159 MMS 1 - 4 | 4.6 ± 0.4 | 2.0 ± 1.2 | N 113 MMS 1 - 3 | 1.1 ± 0.1 | 1.5 ± 0.3 |
| N 160 MMS 1 - 2 | 2.9 ± 0.3 | 1.2 ± 0.8 | N 214 MMS 1 - 2 | 0.4 | 0.5 ± 0.2 |
| N 160 MMS 3 - 4 | 0.3 | 0.2 ± 0.1 | | | |

The synchrotron emission contribution and/or the free-free emission contribution to the measured 1.2 mm flux of the different sources could be estimated from the corresponding radio continuum measurements at 2.45 GHz, 4.75 GHz and 8.55 GHz (Haynes et al. 1991). The HPBW of the 2.45, 4.75 and 8.55 GHz data are $8.9'$, $4.4'$ and $2.8'$, respectively. The mean value of about -0.1 was verified in the spectrum. The extrapolation to the (sub)millimeter wavelength regime was performed with $S_{\nu} \propto \nu^{-0.1}$ (only free-free emission) as the synchrotron emission showed up to be negligible.

In order to get an estimate of the dust temperature, the following procedure was undertaken:

- For reasons described in Chapter 1 (at these wavelengths the grains are in thermal equilibrium with the ISRF) the combination of IRAS 100 μm and 1.2 mm data is a method used to find the dust temperature T_{d} . The SIMBA data is combined with

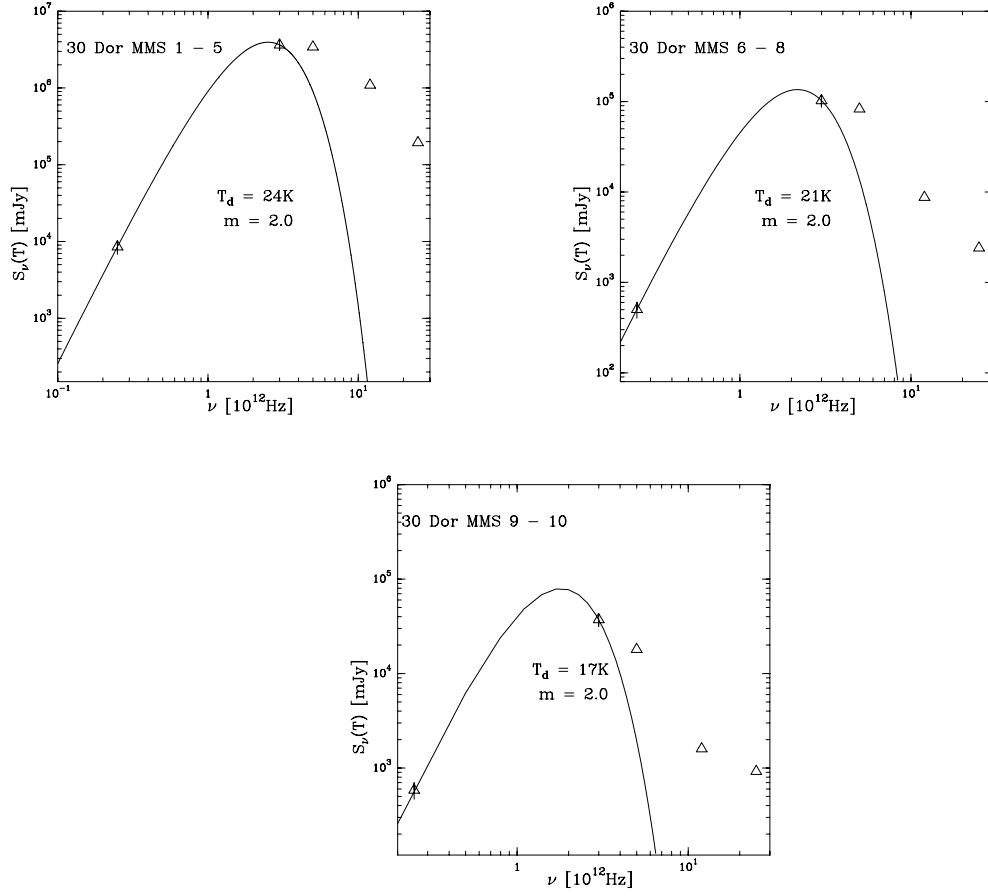


Figure 3.17: SED of the sources detected with SIMBA in 30 Dor A, B and C.

the 100 μm IRAS high-resolution images constructed by Braun et al. (1998) (see Table 3.5). The spatial resolution at 100 μm is only $2.4'$ and does not allow the determination of individual IRAS fluxes for all SIMBA sources. The fluxes of the aggregate regions listed in Table 3.5 at 100 μm and 1.2 mm were integrated over identical spatial areas.

- The contamination to the 1.2 mm flux obtained by extrapolation of the radio data is presented in Table 3.6. The cleaned up 1.2 mm flux is shown in the same table.
- The combined SED of the individual sources are then displayed in Fig. 3.17 - 3.19. The complementary data - IRAS 12, 25 and 60 μm - are also shown (see Table 3.5). In a SED the measured flux density of a source is plotted versus the wavelength or frequency furnishing an estimate of the temperature range and the whole emitted energy. The data points at 100 μm and 1.2 mm are fitted by a modified black-body curve of the form $\nu^m B_\nu(T_d)$ ($m = 2$) (the general method is explained in Chapter 1).

Under these assumptions and within the observational errors (ranging from 4% to 15% for

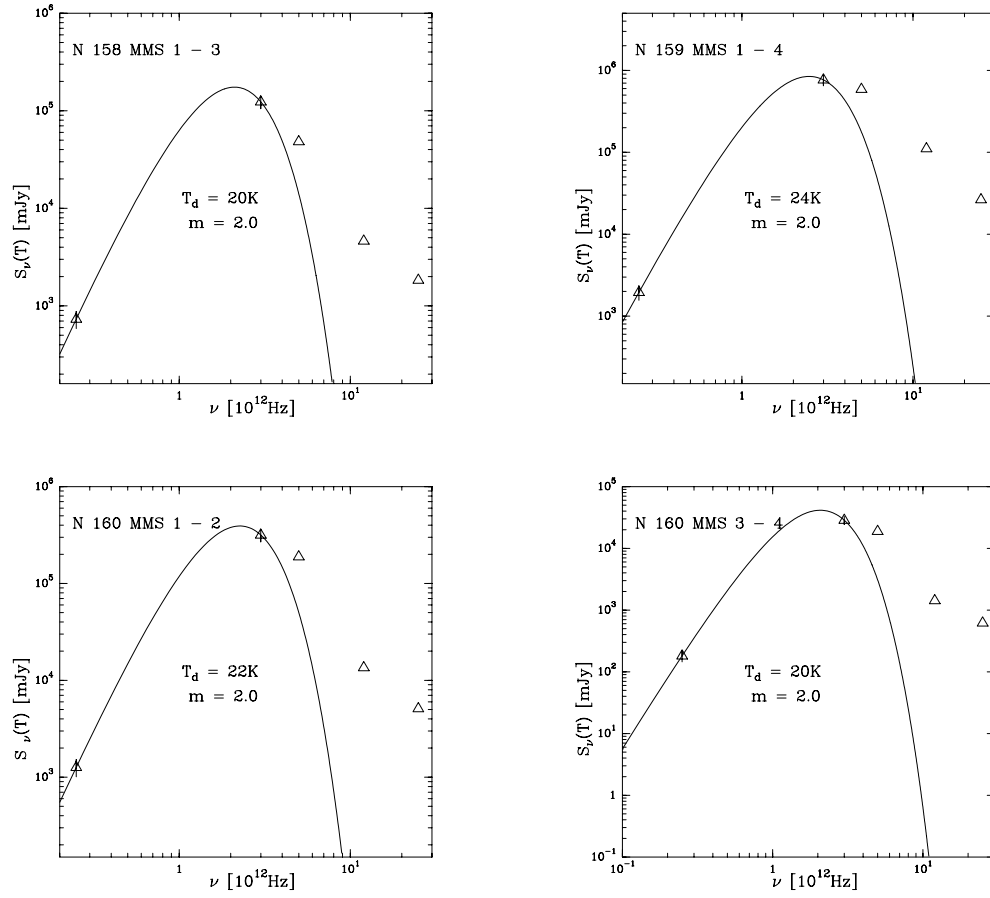


Figure 3.18: SED of the sources detected with SIMBA in N 158C, N 159 and N 160.

SIMBA's calibration, about 10% for MOPSI, 15% for IRAS and for the radio data about 9%) a dust temperature for the different regions is derived:

- 30 Dor A: 24 ± 5 K
- 30 Dor B: 21 ± 2 K
- 30 Dor C: 17 ± 1 K
- N 158: 20 ± 2 K
- N 159: 24 ± 5 K
- N 160 MMS 1 - 2: 22 ± 3 K
- N 160 MMS 3 - 4: 20 ± 2 K
- N 44 MMS 1: 19 ± 1 K
- N 44 MMS 2 - 3: 21 ± 2 K

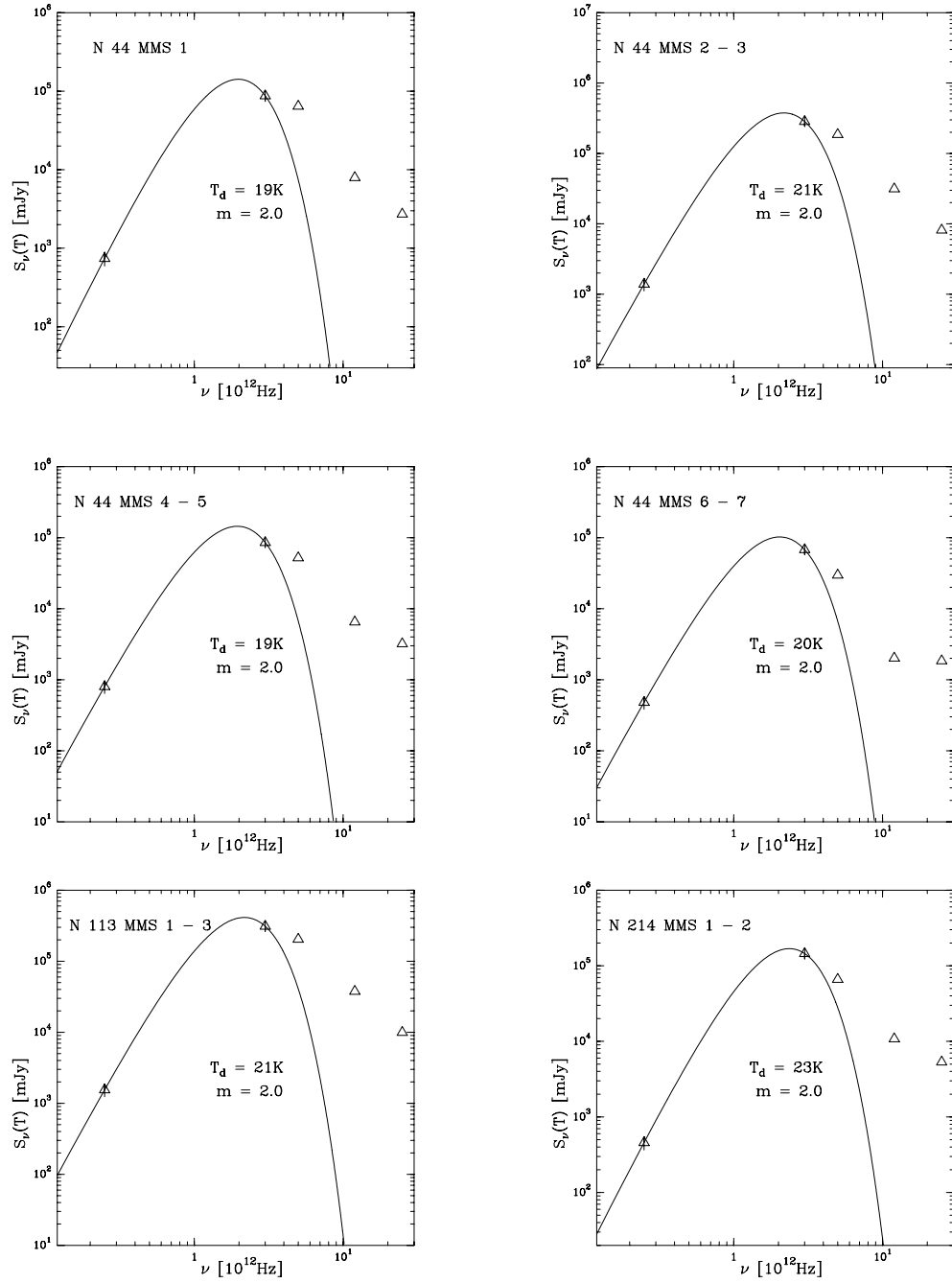


Figure 3.19: SED of the sources detected with SIMBA in N 44, N 113 and N 214.

- N 44 MMS 4 - 5: 19 ± 1 K
- N 44 MMS 6 - 7: 20 ± 2 K
- N 113: 21 ± 2 K
- N 214: 23 ± 4 K

Schwering (1988) found from the 100/60 μm ratio map in LMC HII regions dust temperatures between 32 and 45 K. It is expected that the 100/60 μm ratio furnishes a higher temperature than the 1.2 mm/100 μm one. At 60 μm not only thermal radiation can be measured, because at this wavelength large grains do not dominate. The in SIMBA prominent 30 Dor region is also very well distinguishable in the maps of Schwering. So, a mixture of warm ($25 \text{ K} < T_d < 50 \text{ K}$) and cool ($10 \text{ K} < T_d < 25 \text{ K}$) dust (see the above derived temperatures of this work) can be verified in this area. On the contrary of the SMC, in the LMC the here studied regions have in general a good agreement between the 100 μm and 1.2 mm maps.

The dust temperatures of the HII regions vary between 17 and 24 K. So the existence of dust colder than 20 K in the LMC is confirmed here. The region with the coldest dust (30 Dor C) has its dust sources located on the periphery of the OB cluster LH 90. In the other regions the temperatures range from 19 to 24 K. The highest temperatures (24 K) are verified in 30 Dor A and N 159. The former is close to the rich stellar cluster R136 and previous studies suggest that the maximum of star formation south of 30 Dor is located near N 159.

3.2.2 Masses

In order to derive the dust masses of the different sources presented before the general method explained in Chapter 1 is used (more precisely Eq. (1.17)).

Under the assumptions presented in Chapter 1 a dust mass for the different sources is derived. The uncertainties in the mass estimates vary from 20% to 70%, which originate on one hand from observational (SIMBA) and reduction-related errors (MOPSI) as well as from errors concerning the free-free/synchrotron extrapolation. On the other hand, the dust temperature derived from modified Planck fits to the 1.2 mm and IRAS data introduces another range of uncertainties. The results are shown in Table 3.7.

30 Dor A: (30 Dor MMS 1 - 5) - a total mass of $M_d = (7.8 \pm 3.7) \times 10^3 M_\odot$ is obtained for the entire region in Fig. 3.3. Assuming the average temperature of 24 K to hold for the whole region, the individual dust masses of 30 Dor A given in Table 3.7 are obtained. The result means that the strongest source - 30 Dor MMS 2 - has about 50% of the mass. The sum of the cloud masses is close to the total dust mass, implying that about 10% of the total emission of this area comes from diffuse material.

Obviously, the cluster R136 dominates the radiation field, the ionization and the dynamics of the 30 Dor A region. As the dust cloud 30 Dor MMS 1 is the source of the area shown in Fig. 3.3 with the largest distance from R136 it can be colder than the other regions.

The total mass M_d and the relative contribution of the strongest source of each of the other studied regions are shown next (with the assumption that the temperature holds for all the sources in a region):

30 Dor B: (30 Dor MMS 6 - 8) - Fig. 3.4

$$M_d = (5.4 \pm 2.3) \times 10^2 M_\odot \quad \text{30 Dor MMS 8: 60\%}$$

30 Dor C: (30 Dor MMS 9 - 10) - Fig. 3.5

$$M_d = (1.1 \pm 0.2) \times 10^3 M_\odot \quad \text{30 Dor MMS 10: 70\%}$$

Table 3.7: Dust masses of the individual dust clouds (extended emission subtracted), taking into account only free-free emission contribution (in the sources where contamination was detected). The CO cloud numbers are taken from Johansson et al. (1998) and Israel et al. (1993) (see Table 2.1).

| Source | $M_d[M_\odot]$ | CO cloud |
|--------------|-----------------------------|----------|
| 30Dor MMS 1 | $(5.5 \pm 2.6) \times 10^2$ | 30Dor-06 |
| 30Dor MMS 2 | $(3.7 \pm 1.8) \times 10^3$ | 30Dor-10 |
| 30Dor MMS 3 | $(8.4 \pm 4.0) \times 10^2$ | |
| 30Dor MMS 4 | $(1.6 \pm 0.8) \times 10^3$ | 30Dor-12 |
| | | 30Dor-13 |
| 30Dor MMS 5 | $(3.4 \pm 1.6) \times 10^2$ | 30Dor-15 |
| 30Dor MMS 6 | $(5.0 \pm 2.1) \times 10$ | 30Dor-17 |
| 30Dor MMS 7 | $(1.8 \pm 0.8) \times 10^2$ | |
| 30Dor MMS 8 | $(3.1 \pm 1.3) \times 10^2$ | 30Dor-22 |
| 30Dor MMS 9 | $(3.1 \pm 0.6) \times 10^2$ | |
| 30Dor MMS 10 | $(7.9 \pm 1.6) \times 10^2$ | 30Dor-27 |
| | | 30Dor-28 |
| N158 MMS 1 | $(2.9 \pm 1.3) \times 10^2$ | N158-1 |
| N158 MMS 2 | $(2.4 \pm 1.1) \times 10^2$ | N158-3 |
| N158 MMS 3 | $(5.8 \pm 2.7) \times 10^2$ | N158-2 |
| N159 MMS 1 | $(1.0 \pm 0.7) \times 10^3$ | N 159E |
| N159 MMS 2 | $(3.3 \pm 2.2) \times 10^2$ | N 159W |
| N159 MMS 3 | $(3.5 \pm 2.4) \times 10^2$ | N 159W |
| N159 MMS 4 | $(1.1 \pm 0.7) \times 10^2$ | N 159-2 |
| N160 MMS 1 | $(6.7 \pm 4.7) \times 10^2$ | N 160-1 |
| | | N 160-2 |
| | | N 160-3 |
| N160 MMS 2 | $(6.3 \pm 4.4) \times 10^2$ | N 160-4 |
| | | N 160-5 |
| N160 MMS 3 | $(1.3 \pm 0.7) \times 10^2$ | |
| N160 MMS 4 | $(9.0 \pm 4.7) \times 10$ | |
| N44 MMS 1 | $(9.2 \pm 1.8) \times 10^2$ | |
| N44 MMS 2 | $(8.8 \pm 4.0) \times 10^2$ | 52 |
| N44 MMS 3 | $(6.2 \pm 2.8) \times 10^2$ | 52 |
| N44 MMS 4 | $(5.8 \pm 1.2) \times 10^2$ | |
| N44 MMS 5 | $(3.7 \pm 0.7) \times 10^2$ | |
| N44 MMS 6 | $(5.3 \pm 2.8) \times 10^2$ | 54 |
| N44 MMS 7 | $(5.0 \pm 2.6) \times 10$ | |
| N113 MMS 1 | $(1.4 \pm 0.3) \times 10^3$ | 38 |
| N113 MMS 2 | $(2.0 \pm 0.5) \times 10^2$ | |
| N113 MMS 3 | $(7.0 \pm 1.7) \times 10$ | |
| N214 MMS 1 | $(5.0 \pm 2.4) \times 10$ | 84 |
| N214 MMS 2 | $(3.9 \pm 1.8) \times 10^2$ | |

N 158C: (N 158 MMS 1 - 3) - Fig. 3.7

$$M_d = (1.1 \pm 0.5) \times 10^3 M_\odot \quad \text{N 158 MMS 3: 50\%}$$

N 159: (N 159 MMS 1 - 4) - Fig. 3.9

$$M_d = (1.8 \pm 1.2) \times 10^3 M_\odot \quad \text{N 159 MMS 1: 55\%}$$

N 160: (N 160 MMS 1 - 2, N 160 MMS 3 - 4) - Fig. 3.9

$$M_d = (1.3 \pm 0.9) \times 10^3 M_\odot, M_d = (2.2 \pm 1.1) \times 10^2 M_\odot$$

N 44: (N 44 MMS 1 - 7) - Fig. 3.12

$$M_d = (4.0 \pm 1.4) \times 10^3 M_\odot$$

N 113: (N 113 MMS 1 - 3) - Fig. 3.14

$$M_d = (1.7 \pm 0.4) \times 10^3 M_\odot \quad \text{N 113 MMS 1: 80\%}$$

N 214: (N 214 MMS 1 - 2) - Fig. 3.16

$$M_d = (4.4 \pm 2.1) \times 10^2 M_\odot \quad \text{N 214 MMS 2: 90\%}$$

The mass of the derived cool dust in the LMC is $(2.0 \pm 0.9) \times 10^4 M_\odot$. Nearly 69% is located in the 30 Dor complex, while other 20% belong to the N 44 region.

The mass distribution of the sources in the N 44 area is another evidence for the blowout structure of this luminous HII complex. The phenomenon of fragmentation is clearly observed in several dust regions such as N 113 and N 214 where the more massive cloud of each area, respectively, N 113 MMS 1 and N 214 MMS 2, predominates with 80-90% of the total mass of each region.

The amount of the cool dust in the LMC as estimated by Schwering (1988) from the IRAS 100 μm data and assuming a temperature of 15 K was $(1.0 \pm 0.5) \times 10^5 M_\odot$. Dall'Oglio et al. (1992) observed the LMC with a large beam ($\sim 1^\circ$ FWHM) at 1 mm and estimated with the use of the dust models of Draine & Lee (1984) and Mathis & Whiffen (1989) the amount of dust for the LMC to be, respectively: $(1.0 \pm 0.3) \times 10^7 M_\odot$ and $(9.1 \pm 2.8) \times 10^5 M_\odot$. In the present work, the dust masses derived for the prominent 30 Dor region and the other areas are due to the dense, compact clouds; as a result of the fast-scanning mapping technique with SIMBA the more diffuse component is most likely not detected. Nevertheless, comparing the mass of $(2.0 \pm 0.9) \times 10^4 M_\odot$ derived in the present thesis, the estimate with the Draine & Lee model which is a factor 10^3 higher seems not very realistic.

Chapter 4

Dust Observations in the SMC

4.1 Observed Regions in the SMC

Several regions of the SMC were selected as part of the 1.2 mm continuum emission studies and the observations were made with SIMBA during June, August, September and October 2002. The selection was based on the positions obtained from the IR survey of Schwering & Israel (1990) and also from the CO study of Israel et al. (1993).

Columns 2 and 3 of Table 4.1 list the positions for the epoch 2000.0 of the four regions where detections were surely made: N 12, H 15, N 27 and N 88. Column 4 presents major and minor axes (pc), while Column 5 lists the area (pc²). Columns 6 and 7 display, respectively, the measured peak (mJy/beam) and the integrated flux densities (mJy) at 1.2 mm.

Table 4.1: Axes, area, peak and integrated flux densities of the N 12, H 15, N 27 and N 88 sources, measured from the (sub)millimeter maps. The peak flux density is defined as the maximum value at the given position.

| Source | α_{2000} [h m s] | δ_{2000} [° ' "] | axes ^{a)} [pc] | area ^{b)} [pc ²] | S_{peak} ^{c)} [mJy/beam] | S_{int} ^{d)} [mJy] |
|-----------|----------------------------|----------------------------|----------------------------|--|---|---|
| N12 MMS 1 | 00:46:34.8 | -73:05:32 | 18 x 7 | 41 | 24 ± 4 | 30 ± 5 |
| N12 MMS 2 | 00:46:39.2 | -73:06:08 | 23 x 18 | 323 | 48 ± 7 | 200 ± 34 |
| H15 MMS 1 | 00:48:06.6 | -73:22:56 | 27 x 8 | 115 | 35 ± 5 | 85 ± 15 |
| N27 MMS 1 | 00:48:13.8 | -73:05:06 | 12 x 10 | 84 | 28 ± 4 | 50 ± 9 |
| N27 MMS 2 | 00:48:21.1 | -73:05:36 | 27 x 13 | 270 | 56 ± 8 | 220 ± 38 |
| N27 MMS 3 | 00:48:26.8 | -73:06:03 | 42 x 28 | 472 | 63 ± 9 | 300 ± 52 |
| N88 MMS 1 | 01:24:06.7 | -73:09:03 | 25 x 17 | 212 | 77 ± 12 | 140 ± 24 |

a) Both axes were obtained considering the signal starting at 3σ .

b) In general, the sources have an irregular shape.

c) The uncertainty of S_{peak} comes from the errors in the conversion factors and in the rms (Chapter 2).

d) For the errors of S_{int} see in Chapter 2 the uncertainties of the conversion factors (calibration) and of the MOPSI (reduction and analysis).

Also in this chapter a description of the different regions studied in the SMC as well as the results of the seven detected sources are presented.

4.1.1 N 12

N 12 (Henize 1956), also known as DEM S 23 (Davies, Elliott & Meaburn 1976), is an intense but small HII region, located in the SW part of the Bar of the SMC. It lies toward the dark nebula H 10 (Hodge 1974) and is associated with LI-SMC 36 (Schwering & Israel 1990).

The SW part of the Bar is the region where most of the detections of CO emission were made in the SMC and one of the brightest is the CO cloud (Israel et al. 1993) associated with LI-SMC 36. Rubio et al. (1993) mapped the region of the far-infrared source LIRS 36 with the SEST for ^{12}CO in the $J = 1 \rightarrow 0$ (radius of about 19 pc) and $J = 2 \rightarrow 1$ transitions. The LSR radial velocity of the CO (126.3 km/s) agrees with that of the associated HII region DEM S 23 (123.4 km/s). Further CO observations for LIRS 36 performed with the SEST are presented by Rubio et al. (1996) (together with that for the regions H 15, LIRS 49, N 66 and N 88). Chin et al. (1998) detected other molecules (CS, SO, C_2H , HCO^+ , HCN, HNC, H_2CO , C_3H_2) in this star-forming region.

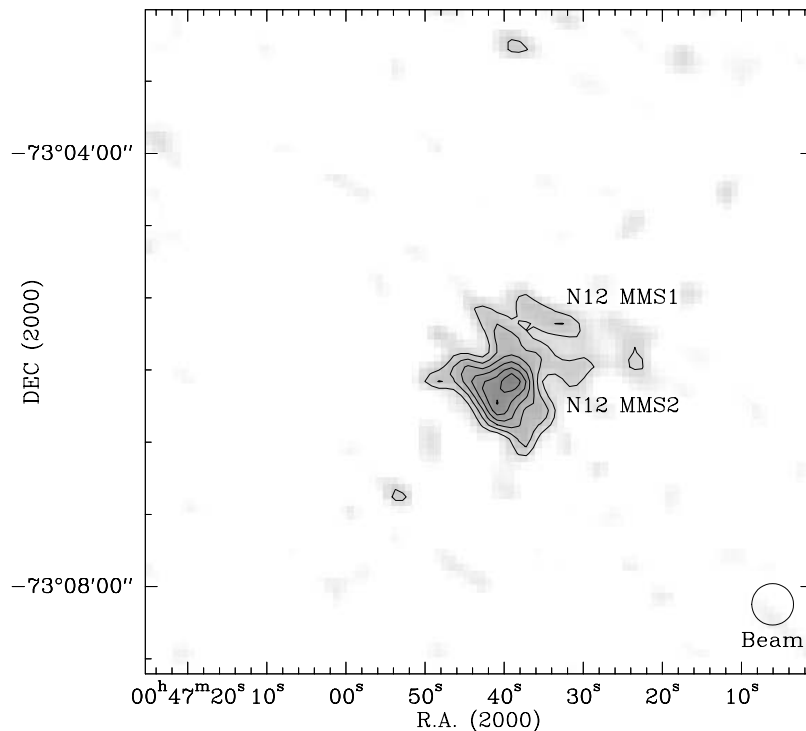


Figure 4.1: The N 12 area in 1.2 mm continuum obtained with a resolution of about $23''$ (HPBW). Contours are 18 mJy/beam (3σ) to 48 mJy/beam in steps of 6 mJy/beam.

Fig. 4.1 shows the 1.2 mm continuum emission map of the N 12 HII region with the contours starting at 3σ (rms of 6 mJy/beam). It has been created from 45 single maps during a total integration time of about 15.5 hours. The contour map shows two clouds here called N 12 MMS 1 - 2.

The detected CO emission and the IR detection are positional closely associated with the detections presented in Fig. 4.1.

4.1.2 H 15

The OB association H 15 (Hodge 1985) is located in the SW part of the SMC Bar and has seven stars brighter than $V = 14.2$.

Fig. 4.2 shows the 1.2 mm continuum emission map of the H 15 region with the contour starting at 3σ . The final map, rms of 7 mJy/beam, has been created from 26 single maps during a total integration time of about 10 hours. It shows a well-defined cloud here called H 15 MMS 1.

Israel et al. (1993) detected $^{12}\text{CO}(1-0)$ emission to the south of the SIMBA emission contour, at the position of the IR detection LI-SMC 44 (Schwering & Israel 1990). This region was also mapped by SIMBA, but yielded no detection.

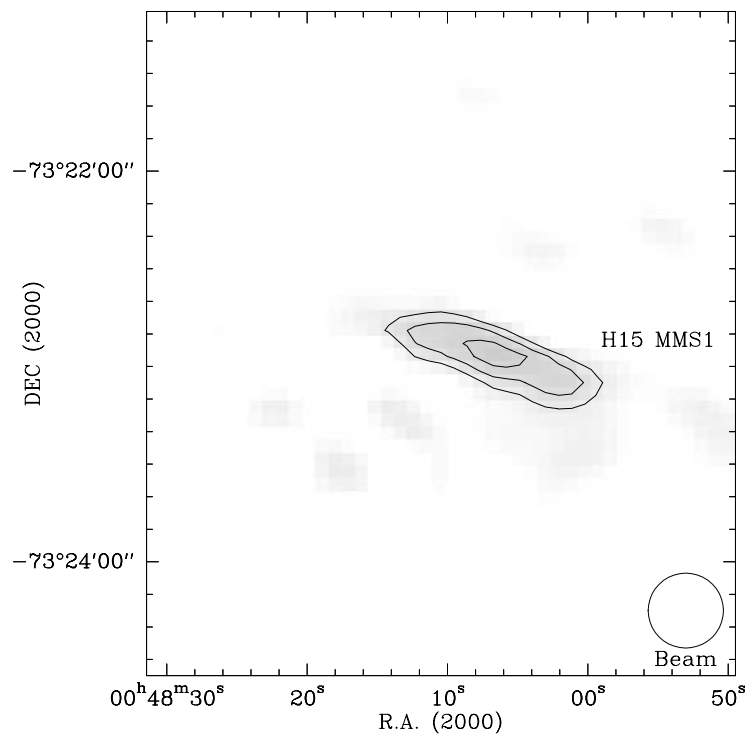


Figure 4.2: The H 15 area in 1.2 mm continuum obtained with a resolution of about $23''$ (HPBW). Contours are 21 mJy/beam (3σ) to 35 mJy/beam in steps of 7 mJy/beam.

4.1.3 N 27

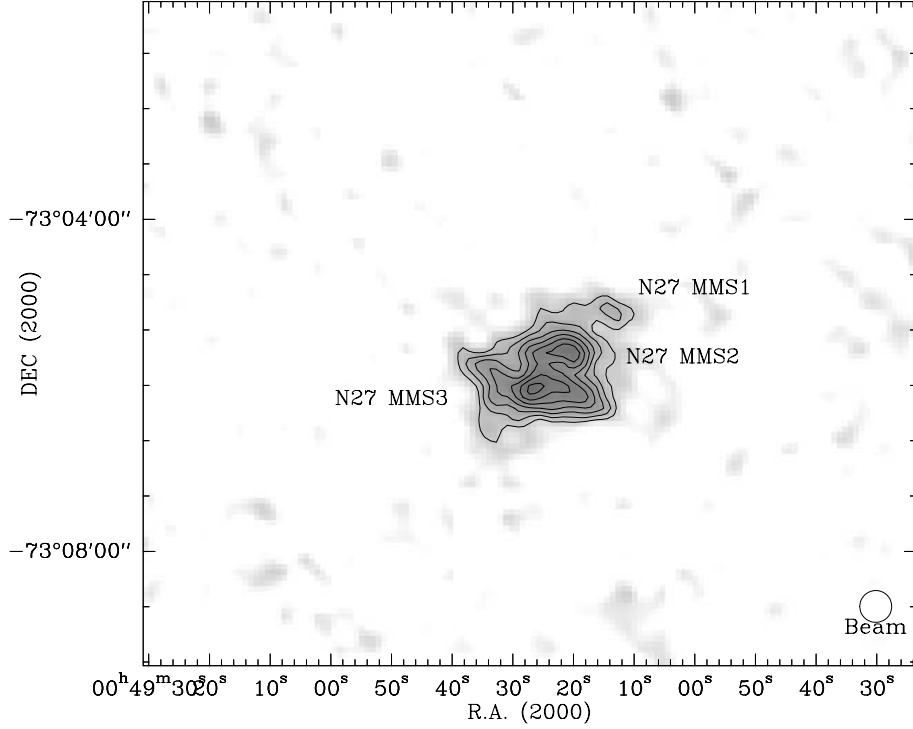


Figure 4.3: The N 27 area in 1.2 mm continuum obtained with a resolution of about $23''$ (HPBW). Contours are 21 mJy/beam (3σ) to 63 mJy/beam in steps of 7 mJy/beam.

The N 27 nebula was first cataloged by Henize (1956) and a later research by Davies, Elliott & Meaburn (1976) called it DEM S 40. N 27 is an intense and relatively compact HII region located in the south-western part of the SMC Bar and is associated with LI-SMC 49 (Schwering & Israel 1990).

In the SMC, the brightest CO cloud is associated with N 27 (Israel et al. 1993). Rubio et al. (1993) mapped the region of the far-infrared source LIRS 49 with the SEST for ^{12}CO in the $J = 1 \rightarrow 0$ (radius of about 17 pc) and $J = 2 \rightarrow 1$. No clearly absorption is seen towards the region in question. As pointed out by Rubio et al. (1993) the possible reason for this is that the CO cloud is behind the associated HII region.

The [CII] map of N 27 can resolve a source which is featureless and has low surface brightness extensions to the south and the west. The [CII] peak coincides with an IRAS detection (LI-SMC 49) and the CO source peaks about 10 pc west from it. A radio continuum source is close to the CO peak and has an extension coinciding with the [CII] peak. The situation described before is consistent with a molecular cloud complex in the process of being eroded by radiation from the exciting stars in N 27 (Westerlund 1997). Heikkilä, Johansson & Olofsson (1999) observed several molecules (e.g. CS, SO, HCO^+ , HCN, C_2H) in the N 27 cloud.

Fig. 4.3 displays the 1.2 mm continuum emission map of the N 27 HII region showing three clouds (N 27 MMS 1 - 3). This figure, with the contours starting at 3σ , was created from 31 single maps during a total integration time of about 11 hours and the rms of the final map was 7 mJy/beam.

Closely associated to the detections in Fig. 4.3 are the positions of the IR source LI-SMC 49 and of the observed CO emission.

4.1.4 N 66

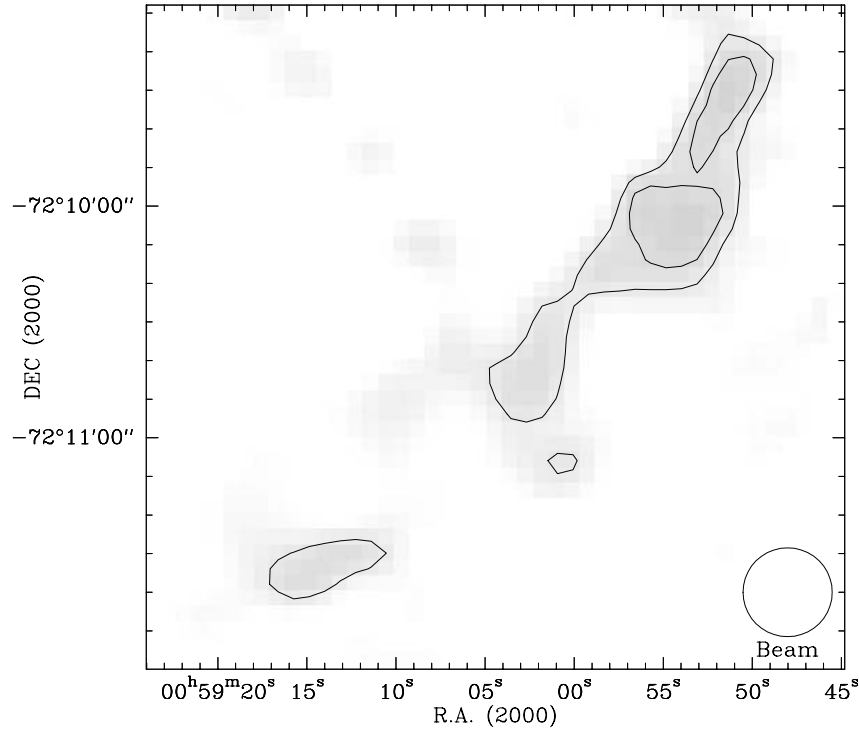


Figure 4.4: The N 66 area in 1.2 mm continuum obtained with a resolution of about $23''$ (HPBW). Contours are 21 mJy/beam (3σ) and 28 mJy/beam.

The largest and most luminous HII region in the galaxy in question is N 66 (Henize 1956), also known as DEM S 103 (Davies, Elliott & Meaburn 1976), NGC 346 (Gordon & Kron 1983) and H 45 (Hodge 1985). N 66 is located in the northern part of the SMC Bar and contains at least one known supernova remnant, SNR 0057-7226 (Danforth et al. 2003), which was confirmed by Ye, Turtle & Kennicutt (1991) through subtraction of the $H\alpha$ map from the 843 MHz radio map. In the N 66 complex Schwering & Israel (1990) detected in IR LI-SMC 131.

The NGC 346 cluster contains a large number of massive stars of spectral types as early as O2 (Naze et al. 2002). Massey, Parker & Garmany (1989) determined its stellar content as

~ 800 stars brighter than $V = 19$. On the outskirts of NGC 346 lies HD 5980 which is the main source of ionization in the nebula. HD 5980 is a OB?+WN eclipsing binary (Contursi et al. 2000).

High sensitivity maps of the $^{12}\text{CO}(2-1)$ line towards N 66 were presented by Rubio et al. (2000). The contour map of the integrated line emission resembles that of the SIMBA contour map (Fig. 4.4) with the former having a much higher signal-to-noise ratio. However, the $^{12}\text{CO}(2-1)$ line observations made with the SEST showed that N 66 does not contain much molecular gas in the region mapped with SIMBA. Rubio et al. (2000) suggest that most of the CO has been photodissociated and only small molecular clumps remain. NIR observations centered at $2.12 \mu\text{m}$ revealed H_2 . They discovered through J, H and K images of the molecular cloud several embedded stars and suggested that at least three different stellar generations are present in N 66 within only some 3×10^6 years.

Fig. 4.4 shows the 1.2 mm continuum emission map of the N 66, with the contours starting at 3σ . The final map has been created from 26 single maps during a total integration time of about 7.5 hours (the 1σ rms is about 7 mJy/beam).

The contour map shows several probable detections, two of them have a measured peak flux of 4σ . The most southern signal is even smaller than the SIMBA beam. Therefore, it can be concluded that this one is a scanning effect. The origin of the others can have the same explanation. As about 60% of the single maps were taken at $120''/\text{s}$ scan speed instead of $80''/\text{s}$ (the latter one was used for all the LMC regions and for all the regions of the SMC, with the exception of all single maps of N 76 and some of N 88), this can have contributed to decrease the quality of the final map. Using $120''/\text{s}$ instead of $80''/\text{s}$ has the advantage that more maps can be done in the same interval of time. However, the quality of the individual maps is best at $80''/\text{s}$. Therefore, in general only maps with this scan speed has been carried out.

To have a more conclusive idea of the (sub)millimeter continuum features of N 66, more integration of this area is needed.

4.1.5 N 76

The N 76 (Henize 1956) nebula, also called DEM S 119 (Davies, Elliott & Meaburn 1976), NGC 371 (Gordon & Kron 1983) and H 53 (Hodge 1985), is located in the northern part of the SMC Bar and was observed by Schwering & Israel (1990) in IR (detection LI-SMC 161).

The 1.2 mm continuum emission map of the N 76 region with the contour starting at 3σ is shown in Fig. 4.5. It has been created from 20 single maps during a total integration time of about 5.5 hours and the 1σ rms is about 8 mJy/beam.

The contour map shows a probable detection, which have a measured peak flux of 3σ . However, this SIMBA signal could be a scanning effect. As mentioned before, the scan speed of $120''/\text{s}$ can have contributed to decrease the quality of the final map.

A better idea of the features of N 76 needs more observations at the studied wavelength regime.

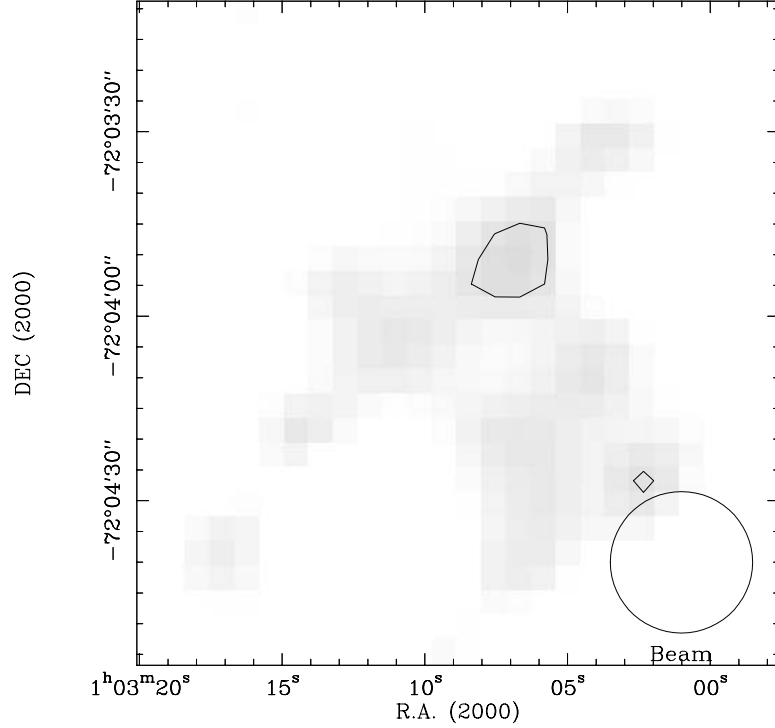


Figure 4.5: The N 76 area in 1.2 mm continuum obtained with a resolution of about $23''$ (HPBW). Contour is 24 mJy/beam (3σ).

4.1.6 N 81

The N 81 (Henize 1956) nebula, also called DEM S 138 (Davies, Elliott & Meaburn 1976) and H 60 (Hodge 1985), is located in the Shapley Wing, SE of the main bar, ~ 1.2 kpc from the main body of the SMC (Heydari-Malayeri et al. 1999a). The IR survey of Schwering & Israel (1990) detected LI-SMC 187 in this nebula.

The search for very young, emerging HII regions in the MCs, yielded the discovery of a very rare class of HII regions called high-excitation compact HII blobs (HEBs). In the SMC two were discovered, N 81 and N 88A. In contrast to the typical HII regions which are extended structures (more than 50 pc powered by a large number of stars), they are very dense and small ($\sim 1.5 - 3$ pc). In general HEBs are heavily affected by local dust. In contrast to other MCs HEBs (e.g. LMC 159-5, N 160A1, N 160A2, SMC N 88A) N 81 does not lie adjacent or in the direction of a typical giant HII region, but is isolated. The star formation in N 81 is a local event there, being powered by a small group of newborn massive stars (Heydari-Malayeri et al. 1999a). Martins, Schaerer & Heydari-Malayeri (2003) performed far-UV spectra and revealed that N 81 stars are of O6-O8 type.

Fig. 4.6 shows the 1.2 mm continuum emission map of the N 81 nebula with the contours starting at 3σ . The final map has been created from 25 single maps during a total integration

time of about 10.5 hours (the 1σ rms is about 9 mJy/beam). The contour map shows four probable detections, one of them has a measured peak flux of 4σ . The two more north displayed signals are even smaller than the SIMBA beam. Therefore, it can be concluded that probably both are scanning effects. The origin of the others can have the same explanation.

Israel & Koorneef (1988), Heydari-Malayeri et al. (1999a) and Heydari-Malayeri et al. (2003) found through, respectively, $\text{Br}\gamma/\text{H}\beta$, $\text{Br}\alpha/\text{H}\beta$ ratios and $\text{H}\alpha/\text{H}\beta$ Balmer decrement and H - K color index of the stars in the field (does not display correlation with the projected distance of N 81) a low extinction towards this HII region.

The central SIMBA peak (IR: LI-SMC 187) coincides practically with $^{12}\text{CO}(1-0)$ emission (Israel et al. 1993). Among all the regions detected in their survey and included in this study, this one was the weakest.

The fact that no important molecular cloud has been detected together with the low extinction are arguments against the presence of important dust concentration towards N 81.

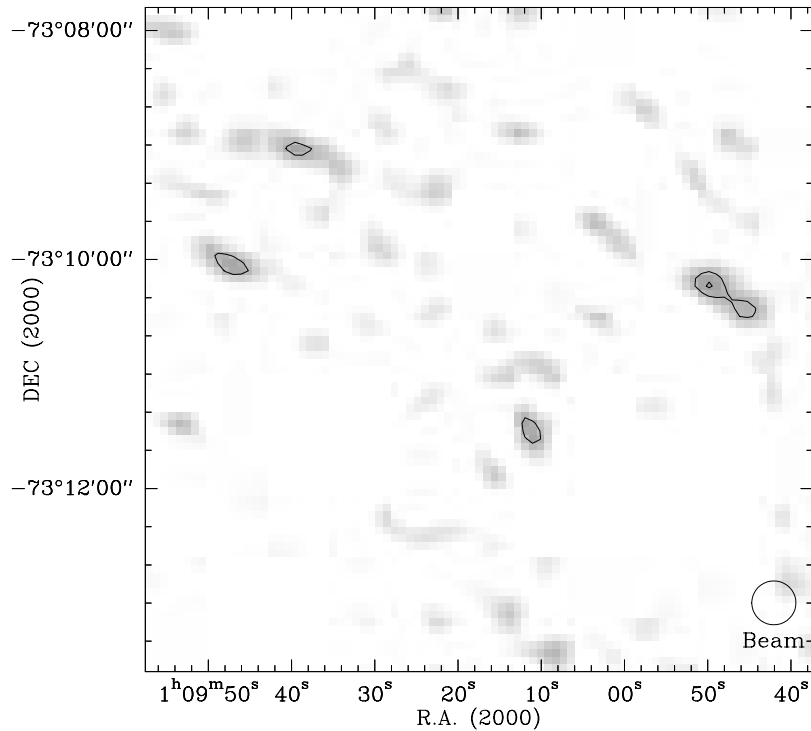


Figure 4.6: The N 81 area in 1.2 mm continuum obtained with a resolution of about $23''$ (HPBW). Contours are 27 mJy/beam (3σ) and 36 mJy/beam.

4.1.7 N 83 - 84

The region N 83-84-85 (Henize 1956) is a complex, also located in the Shapley Wing, rich in young stellar clusters and nebulae of different sizes. These objects are probably all related.

It appears that the region of about 500 pc is undergoing a sequential star formation, on a scale of 10^7 yr (Testor & Lortet 1987). The youngest parts of the complex are N 83 and N 84. They are associated, respectively, to NGC 456, H 61 and NGC 460 (Gordon & Kron 1983), H 62 (Hodge 1985). They also are called DEM S 147 and 151 (Davies, Elliott & Meaburn 1976) where unevolved O stars (O6-8V) were discovered through BV photometry by Testor & Lortet (1987). The ionized gas in the N 83-84 region has a high degree of fragmentation.

Fig. 4.7, created from 28 single maps during a total integration time of about 10 hours, shows the 1.2 mm continuum emission map of the N 83-84 emission nebulae with the contours starting at 3σ (the 1σ rms is about 8 mJy/beam). The contour map shows several probable detections, some of them have a measured peak flux of 4σ , but they are practically all smaller than the SIMBA beam. Therefore these signals can be caused by scanning effects.

In order to have a more conclusive idea of the (sub)millimeter continuum features of this area, more integration of it is needed.

Schwering & Israel (1990) observed the N 83-84 complex in IR and revealed the detections LI-SMC 199 and 202. The last one, located SE of the region shown in Fig. 4.7, presents $^{12}\text{CO}(1-0)$ emission (Israel et al. 1993). This region was also mapped with SIMBA, but no detection was observed.

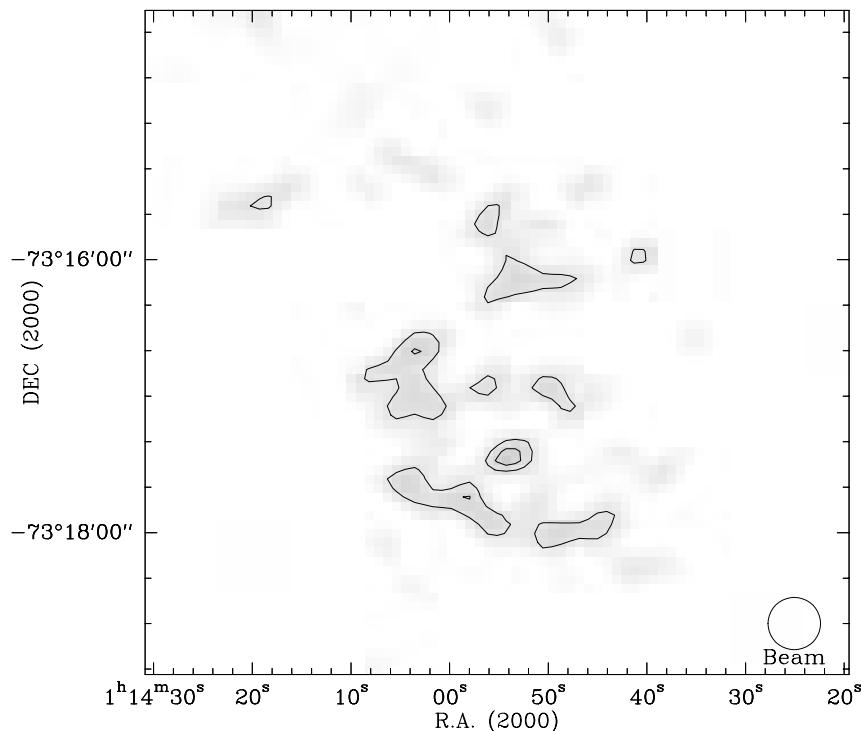


Figure 4.7: The N 83-84 area in 1.2 mm continuum obtained with a resolution of about $23''$ (HPBW). Contours are 24 mJy/beam (3σ) and 32 mJy/beam.

4.1.8 N 88

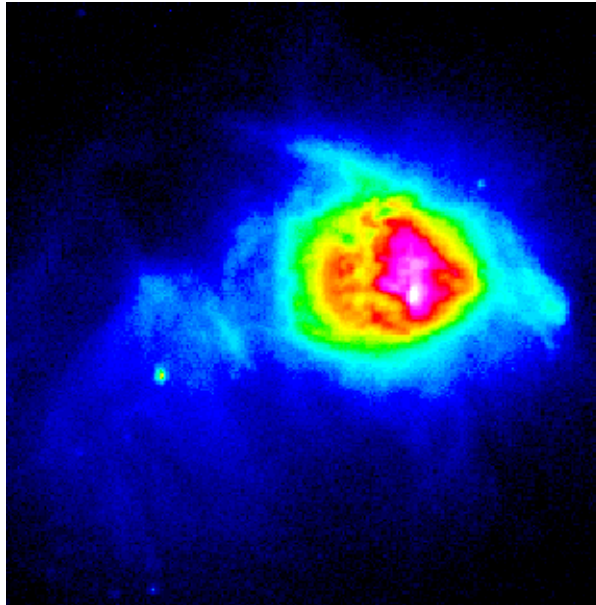


Figure 4.8: $H\alpha$ image from the HII blob N 88A - diameter about 1 pc - taken with HST (Heydari-Malayeri homepage).

The HII region N 88 (Henize 1956), also called DEM S 161 (Davies, Elliott & Meaburn 1976) and H 64 (Hodge 1985), is located further out the Shapley Wing and on the west side of the only supergiant shell in the SMC, SGS SMC 1 (Meaburn 1980). In IR (Schwering & Israel 1990) LI-SMC 215 was detected. This region covered by the SIMBA observations coincides with the star clusters HW 80, HW 81, HW 82 (Hodge & Wright 1974) and L 101 (Lindsay 1958). They are all constituted mainly by blue stars (Testor & Pakuli 1985). The second and the last one are closely associated to the object shown in Fig. 4.9.

N 88 is a nebula with a very bright compact core surrounded by diffuse nebulosity. HeII absorption lines indicate that the central object, the blob N 88A is ionized by a star earlier than O5V (Testor, Rola & Whiting 1999). Israel & Koorneef (1988) observed H_2 emission in the direction of N 88. Caplan et al. (1996) observed an integrated $H\alpha/H\beta$ ratio of 3.75 for N 88, the ratio reaches six in the core and drops rapidly in the surroundings. They concluded that a ratio significantly higher than 2.8 is evidence for reddening by dust. N 88 is one of the most reddened objects from a sample of 24 bright HII regions in the SMC. The UV attenuation law for N 88A increases slowly over 3000-1500 Å, as compared to the general SMC reddening which has a steep rise. This is interpreted by Kurt et al. (1999) as evidence for the destruction of small grains in and around the nebula.

N 88A (Fig. 4.8) is probably younger than N 81 as N 81 is more extended, less dense and exhibits several of its exciting stars through the Wide Field Planetary Camera 2 (WFPC2) on board of the HST (Heydari-Malayeri et al. 1999b).

Fig. 4.9 shows the 1.2 mm continuum emission map of the N 88 emission nebula with the contour starting at 3σ (rms of 7 mJy/beam). It has been created from 25 single maps during

a total integration time of about 11.5 hours. The contour map shows a well-defined cloud here called N 88 MMS 1.

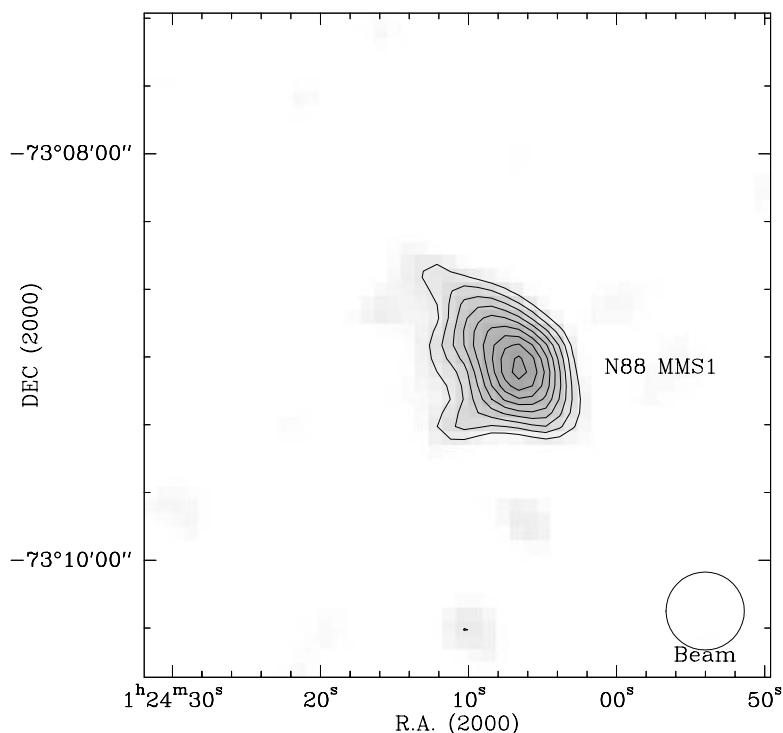


Figure 4.9: The N 88 area in 1.2 mm continuum obtained with a resolution of about $23''$ (HPBW). Contours are 21 mJy/beam (3σ) to 77 mJy/beam in steps of 7 mJy/beam.

$^{12}\text{CO}(1-0)$ emission (Israel et al. 1993) is located practically at the position of the SIMBA emission peak, which is also the position of LI-SMC 215.

The fact that N 88A is probably younger than N 81 as well as that Israel et al. (1993) detected more CO towards N 88 than towards N 81 is in agreement with the detection of cold dust in the former and the non-detection in the latter.

4.2 Results

4.2.1 Temperatures

As mentioned before, the emission observed at 1.2 mm might be not entirely due to thermal emission.

In order to estimate the CO contribution, the intensity ratio I_{2-1}/I_{1-0} found by Lequeux et al. (1994) accurate to 20% for the different regions is used. In all four star formation regions where SIMBA detections were surely observed, the contamination by the CO in the $J = 2$

- 1 transition is found to be negligible (for N 12, H 15, N 27 and N 88 the intensity ratio I_{2-1}/I_{1-0} is 1.1, 1.2, 1.3 and 1.0, respectively, giving 4, 1, 7 and 1 mJy as corresponding contamination).

From the corresponding radio continuum measurements at 2.45 GHz, 4.75 GHz and 8.55 GHz (Haynes et al. 1991) the synchrotron emission contribution and/or the free-free emission contribution to the measured 1.2 mm flux of the different sources could be estimated. The HPBW of the 2.45, 4.75 and 8.55 GHz data are $8.9'$, $4.4'$ and $2.8'$, respectively. The mean value of about -0.1 was confirmed in the spectrum. The extrapolation to the (sub)millimeter wavelength regime was performed with $S_\nu \propto \nu^{-0.1}$ (only free-free emission) as the synchrotron radiation revealed to be negligible.

Fig. 4.10 shows the SED of the individual or combined dust sources per region obtained fitting 1.2 mm data (see Column 3 in Table 4.2) with the IRAS $100 \mu\text{m}$ images (see Table 4.3). It also presents the complementary data from IRAS 12, 25 and $60 \mu\text{m}$ (the procedure used to get an estimate for the dust temperature is explained in Chapter 1).

Table 4.2: Contamination and corrected dust fluxes for regions in the SMC.

| Region | S_{ff} [mJy] | S_{dust} [mJy] |
|----------------|-----------------------|-------------------------|
| N 12 MMS 1 - 2 | 20 ± 4 | 210 ± 40 |
| H 15 MMS 1 | - | 85 ± 15 |
| N 27 MMS 1 - 3 | 65 ± 13 | 505 ± 99 |
| N 88 MMS 1 | - | 140 ± 24 |

Table 4.3: IRAS fluxes of regions in the SMC.

| Region | S_{IRAS} [Jy] | | | |
|----------------|------------------------|------------------|------------------|-------------------|
| | $12 \mu\text{m}$ | $25 \mu\text{m}$ | $60 \mu\text{m}$ | $100 \mu\text{m}$ |
| N 12 MMS 1 - 2 | 0.5 ± 0.1 | 0.9 ± 0.1 | 1.0 ± 0.2 | 10.1 ± 1.5 |
| H 15 MMS 1 | 0.6 ± 0.1 | 1.0 ± 0.2 | 9.8 ± 1.5 | 14.6 ± 2.2 |
| N 27 MMS 1 - 3 | 1.1 ± 0.2 | 1.8 ± 0.3 | 28.5 ± 4.3 | 39.7 ± 6.0 |
| N 88 MMS 1 | 1.1 ± 0.2 | 1.7 ± 0.3 | 5.4 ± 0.8 | 7.9 ± 1.2 |

Considering also the observational errors in the SMC of 14% for SIMBA's calibration, about 10% for MOPSI, 20% for the radio data and 15% for IRAS, the derived dust temperatures for the different regions are:

- N 12: 17 ± 1 K
- H 15: 20 ± 2 K
- N 27: 18 ± 1 K
- N 88: 17 ± 1 K

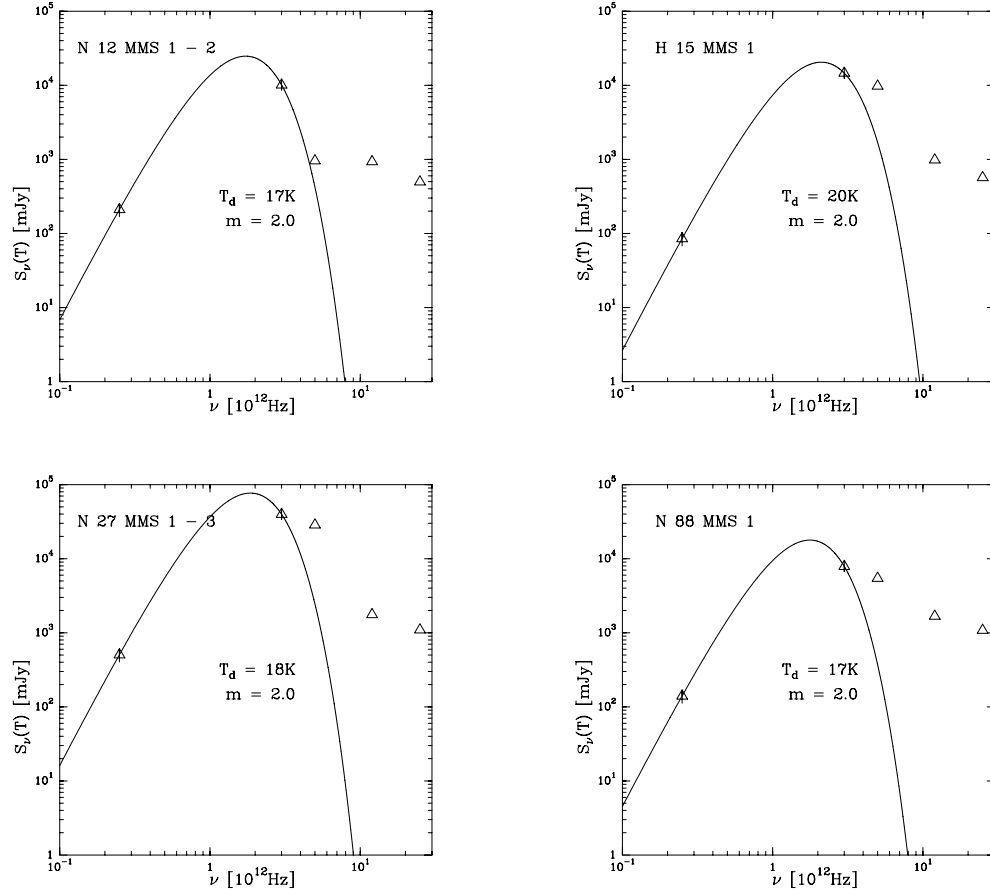


Figure 4.10: SED of the sources detected with SIMBA in N 12, H 15, N 27 and N 88.

Wilke et al. (2003) analyzed the ISOPHOT map of the SMC at $170 \mu\text{m}$ and obtained an average dust temperature of 20.5 K for this galaxy from the $170/100 \mu\text{m}$ ratio. Their ISO $170 \mu\text{m}$ source catalog contains a total number of 243 sources, with the number 10 being associated with N 12, 18 with H 15, 15 and 20 with N 27 and the source labelled 232 with N 88.

Stanimirovic (1999) using the $100/60 \mu\text{m}$ ratio derived for the SMC dust temperatures varying from 31 to 45 K for HII regions.

As in this work the $1.2 \text{ mm}/100 \mu\text{m}$ ratio is being used, it can be expected that here the derived temperatures will be lower than the ones obtained in the two previously cited studies.

Schlegel, Finkbeiner & Davis (1998) $100 \mu\text{m}$ map of the Galaxy shows the dust temperature varying from 17 to 21 K. Therefore, considering that the ISRF of the SMC is 10 times stronger than that of the Solar Neighborhood, it is unlikely that dust colder than 17 K contributes to the IRAS $100 \mu\text{m}$ flux in the SMC.

Schwering (1988) found from the $100/60 \mu\text{m}$ ratio in SMC HII regions dust temperatures ranging from 34 to 43 K. The prominent HII regions in his IR data (N 66, N 76, N 83-84) do not show SIMBA detections. In this sites the strong UV radiation from the OB stars

heats the dust grains to higher temperatures erasing a SIMBA dust contribution. The lower metallicity of the SMC leads to a smaller dust amount, which decreases the self-shielding allowing that the UV radiation penetrates deeper in the star forming regions. In the other regions (see derived temperatures in the present work) a cool dust phase exists associated with the molecular cloud. Two types of HII regions could so be verified in this study (one with and another without a cool dust phase) in the SMC. Also the existence of dust colder than 20 K is confirmed in this galaxy.

The dust temperatures of the HII regions vary from the absence of a cool phase in the northern part of the SMC Bar (N 66, N 76) and in the Shapley Wing (N 81, N 83-84), with the exception of N 88, to the presence of it in the SW part of the Bar (N 12, H 15, N 27). There it is identified a regime of T_d going from 17 to 20 K. N 12, N 27 and N 88 have very similar temperatures.

4.2.2 Masses

The results for the dust masses of N 12, N 27, H 15 and N 88 are shown in Table 4.4 (the procedure used to get an estimate for the dust mass is explained in Chapter 1). The uncertainties in the mass are around 20%. These uncertainties were derived like the ones for the LMC regions.

A total mass of $M_d = (3.2 \pm 0.7) \times 10^2 M_\odot$ is obtained for the entire N 12 region (Fig. 4.1). The dust masses from N 12 given in Table 4.4 are obtained assuming the average temperature of 17 K to hold for all individual sources. So the strongest source - N 12 MMS 2 - has about 85% of the mass.

For the entire N 27 region (Fig. 4.3) a total mass of $M_d = (6.7 \pm 1.5) \times 10^2 M_\odot$ is obtained. Assuming that the average temperature of 18 K holds for all individual sources the dust masses from N 27 given in Table 4.4 are obtained. The result means that the strongest source - N 27 MMS 3 - has about 50% of the total mass.

Table 4.4: Total dust masses of the dust clouds. The CO cloud numbers are taken from Israel et al. (1993).

| Source | $M_d [M_\odot]$ | CO cloud |
|------------|-----------------------------|----------|
| N 12 MMS 1 | $(4.2 \pm 0.9) \times 10$ | 8 |
| N 12 MMS 2 | $(2.8 \pm 0.6) \times 10^2$ | 8 |
| H 15 MMS 1 | $(1.0 \pm 0.2) \times 10^2$ | 15 |
| N 27 MMS 1 | $(5.9 \pm 1.3) \times 10$ | 20 |
| N 27 MMS 2 | $(2.6 \pm 0.6) \times 10^2$ | 20 |
| N 27 MMS 3 | $(3.5 \pm 0.8) \times 10^2$ | 20 |
| N 88 MMS 1 | $(2.1 \pm 0.4) \times 10^2$ | 41 |

The total mass of the derived cool dust is $(1.3 \pm 0.3) \times 10^3 M_\odot$. Nearly 84% of it is located in the SW Bar. The other 16% are located in N 88, which is a further evidence that this

HII region is the most recent site of star formation in the Shapley Wing, in agreement with Heydari-Malayeri et al. (1999b). N 88 is the SMC source with the highest cool dust concentration in the center (it has the HEB N 88A as central object).

Schwering (1988) obtained for the SW Bar area and the Shapley Wing region $6.4 \times 10^3 M_{\odot}$ and $1.0 \times 10^3 M_{\odot}$, respectively ($T_d \simeq 34$ K). This means that the SW Bar has more dust than the Wing in both phases (cool and warm). Assuming a temperature of 15 K, Schwering (1988) estimated the amount of cool dust from the $100 \mu\text{m}$ data and derived a value of $(0.8 \pm 0.4) \times 10^4 M_{\odot}$. Likewise, Stanimirovic (1999) obtained $2.4 \times 10^4 M_{\odot}$ using $240 \mu\text{m}$ data. The cool dust is associated with the molecular gas phase and in the SMC the latter one exists only in dense parts of the interstellar clouds. The mass estimate from the present survey, which covers eight regions (Table 2.1) from 27 of the Israel et al. (1993) CO detections in the SMC, including the most important star formation sites in this galaxy, agrees with the former estimates.

Chapter 5

Gas-to-dust Ratio R in the LMC and the SMC

In Chapter 1 the differences between the Milky Way, the LMC and the SMC were already commented (e.g. metallicity and radiation field). It was soon clear that in the MCs, especially in the SMC, CO emission is weaker than in the Milky Way. This is due to the low metallicity and the CO photodissociation. The latter is a result of the strong radiation field. In the MCs, contrary to the Galaxy, CO molecules can only survive in dense parts of interstellar clouds at densities that depend on the radiation field, while they are photodissociated in the less dense medium. The weakness of CO does not imply small amounts of H₂ as molecular hydrogen is not seriously affected by photodissociation (Israel & de Graauw 1991). However, it has even been claimed that irregular galaxies contain negligible amounts of molecular gas, they have giant HII regions and OB associations which presence show episodes of recent star formation.

The first detection of CO ($J = 1 - 0$) in the MCs was done by Huggins et al. (1975). Complete maps with low resolution were made by Cohen et al. (1988) for the LMC and by Rubio et al. (1991) for the SMC. In the meantime, the ESO-SEST Key Programme: *CO in the Magellanic Clouds* (e.g. Israel et al. 1993; Rubio et al. 1993; Rubio, Lequeux & Boulanger 1993; Lequeux et al. 1994; Rubio et al. 1996; Kutner et al. 1997) has presented observations of parts of the Magellanic Clouds with high spatial resolution. Observations in the ¹²CO (1 → 0) line in the LMC and in the SMC were reported by Israel et al. (1993) towards 92 and 42 IRAS sources, respectively.

The other observations of the CO emission in the LMC, made by using the SEST as part of the ESO-SEST Key Programme concentrated on the more remarkable areas cited next. The observations of the Key Programme fully mapped several regions in the ¹²CO (1 - 0) emission: 30 Dor central and southern complex (e.g. Johansson et al. 1998), N 11 (e.g. Israel et al. 2003), cloud 37 (e.g. Garay et al. 2002) identifying at least 90 molecular clouds. Because of the proximity of the LMC the SEST telescope with an angular resolution of 45'' and 23'' at the CO (1 → 0) and CO (2 → 1) frequencies provides, respectively, a linear resolution of 11 and 6 pc at the distance of this galaxy, which is well suited to resolve the largest molecular clouds. The LMC CO clouds have sizes between 10 and 40 pc, line widths ranging from 2.5 to 10 km/s, CO luminosities between 5×10^2 and 5×10^4 K km s⁻¹ pc² and virial masses

ranging from 10^3 to $7 \times 10^5 M_{\odot}$. These clouds are larger in size and more massive than the clouds found in the SMC, but do not look like typical GMCs in the Milky Way. Their properties are closer to molecular clouds in the outer Galaxy than in the inner one (Rubio 1997).

CO observations undertaken with NANTEN (lower resolution i.e. $2.6'$, which corresponds to ~ 30 pc linear resolution, and higher spatial coverage than the studies carried out with SEST) found the following statistics for massive CO clouds in the LMC:

- 22% of the CO clouds have no sign of star formation, i.e., they are not associated with HII regions or stellar clusters.
- 31% of the CO clouds are associated only with small HII regions.
- 47% of the CO clouds are associated with stellar clusters and large HII regions, thus suggesting an ongoing formation of massive clusters.

There are also several regions where stellar clusters coexist with large HII regions and have only a small amount of CO clouds associated.

Fukui et al. (1999) pointed out that the four above cited situations may represent the evolutionary sequence of the CO clouds. Most of the regions mapped with SIMBA in the LMC are included in the third class. The CO cloud N 159-S, as reported in Chapter 3, has no sign of dust. It is an example of the first class.

Observations done as part of the ESO-SEST Key Programme in the SMC focused in the study of the southwestern bar (e.g. Rubio et al. 1993) showing a variety of CO structures with a wide range of radii (10 to 200 pc). At the smallest scales (≈ 10 pc) which can be resolved the SMC structures are less luminous in CO than Galactic molecular structures of the same size, by a factor of about 1.5 while at large scales they are much less luminous by a factor of 10 - 20 (Rubio, Lequeux & Boulanger 1993).

The total mass of the molecular clouds in the LMC and the SMC is estimated to be $1.4 \times 10^8 M_{\odot}$ and $\sim 3 \times 10^7 M_{\odot}$, respectively (Westerlund 1997). From HI observations with an angular resolution of $1'$, Kim (1998) estimated that the mass of the LMC has an upper limit of $\sim 3.5 \times 10^9 M_{\odot}$ out to a radius of 4 kpc.

Several authors (e.g. Koornneef 1982, Pei 1992) remarked the differences in the dust-to-gas (HI) ratio between the Milky Way, the LMC and the SMC. The $N(\text{HI})/E(\text{B-V})$ ratio for the MCs has been investigated several times in the literature and a large spread in the gas-to-dust ratios has been found depending on the used measurements (Schwering 1988). Pei (1992) estimated the mean ratios as being respectively 1:0.2:0.1.

The dust-to-gas ratio measures the efficiency of the dust production. According to commonly used dust models the main ingredients are carbon and silicate, therefore a higher efficiency is expected for more metal-rich systems. Low C and O abundances, strong mean UV radiation fields and low dust-to-gas ratios are the hypothesis to explain the tendency of weaker CO emission in the Magellanic Clouds sources when compared to the galactic ones.

Stanimirovic (1999) suggested for the SMC a dust model constituted by:

- large silicate core particles mantled with amorphous carbon or graphite, with sizes $a > 0.05 \mu\text{m}$ which are known as "classical" grains
- very small carbonaceous grains (VSGs), with sizes $a < 0.005 \mu\text{m}$
- Polycyclic Aromatic Hydrocarbons (PAH's)

This model is based on several studies such as Mathis, Rumpl & Nordsieck (1977), Draine & Anderson (1985), Li & Greenberg (1997) and Rodrigues et al. (1997).

In Stanimirovic's (1999) model at $100 \mu\text{m}$ and 1.2 mm (the SEDs plotted in Chapters 3 and 4 are fitted with these wavelengths) the large grains dominate the emission spectra. They reach equilibrium with the ISRF being characterized by a single temperature. In small grains their low heat capacity produces temperature fluctuations with the changes becoming progressively larger for smaller grains. At $100 \mu\text{m}$ and 1.2 mm the smaller grains, which are transiently heated, make a negligible contribution to the emission. Therefore, the dust temperature is better estimated at these wavelengths.

Stanimirovic's (1999) observations of HI and the combination of these data with the IR data ($100/60 \mu\text{m}$ ratio map) enabled a comparison of dust and neutral gas in the whole SMC all the way down to 30 pc . The total dust mass and the total mass of HI within a $2^\circ \times 2^\circ$ area of the galaxy in question are, respectively, $1.8 \times 10^4 M_\odot$ and $2.2 \times 10^8 M_\odot$. The highest dust-to-gas ratios in the SMC she found in bright HII regions. A considerable spatial variation between the optical bar and the Eastern Wing was found. The maximum being that of N 88. Local differences in the dust-to-gas ratio were hypothetically attributed to local phenomena such as: i) atomic gas deficiency due to molecular hydrogen presence; ii) massive star formation regions signed by excessive dust; iii) cold dust not emitting at $100 \mu\text{m}$. She also interpreted that it is hard to believe that cold gas and/or dust might exist in such amount to allow an interpretation as a deficiency of HI ($\sim 8 \times 10^8 M_\odot$ of H_2 is required) or as a deficiency of cold dust ($\sim 10^6 M_\odot$ not seen by IRAS or COBE).

Vermeij et al. (2002) presented $3.3, 6.2, 7.7, 8.6$ and $11.2 \mu\text{m}$ spectra from a sample of HII regions in the LMC, including several positions in 30 Dor and one in N 159 (towards the molecular cloud N 159E). In all spectra emission bands arising from PAHs are present. Their observations point towards the molecular structure as the major cause of variations in the spectra. Compact PAHs dominate in the SMC and in 30 Dor, while PAHs with open, uneven structure are the dominant ones in Galactic HII regions and the non-30 Dor LMC sources.

In Chapters 3 and 4 the SEDs of the several regions (with the respectively derived dust temperatures) surveyed with SIMBA in the LMC and the SMC were plotted. In the same chapters the dust masses of the regions were estimated. The derived dust masses allow a comparison with the amount of gas. The observations of dust continuum emission and CO line offer the opportunity to directly compare both methods and thus to put constraints on the ratio of molecular gas-to-dust R .

In this chapter, the molecular gas-to-dust ratios R are derived by using the gas masses obtained from the literature and the dust masses derived in this work from the associated dust clouds.

5.1 Gas-to-dust Ratio R in the LMC

The virial mass formula

$$M_{\text{vir}} = 190 D \Delta v^2 \quad (5.1)$$

gives the virial cloud mass in units of M_{\odot} for a spherical cloud with a r^{-1} volume density profile, where D is the FWHM of the integrated emission when modelled with a circular Gaussian distribution [pc] and Δv is the FWHM of the observed line profile [km s^{-1}]. The value of the virial theorem coefficient is appropriate to the density distribution; in the case of $\rho(r) \propto r^{-1}$ it is 190 (MacLaren, Richardson & Wolfendale 1988).

However, the geometry of the detected SIMBA sources in the LMC displayed in Chapter 3, as well as that of the CO detections of Johansson et al. (1998) and Johansson (2002) molecular clouds in the corresponding regions, rise doubts if Eq. (5.1) should be applied to the sources.

Johansson et al. (1998) assumed an ellipsoidal shape for the molecular clouds. They modelled with axial ratios between 1 and 3 for low and high optical depths finding an average factor of 0.8 with a spread of 20%. Applying the factor to Eq. (5.1) it is obtained

$$M_{\text{vir}} = 150 D \Delta v^2. \quad (5.2)$$

The virial masses derived are given in Table 5.1. The uncertainties shown for M_{vir} reflect the fact that the line widths suffer from errors of 0.5 km s^{-1} . These are the largest line width errors which apply to weak signals and/or complex emission (all sources are included in one or the other case).

Along six lines of sight towards the LMC, as well as one towards the SMC, Richter (2000) presented H_2 observations obtained through FUV absorption. He investigated correlations between the HI and the H_2 column densities. From the results he pointed out that the fraction of gas in molecular form should be lower in the MCs than in the Galaxy. None of these lines of sight is in the regions studied in this work. Kahabka, de Boer & Brüns (2001) analyzed background X-ray sources in the LMC field and derived total hydrogen column densities. Then, they compared them with the neutral hydrogen column densities inferred from 21 cm line measurements. For two of their background sources (one of them, the quasar RX J0536.9-6913, being localized in the 30 Dor complex) they found hydrogen column densities due to LMC gas, which are in excess compared to the HI columns. They concluded from RX J0536.9-6913 (=MDM 65 of Marx, Dickey & Mebold 1997) located at 05:36:57.8 -69:13:26 (J2000) that the mass fraction of molecular gas in the 30 Dor complex is less than $\sim 70\%$. But, the coordinates from RX J0536.9-6913 localize it in none of the 30 Dor regions: A, B or C.

Assuming that the clouds' hydrogen content is only in molecular form the virial mass represents the total gas mass, i.e. $M_{\text{vir}} \sim M_{\text{H}_2} \sim M_{\text{g}}$. This allows the determination of the molecular gas-to-dust ratio R given through

$$R = \frac{M_{\text{g}}}{M_{\text{d}}}. \quad (5.3)$$

But, there are a number of assumptions about the determination of R which deserve a closer view:

- The virial mass formula to obtain the gas mass is used in this study as it is the preferable method (see Chapter 1). However, it is questioned by several authors (e.g. Maloney 1990). Maloney (1990) showed the correlation between CO luminosities and virial masses of galactic clouds to be a result of the size-linewidth relation and that they do not require virial equilibrium at all. But, he also argued that the implied value of $n(\text{H}_2)/I_{\text{CO}}$ from the virial masses compared with that derived from γ -rays suggests that while the more massive molecular clouds are probably self-gravitating, clouds with "virial masses" $< 10^4 M_{\odot}$ are strongly influenced by nongravitational forces.
- The absorption coefficient $\kappa_{1200} = 0.37 \text{ cm}^2$ per gram of dust is the Galactic value that assumes a mixture of silicate and amorphous carbon grains with a mass ratio and optical constants as given in Chapter 1. Under the assumption that the formation of dust grains is similar in all kinds of galaxies the same value can be used. However, different metal abundances and different radiation fields may lead to a change in the processing of grains. It is known (e.g. Bazell & Dwek 1990, Ossenkopf 1993) that for fluffy grains composed of subparticles of silicate and amorphous carbon with an admixture of frozen ice the mass absorption coefficient will considerably increase. Krügel & Siebenmorgen (1994) calculated an enhancement by a factor of ten for the submillimeter absorptivity. Such a modification in the value of κ_{1200} would decrease the dust mass M_{d} and increase the R by the same factor.

A common assumption is that dust and gas are well mixed. In this study the identified dust clouds correlate in general with the CO sources. However, sometimes the gas and the dust have a difference in their cloud sizes. In the cases of 30 Dor MMS 6 and N 159 MMS 4 (the two highest R in Table 5.1) the dust concentrates near the center of the observed CO. In other words, the gas extends beyond the dust emission. This increases the respectively R values.

M_{vir} is determined from the CO sources of Johansson (2002) (positions of the dust sources N 44 MMS 2 - 3) and Johansson et al. (1998) (positions of the other dust sources). No CO data or no M_{vir} is available for the detected SIMBA sources not shown in Table 5.1 (e.g. 30 Dor MMS 7 and 9). Therefore, R could not be calculated for these sources. For the dust sources 30 Dor MMS 4 and 10 as well as N 160 MMS 1 and 2 no R could be established as there is CO cloud confusion at these sources. As 30 Dor MMS 5 and N 158 MMS 2 have both a considerable spatial shift from their nearest associated CO clouds, no gas-to-dust ratio was derived for them.

The calculated R values (Table 5.1) have uncertainties ranging between 46% and 71% as they reflect the uncertainties of M_{vir} which are between 10% and 36% and that of M_{d} . R was calculated with the masses shown in Table 3.7.

The ratio R shows a high dispersion in the 30 Dor central field as well as in the southern field (N 158 and N 159). The R of the clouds in the southern area range from values of 19 to 612, while that of the central field go from 68 to 298. As pointed out in Chapter 3, the 30 Dor central field and the southern field have different physical environments. However, no shift was verified in the R values from the central field to the southern one. But it can be concluded that the high R value in N 159 MMS 4, i.e. relatively low amount of dust mass, reflects the tendency seen even more to the south. This SIMBA source is located near the

Table 5.1: Gas masses and molecular gas-to-dust ratios.

| Source | CO cloud | CO size [pc] | M_{vir} [$10^3 M_{\odot}$] | R |
|-----------------|----------|-----------------|--|---------------|
| 30 Dor MMS 2 | 30Dor-10 | 20.1 | 383 ± 38 | 103 ± 50 |
| 30 Dor MMS 6 | 30Dor-17 | 7.0 | 15 ± 4 | 298 ± 149 |
| 30 Dor MMS 8 | 30Dor-22 | 6.8 | 21 ± 4 | 68 ± 31 |
| N 158 MMS 1 | N158-1 | 10.5 | 19 ± 6 | 66 ± 37 |
| N 158 MMS 3 | N158-2 | 9.9 | 11 ± 4 | 19 ± 11 |
| N 159 MMS 1 | N159-E | 19.2 | 168 ± 25 | 168 ± 81 |
| N 159 MMS 2 - 3 | N159-W | 16.7 | 90 ± 14 | 132 ± 92 |
| N 159 MMS 4 | N159-2 | 14.8 | 67 ± 13 | 612 ± 435 |
| N 44 MMS 2 - 3 | 52 | 36.4 | 238 ± 36 | 159 ± 75 |

CO source N 159-S, where no dust has been detected.

If a carbon and silicate abundance like the one mentioned in Chapter 1 is assumed, the gas-to-dust ratio for our Galaxy is $R \sim 150$. The uncertainties in the ratio are introduced by the uncertainties in the dust particle properties with the classical values of R for the Milky Way ranging between 100 and 200 (e.g. Hildebrand 1983).

As the LMC has a lower metallicity than our Galaxy, some R values shown in Table 5.1 seem to be surprisingly small. However, the chemical-abundance estimates for the MCs tend to support the idea of an incomplete mixing of the ISM (e.g. a dispersion of $[\text{Fe}/\text{H}]$ being possible) (Westerlund 1997). In other words, stellar clusters with the same age can form in different processed material. All three cases with lower R results are from small clouds. The R values obtained for the 30 Dor MMS 6 and 8 sources as well as the values for the sources of N 158 have also a uncertainty contribution from the cloud size. The relative size errors increase with the decreasing cloud giving a non-negligible contribution to the uncertainty of small clouds. The cloud size errors are not specified in the virial masses as they are not presented in the CO literature.

As said before the H_2 is not so seriously affected by photodissociation than the CO. If this is a considerable phenomenon the virial mass estimated from CO will be underestimated. So, R and SFE (see Chapter 6) will be, respectively, underestimated and overestimated by the same factor.

In Fig. 5.1 the ratio R is compared with the cloud size and there seems to be no relation between the two variables. Nevertheless, by excluding the two sources with higher R (where the dust is located near the center of the CO emission) the conclusion is that both variables in Fig. 5.1 increase with each other.

Johansson et al. (1998) found - for their CO sample - a correlation between the CO luminosity and the cloud size as well as one between the line width and the cloud size.

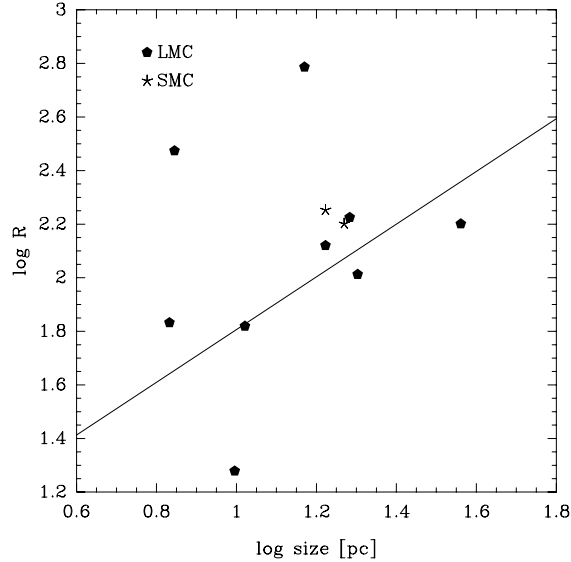


Figure 5.1: Comparison of cloud size and molecular gas-to-dust ratio. The continuous line is a least squares fit to the data (without the two points of higher R).

5.2 Gas-to-dust Ratio R in the SMC

As displayed in Chapter 4, the geometry of the detected SIMBA sources in the SMC in the regions N 12 and N 27 are not elongated such as the ones in the LMC regions. As they are more circular Eq. (5.1) is used directly. This method was used by Rubio, Lequeux & Boulanger (1993) for several molecular clouds in the SMC. The values of M_{vir} derived in their paper for the two regions also mapped with SIMBA are given in Table 5.2. The molecular gas-to-dust ratios R calculated through Eq. (5.3) using the dust masses shown in Table 4.4 and the virial masses are also given in Table 5.2. The uncertainties presented for M_{vir} reflect the errors in the line width which are like those in the LMC. The uncertainties of R are approximately 30% reflecting those of M_{vir} (15% to 25%) and M_{d} .

Table 5.2: Gas masses and molecular gas-to-dust ratios.

| Source | CO cloud | CO size [pc] | M_{vir} [$10^3 M_{\odot}$] | R |
|----------------|----------|-----------------|--|--------------|
| N 12 MMS 1 - 2 | 8 | 18.6 | 51 ± 13 | 159 ± 52 |
| N 27 MMS 1 - 3 | 20 | 16.7 | 120 ± 18 | 179 ± 48 |

The similar values of N 12 and N 27 are not a surprise as both are intense and compact HII

regions and are located close to each other. Compared to the Galactic value of $R \sim 150$ the average SMC value ($R = 169$) is similar, but there are only two data points available for regions in this galaxy. The remarks mentioned in the former section about the determination and scatter of R are also valid in the SMC.

No M_{vir} is available for the other two sources shown in Table 4.4 (H 15 MMS 1 and N 88 MMS 1). Therefore, R could not be calculated for them.

5.3 R Estimate through Indirect Method

Table 5.3: Estimated molecular gas-to-dust ratios of the remaining sources in the MCs.

| Source | R |
|---------------|---------------|
| 30 Dor MMS 1 | 227 ± 118 |
| 30 Dor MMS 3 | 197 ± 102 |
| 30 Dor MMS 4 | 155 ± 81 |
| 30 Dor MMS 5 | 266 ± 138 |
| 30 Dor MMS 7 | 146 ± 70 |
| 30 Dor MMS 9 | 39 ± 10 |
| 30 Dor MMS 10 | 28 ± 7 |
| N 158 MMS 2 | 65 ± 33 |
| N 160 MMS 1 | 99 ± 74 |
| N 160 MMS 2 | 102 ± 76 |
| N 160 MMS 3 | 126 ± 73 |
| N 160 MMS 4 | 140 ± 81 |
| N 44 MMS 1 | 58 ± 15 |
| N 44 MMS 4 | 62 ± 16 |
| N 44 MMS 5 | 69 ± 17 |
| N 44 MMS 6 | 64 ± 37 |
| N 44 MMS 7 | 140 ± 81 |
| N 113 MMS 1 | 74 ± 23 |
| N 113 MMS 2 | 140 ± 43 |
| N 113 MMS 3 | 193 ± 60 |
| N 214 MMS 1 | 279 ± 145 |
| N 214 MMS 2 | 141 ± 73 |
| H 15 MMS 1 | 604 ± 181 |
| N 88 MMS 1 | 264 ± 74 |

In the two former subsections R could not be derived for all SIMBA sources as M_g was not completely available. In Chapter 6, more precisely through Eq. (6.1a) and (6.2a), the M_g is derived from the respectively FIR luminosity for the remaining sources. Therefore, from these data also R can be estimated. The results are shown in Table 5.3. The uncertainty of R ranges from 25% to 75%. It reflects the errors of M_g , which are a combination of the uncertainties of L_{FIR} and of Eq. (6.1), as well as the errors of M_d .

The R values show a high dispersion as the ones shown in Table 5.1.

In the SMC Stanimirovic (1999) also found a considerable dispersion (see introduction of this chapter) in the dust-to-gas mass ratio of individual regions.

Given the uncertainties of the R only for some of the objects listed in the Tables 5.1 to 5.3 a detailed classification in relation to the galactic range is possible. Therefore, the R of the 30 Dor C and N 158C regions in the LMC can be clearly specified as lower than galactic values and that of H 15 in the SMC as higher than galactic ones.

A east-west assymetry can be verified in the 30 Dor central complex. The difference in the gas-to-dust ratio, with the highest values in 30 Dor A and the lowest ones in 30 Dor C, is not unique for the LMC. Fitzpatrick (1986) observed a $N(\text{HI})/E(\text{B-V})$ ratio with 30 Dor stars having higher values than non-30 Dor stars. One of Xu et al. (1992) hypothesis to explain the east-west assymetry on the FIR-to-6.3 cm brightness ratio in the LMC was a difference in the gas-to-dust ratio.

When the temperature of a region is lower the gas-to-dust ratio decreases because of the increase of M_d . This is also clearly seen in the central part of 30 Dor with $17 \text{ K} \leq T_d \leq 24 \text{ K}$ where 30 Dor C has the lowest R .

A north-south assymetry is revealed for the 30 Dor southern HII regions. The variation in the R shows the highest values in N 159 and the lowest ones in N 158C. However, the difference may also be explained by a east-west assymetry: less variations in the R between N 158C, N 160 and N 159 compared with the ones in the 30 Dor central complex could be associated to the lower east-west distance in the 30 Dor southern area.

In the N 44 complex the calculated source (Table 5.1) presents a R value (84-234) practically in the galactic range. Differently the estimated clouds in N 44 provide gas-to-dust ratios mostly below the Milky Way values (not considering N 44 MMS 7 as it is much less massive in CO and dust). This reveals a bimodal behavior in the interstellar complex in question.

The estimated R s of the N 113 and N 214 regions show a correlation with the cloud size. The smaller clouds have higher R indicating that they are losing cool dust in the fragmentation process.

The R results of the SMC sources given in Table 5.3 are higher (H 15) than the galactic values or range from the galactic to higher ones (N 88). H 15 is located, like N 12 and N 27, in the SW part of the SMC Bar, however it is a region with different properties (see Chapter 4).

Dwarf galaxies have usually stochastic star formation and chemical evolution making it commonly hard to detect a radial dependence in their dust-to-gas ratio. Stanimirovic (1999) firstly suggested for a dwarf galaxy, in that case the SMC, a radial gradient for M_d/M_{HI} . In the present work neither in the LMC nor in the SMC a radial dependence of R could be observed. A larger data set is needed to confirm or deny a radial dependence.

Chapter 6

Star Formation Efficiency in the LMC and the SMC

The ratio $L_{\text{FIR}}/M_{\text{g}}$ is often referred to as star formation efficiency (SFE). In this ratio the FIR emission, which is the tracer of the current star formation rate, is normalized by the gas mass available to form stars. In other words, the ratio gives the efficiency of converting gas into stars. Since the recognition that star formation takes place in molecular clouds, studies of the SFE consider the relationship between stars and molecular gas.

The FIR luminosity is here defined as the luminosity between 12 μm and 1.2 mm. For 12 μm to 100 μm a trapezoid formula is used to obtain the flux whereas between 100 μm and 1.2 mm the corresponding modified Planck function of the form $\nu^m B_{\nu}(T_{\text{d}})$ ($m = 2.0$) is integrated.

As the environment in question consists of molecular clouds, M_{g} can be constrained as shown in Chapter 5 ($M_{\text{vir}} \sim M_{\text{H}_2} \sim M_{\text{g}}$). This means that the values shown in Tables 5.1 and 5.2 are used, respectively, to obtain the results presented in Tables 6.1 and 6.3.

It is assumed that the FIR luminosity of the individual sources in each region (30 Dor A, 30 Dor B, etc) has a distribution like that of their dust masses (e.g. N 159 MMS 1 has 55% of the dust mass of the N 159 dust cloud, so N 159 MMS 1 has 55% of the total L_{FIR} of the N 159 complex). The temperatures used in this chapter are those derived from the SEDs displayed in former chapters.

The uncertainties given for L_{FIR} range from 14% to 32% as they are a combination from three other uncertainties: the IRAS fluxes uncertainties (15%), the SIMBA and MOPSI ones (varying together between 11% and 18%) and the radio contamination ones (9% in the LMC and 20% in the SMC).

6.1 FIR Luminosity versus Molecular Mass in the LMC

The star formation process can be classified as follows (Gao et al. 2001):

- SFE $< 4 L_{\odot}/M_{\odot}$ - weak

Table 6.1: SFEs in the LMC.

| Source | L_{FIR} [$10^3 L_{\odot}$] | $L_{\text{FIR}}/M_{\text{g}}$ [L_{\odot}/M_{\odot}] |
|-----------------|--|--|
| 30 Dor MMS 2 | 13865 ± 2634 | 36.2 ± 7.6 |
| 30 Dor MMS 6 | 49 ± 11 | 3.2 ± 1.1 |
| 30 Dor MMS 8 | 340 ± 75 | 16.2 ± 4.7 |
| N 158 MMS 1 | 105 ± 26 | 5.5 ± 2.3 |
| N 158 MMS 3 | 210 ± 52 | 19.1 ± 8.4 |
| N 159 MMS 1 | 2627 ± 657 | 15.6 ± 4.5 |
| N 159 MMS 2 - 3 | 1775 ± 444 | 19.7 ± 5.9 |
| N 159 MMS 4 | 284 ± 71 | 4.2 ± 1.3 |
| N 44 MMS 2 - 3 | 1655 ± 381 | 7.0 ± 1.9 |

- $4 L_{\odot}/M_{\odot} \leq \text{SFE} < 10 L_{\odot}/M_{\odot}$ - normal (e.g. giant molecular clouds in the Galactic disk)
- $10 L_{\odot}/M_{\odot} \leq \text{SFE} < 20 L_{\odot}/M_{\odot}$ - moderate starburst
- $\text{SFE} \geq 20 L_{\odot}/M_{\odot}$ - powerful starburst

Different values in the SFE express from a quiescent steady state to starburst. A considerable high SFE can be caused by an increased efficiency for converting gas into stars and a bias of the IMF towards higher masses (Krügel et al. 1988).

The average value in solar units of $L_{\text{FIR}}/M_{\text{g}}$ in the 30 Dor central area is found to be 18.5, ranging from 3.2 to 36.2. In the 30 Dor southern HII regions it is found to be 12.8, ranging from 4.2 to 19.7. In the N 44 region the derived value is 7.0. From the nine studied regions in the LMC the SFE is weak to normal in four areas and suggests a moderate starburst in other four as well as a powerful starburst in 30 Dor MMS 2 (see Table 6.1). The uncertainty of SFE (ranging between 21% and 44%) comes from the L_{FIR} and M_{g} previously mentioned errors.

The values found for the 30 Dor central field and the 30 Dor southern HII regions show a lot of variation even in the same region. The highest and the lowest SFEs are obtained in 30 Dor MMS 2 and 6, respectively. These very distinct results come, respectively, from the strongest and the weakest source detected in the LMC with SIMBA.

The highest $L_{\text{FIR}}/M_{\text{g}}$ in the more hostile environment (the core of the 30 Dor nebula) shows that the SFE is sensitive to the UV flux: when the radiation field goes up the $L_{\text{FIR}}/M_{\text{g}}$ ratio increases. The UV flux in 30 Dor MMS 2 ($9.4 \text{ erg s}^{-1} \text{ cm}^{-2}$) is about 15 times that in N 159 MMS 2 - 3 ($0.4 - 0.96 \text{ erg s}^{-1} \text{ cm}^{-2}$) (Heikkilä, Johansson & Olofsson 1999).

The relation between FIR luminosity L_{FIR} and gas mass M_{g} for the MCs is shown in Fig. 6.1. The fit through the data points included in Table 6.1 yields for the LMC

$$\log(L_{\text{FIR}}) = (1.24 \pm 0.07)\log(M_{\text{g}}) - (0.10 \pm 0.35). \quad (6.1)$$

In Table 6.1 only the same sources already presented in Table 5.1 are used, following the reasons shown in Chapter 5. Therefore, SFE could not be calculated directly for all sources.

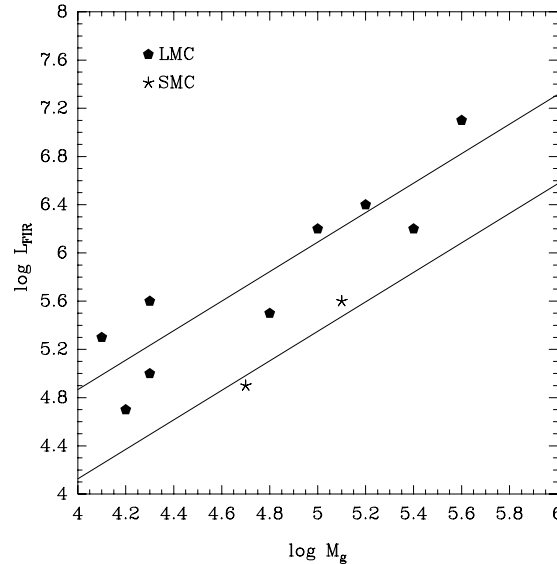


Figure 6.1: The FIR luminosity L_{FIR} versus the gas mass M_g .

However, the FIR luminosity is available for each source. Since Eq. (6.1) gives a good correlation, it is possible to estimate M_g with the FIR data available for the remaining LMC sources detected with SIMBA ($\log(M_g) = (0.66 \pm 0.04)\log(L_{\text{FIR}}) + (0.93 \pm 0.26)$) (Eq. (6.1a)). Thus, SFE was also derived and the results for these sources are given in Table 6.2. The uncertainties given for SFE range from 25% to 42% as they reflect the uncertainties of L_{FIR} and the correlation of Eq. (6.1) (error of 17%).

For the 22 additional sources, the SFE can be classified as weak to normal in 13 areas and suggests a moderate starburst in other eight, as well as one powerful starburst. From these nine higher values four are located in 30 Dor A including the three highest.

30 Dor MMS 2 and 4 are sites of the most intense starbursts, while the other three sources in 30 Dor A reveal a more moderate starburst. In N 159 (N 159 MMS 1 - 3) the derived SFE suggests the level of a moderate starburst. These all are clear signs of ongoing massive star formation and is in agreement with the fact that numerous IR sources had been detected by Rubio et al. (1998) and Rubio, Roth & Tapia (1990) through J, H and K images in two fields of 30 Dor A (30 Dor MMS 2 - 4) and a field of N 159, respectively.

The SFE values of the SIMBA sources located towards N 160A (N 160 MMS 1 - 2) and N 158 (N 158 MMS 3) indicate a moderate starburst. This result is in agreement with the fact that Boreiko & Betz (1991) found in N 160A and N 158 a good spatial correlation between FIR continuum and CII emission indicating that the dust emission comes from relatively dense regions near early-type stars. Testor & Niemela (1998) found that LH 101 in N 158C has several reddened unevolved early O stars and unreddened evolved massive stars, with the two

Table 6.2: Estimated SFEs of the remaining sources in the LMC.

| Source | L_{FIR} [$10^3 L_{\odot}$] | M_{g} [$10^3 M_{\odot}$] | $L_{\text{FIR}}/M_{\text{g}}$ [L_{\odot}/M_{\odot}] |
|---------------|--|--|--|
| 30 Dor MMS 1 | 2048 ± 389 | 125 ± 26 | 16.4 ± 4.6 |
| 30 Dor MMS 3 | 3151 ± 599 | 166 ± 35 | 19.0 ± 5.3 |
| 30 Dor MMS 4 | 5829 ± 1108 | 248 ± 52 | 23.5 ± 6.6 |
| 30 Dor MMS 5 | 1260 ± 239 | 90 ± 19 | 13.9 ± 3.9 |
| 30 Dor MMS 7 | 194 ± 43 | 26 ± 6 | 7.4 ± 2.4 |
| 30 Dor MMS 9 | 59 ± 9 | 12 ± 2 | 4.9 ± 1.2 |
| 30 Dor MMS 10 | 147 ± 22 | 22 ± 4 | 6.7 ± 1.7 |
| N 158 MMS 2 | 87 ± 22 | 16 ± 4 | 5.6 ± 1.9 |
| N 160 MMS 1 | 790 ± 253 | 66 ± 18 | 11.9 ± 5.0 |
| N 160 MMS 2 | 753 ± 241 | 64 ± 17 | 11.7 ± 4.9 |
| N 160 MMS 3 | 95 ± 27 | 16 ± 4 | 5.8 ± 2.2 |
| N 160 MMS 4 | 63 ± 18 | 13 ± 3 | 5.0 ± 1.9 |
| N 44 MMS 1 | 563 ± 84 | 53 ± 11 | 10.6 ± 2.6 |
| N 44 MMS 4 | 312 ± 44 | 36 ± 7 | 8.7 ± 2.2 |
| N 44 MMS 5 | 187 ± 26 | 26 ± 5 | 7.3 ± 1.8 |
| N 44 MMS 6 | 288 ± 86 | 34 ± 9 | 8.4 ± 3.4 |
| N 44 MMS 7 | 26 ± 8 | 7 ± 2 | 3.7 ± 1.5 |
| N 113 MMS 1 | 1558 ± 265 | 104 ± 21 | 15.0 ± 3.9 |
| N 113 MMS 2 | 213 ± 36 | 28 ± 6 | 7.6 ± 2.0 |
| N 113 MMS 3 | 71 ± 12 | 14 ± 3 | 5.2 ± 1.4 |
| N 214 MMS 1 | 74 ± 17 | 14 ± 3 | 5.3 ± 1.7 |
| N 214 MMS 2 | 594 ± 137 | 55 ± 13 | 10.8 ± 3.6 |

groups being spatially separated. They suggested a propagating star formation in LH 101. The different SFE values from N 158 MMS 1 - 3 reinforce this scenario.

LH 90, located in 30 Dor C, is the second association of the LMC for its richness in WR stars (Lortet & Testor 1984). The heavy presence of WR stars could be partially responsible for their lower SFE values.

Considering the values and the uncertainties derived in Tables 6.1 and 6.2 the star formation efficiencies of the different regions can be ordered in the following sequence going from the higher to the lower activity stages: 30 Dor A, N 159, N 158C, 30 Dor B, N 113, N 160A, N 44, N 214, 30 Dor C, N 160 MMS 3 - 4.

A substantial variation in the SFE within a galaxy represents the temporal evolution of star forming regions in molecular cloud complexes or localized bursts of star formation. It is here very well seen in the LMC.

For a sample of Im and Sm galaxies Albrecht (2000) found from the $L_{\text{FIR}}/M_{\text{HI}}$ ratio (where L_{FIR} was defined in the same way as in this thesis) mean values for the SFE in solar units of 6 and 5.4, respectively. These results were obtained with 1.3 mm data and not at 1.2 mm, which results in only slightly higher values for L_{FIR} . His results support the idea of lower

activity stages in dwarf galaxies. In the present work it can be seen that individual regions of LMC exhibit activity stages well above these mean values.

6.2 FIR Luminosity versus Molecular Mass in the SMC

The values of $L_{\text{FIR}}/M_{\text{g}}$ in the SMC (Table 6.3) where the SFE could be derived directly, range from 1.5 to 3.0 in solar units. These results indicate an average SFE in the SMC much lower than that in the LMC, but the SFE could only be calculated for two regions. The SFE of N 27 has an uncertainty of 23% whereas for N 12 it is 30%. This comes from the errors of the respectively L_{FIR} and M_{g} .

Table 6.3: SFEs in the SMC.

| Source | L_{FIR} [$10^3 L_{\odot}$] | $L_{\text{FIR}}/M_{\text{g}}$ [L_{\odot}/M_{\odot}] |
|----------------|--|--|
| N 12 MMS 1 - 2 | 75 ± 13 | 1.5 ± 0.4 |
| N 27 MMS 1 - 3 | 364 ± 62 | 3.0 ± 0.7 |

Table 6.4: Estimated SFEs of the remaining regions in the SMC.

| Source | L_{FIR} [$10^3 L_{\odot}$] | M_{g} [$10^3 M_{\odot}$] | $L_{\text{FIR}}/M_{\text{g}}$ [L_{\odot}/M_{\odot}] |
|------------|--|--|--|
| H 15 MMS 1 | 111 ± 18 | 60 ± 12 | 1.8 ± 0.5 |
| N 88 MMS 1 | 98 ± 16 | 55 ± 11 | 1.8 ± 0.5 |

The L_{FIR} in the SMC seems to correlate with the M_{g} in a similar way as in the LMC (Fig. 6.1). So the same slope is admitted. Thus, the relation between the FIR luminosity L_{FIR} and the gas mass M_{g} in the SMC gives

$$\log(L_{\text{FIR}}) = 1.24\log(M_{\text{g}}) - 0.85. \quad (6.2)$$

In the same way as proceeded for the LMC, the SFE for the two remaining SMC regions was derived in Table 6.4 ($\log(M_{\text{g}}) = 0.66\log(L_{\text{FIR}}) + 1.45$) (Eq. (6.2a)). Admitting a straight line connecting both SMC points in Fig. 6.1, the SFE values for H 15 and N 88 would be, respectively, 1.8 and 1.7: very similar to the values presented in Table 6.4.

As it can be seen, all regions studied in the SMC show low values of SFE. This is in agreement with other studies for this galaxy.

6.3 Star Formation Efficiency versus Dust Temperature

In Fig. 6.2 the ratio $L_{\text{FIR}}/M_{\text{g}}$ (given in Tables 6.1 and 6.3) and the dust temperature of the coldest component are compared. A higher SFE stands for a higher number of young

stars which heat more the dust. This implies that $L_{\text{FIR}}/M_{\text{g}}$ increases with T_{d} . In spite of the scatter, the data indicate a correlation between the SFE and the temperature of the coldest dust component with the former increasing with T_{d} . So the comparison among the different regions with distinct temperatures (the dust temperatures in the individual areas range between 20 K and 24 K in the LMC and between 17 K and 18 K in the SMC) determine the relation

$$\log(L_{\text{FIR}}/M_{\text{g}}) = -1.54 + 0.11T_{\text{d}}. \quad (6.3)$$

This equation shows that $L_{\text{FIR}}/M_{\text{g}}$ establishes a minimal temperature for the bulk of dust.

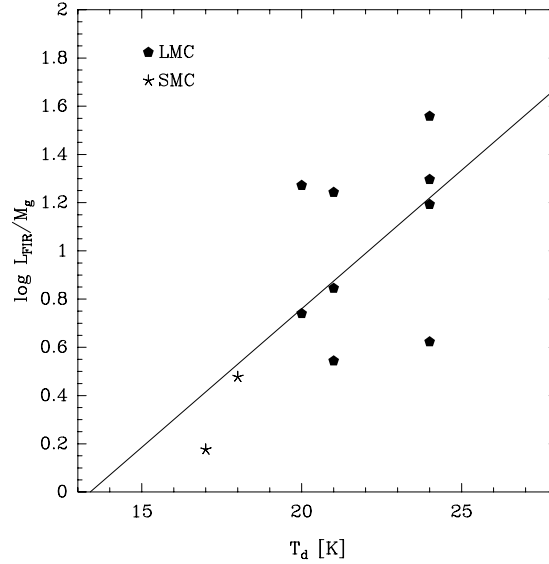


Figure 6.2: Comparison of the coldest dust component and star formation efficiency in the MCs. The continuous line is a least squares fit to the data.

As the two regions in the SMC present a behavior similar to the regions in the LMC, in this case the equation was calculated with the data for both galaxies.

A dependence between $\log(L_{\text{FIR}}/M_{\text{g}})$ and the minimal temperature of the bulk of dust fitted by Chini et al. (1989) ((sub)millimeter data with 1.3 mm instead of 1.2 mm) for different types of objects, including normal spirals, compact HII regions, starburst galaxies and QSOs, is similar ($\log(L_{\text{FIR}}/M_{\text{g}}) = -1.44 + 0.12T_{\text{d}}$).

Eq. (6.3) is used to estimate the ratio of the FIR luminosity to the gas mass for the regions detected with SIMBA in the MCs, but not shown in Tables 6.1 and 6.3. The SFE results are given in Table 6.5 and the uncertainties are approximately 60%, which come from the uncertainties of Eq. (6.3) and that of T_{d} .

From the 14 regions presented in Table 6.5 the SFE indicates weak to normal star formation

Table 6.5: Estimated SFEs of the remaining regions in the MCs.

| Source | $L_{\text{FIR}}/M_{\text{g}}$ [L_{\odot}/M_{\odot}] |
|-------------------|--|
| 30 Dor MMS 1 | 16.6 ± 10.0 |
| 30 Dor MMS 3 - 5 | 16.6 ± 10.0 |
| 30 Dor MMS 7 | 7.5 ± 4.3 |
| 30 Dor MMS 9 - 10 | 2.6 ± 1.5 |
| N 158 MMS 2 | 5.8 ± 3.3 |
| N 160 MMS 1 - 2 | 9.8 ± 5.7 |
| N 160 MMS 3 - 4 | 5.8 ± 3.3 |
| N 44 MMS 1 | 4.4 ± 2.5 |
| N 44 MMS 4 - 5 | 4.4 ± 2.5 |
| N 44 MMS 6 - 7 | 5.8 ± 3.3 |
| N 113 MMS 1 - 3 | 7.5 ± 4.3 |
| N 214 MMS 1 - 2 | 12.7 ± 7.5 |
| H 15 MMS 1 | 5.8 ± 3.3 |
| N 88 MMS 1 | 2.6 ± 1.5 |

activity in 10 areas and suggests a moderate starburst in the remaining four areas.

By comparing the SFE values of the LMC and the SMC estimated, respectively, through Eq. (6.1a) and Eq. (6.2a) with those obtained through Eq. (6.3) it can be realized that the first method is better. Only three different temperatures are available for LMC and two for the SMC (Fig. 6.2) which gives a not so good correlation as the one obtained with the data displayed in Fig. 6.1. In Table 6.5 average values could be derived (14 regions instead of the 24 sources in Tables 6.2 and 6.4). For the 14 regions seven different temperatures have been calculated in former chapters, thus four regions have the same calculated SFE (they have the same estimated dust temperature, 20 K). Nevertheless the results are in general agreement with the values presented in Tables 6.2 and 6.4 (considering the involved uncertainties). For several sources the estimates of SFE are practically the same as in Table 6.2 (30 Dor MMS 1, 30 Dor MMS 7, N 158 MMS 2, N 160 MMS 3, N 160 MMS 4).

6.4 Star Formation Efficiency from FIR and $H\alpha$

For the sources where the gas mass M_{g} is available and not derived from the FIR luminosity L_{FIR} (Tables 6.1 and 6.3) the SFE can also be analyzed only with the integrated IRAS fluxes contribution to the luminosity. The contribution of the luminosity between 12 and 100 μm ranges in the LMC from 66% to 83% and in the SMC from 40% to 59% of the L_{FIR} (luminosity between 12 μm and 1.2 mm). The SFE calculated taking into account only the part of the luminosity obtained with the trapezoid formula for the sources in the LMC and the SMC is obviously lower than the derived respectively in Tables 6.1 and 6.3, but the classification of the sources did not change.

Considering the $H\alpha$ flux calculated by Heikkilä, Johansson & Olofsson (1999) for the central

part of 30 Dor, the outer edge of 30 Dor, N 159W and N 160 in the LMC and N 27 in the SMC combined with the M_{vir} derived from the associated CO clouds obtained by Johansson et al. (1998) the star formation efficiency using the ratio $L_{\text{H}\alpha}/M_{\text{H}_2}$ (assuming $M_{\text{vir}} \sim M_{\text{H}_2}$) is calculated (see Table 6.6).

Rownd & Young (1999) define as starburst any region with $\log(\text{SFE}) > -1.35$. The results in Table 6.6 are in general agreement with the results obtained for these sources in the present work: 30 Dor MMS 2 and N 27 are the sources with, respectively, the highest and the lowest star formation efficiency.

A good general agreement between IRAS and H α emission is observed in the LMC by Schwing (1988). The IR emission also follows well the H α one in the SMC, except in the northern part.

Table 6.6: H α and derived SFE.

| Source | CO cloud | $L_{\text{H}\alpha}$ [$10^3 L_{\odot}$] | M_{H_2} [$10^3 M_{\odot}$] | $\log(\text{SFE})$ [L_{\odot}/M_{\odot}] |
|-----------------|-----------------|--|--|---|
| 30 Dor MMS 2 | 30 Dor-10 | 35 | 383 | -1.04 |
| 30 Dor MMS 10* | 30 Dor-27 | 1.9 | 24 | -1.10 |
| N 159 MMS 2 - 3 | N 159W | 3.9 | 90 | -1.36 |
| N 160 MMS 1 - 2 | N 160-1,2,3,4,5 | 3.8 | 130 | -1.53 |
| N 27 MMS 1 - 3 | 20 | 1.4 | 120 | -2.93 |

*Not completely coincident.

6.5 Final Remarks

In Fig. 6.3 the cloud size is compared with the dust temperature whereas in Fig. 6.4 the $L_{\text{FIR}}/M_{\text{g}}$ ratio is compared with the cloud size. In both cases no relation seems to exist between the variables.

The sources studied in the LMC are basically associated to the 30 Dor giant complex which is marked with multiple signs of star formation. Therefore, the SFE values are in general high (specially in its core: 30 Dor A). So, the values derived in this chapter for LMC are biased towards higher activity stages. For the SMC the SFE results were obtained for a small sample of regions. Three of the studied star formation sites which presented dust detections are located in the SW part of the Bar, while further out of this part of the optical bar only one HII region with dust detection was found (N 88). So in order to weight the importance of the variation of the local phenomena through the LMC and the SMC on the values of the SFE one must await more (sub)millimeter data.

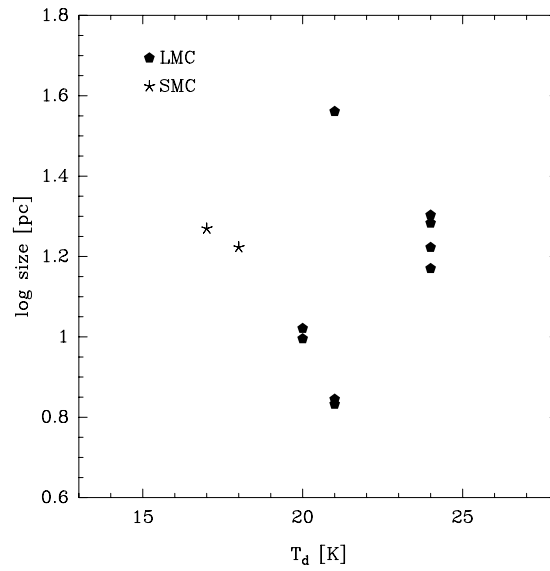


Figure 6.3: Comparison of the coldest dust component and cloud size.

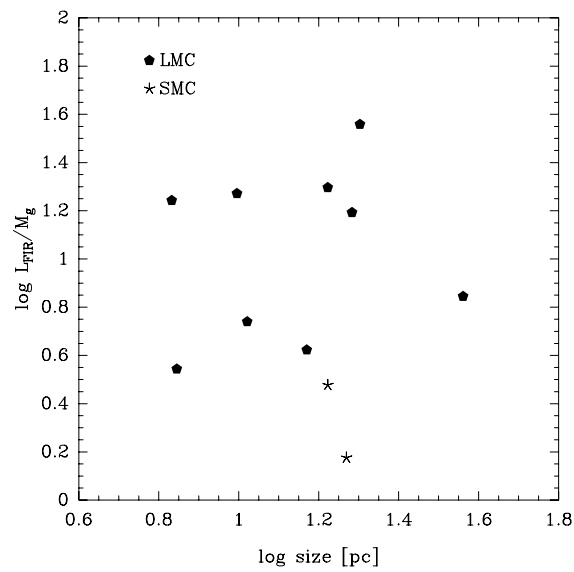


Figure 6.4: Comparison of cloud size and star formation efficiency in the MCs.

Chapter 7

Summary and Outlook

7.1 Summary

This thesis presents first 1.2 mm continuum survey in the Magellanic Clouds. The observations were performed with SIMBA at the SEST, which is currently the only submillimeter telescope in the Southern Hemisphere. The MCs have been observed at four ESO and two Swedish observing runs, totalizing about 160 h of integration time on MC sources. The data reduction of the 1.2 mm measurements was performed by using the MOPSI software package. This study comprises star forming regions with CO detections extracted from Israel et al. (1993) and Johansson et al. (1998), respectively, the first and the seventh part of the ESO-SEST Key Programme: *CO in the Magellanic Clouds*.

Johansson et al. (1998) mapped the central part of the 30 Doradus nebula and the southern HII regions N 158C, N 159 and N 160. From their 50 CO sources, 38 have been investigated for dust continuum emission. For 20 of them one or more positive detections have been obtained totalizing 21 observed dust sources.

Israel et al. (1993) observed CO towards 92 positions in the LMC and 42 in the SMC. In the LMC, four of the brightest sources from those not located in the 30 Dor complex were selected. In the N 44 (two positions), N 113 and N 214 nebulae, a total of 12 dust sources have been revealed.

In the SMC, the observations coordinates were based on Israel et al. (1993) and oriented towards selected regions located in the SW Bar, in the northern Bar and in the Shapley Wing. The spatial distribution of the star forming regions was chosen in order to get an idea of the cool dust across this dwarf galaxy. From the eight studied star formation sites four presented dust detections. Three of them are located in the SW part of the Bar, while further out of this part of the optical bar only one HII region with dust detection was found (N 88). As expected, the two brightest CO sources included in this study (N 12, N 27) have associated dust sources.

In the SMC seven dust sources have been obtained, distributed through four mosaics. Together with the ones shown in the eight mosaics of the LMC, the survey resulted in a total number of 40 (sub)millimeter sources for the two galaxies. All of them are new detections. The SMC sources have on average smaller sizes than those of the LMC.

Comparing the 1.2 mm integrated fluxes of the LMC sources with those of the SMC sources, it is clear that the former are, on the average, considerably higher. This result is expected as the SMC has a lower metallicity and a higher radiation field.

From the detected dust sources several properties were obtained. As at 100 μm and 1.2 mm the grains are in thermal equilibrium with the interstellar radiation field these wavelengths, which were respectively taken with IRAS and SIMBA, were combined to find the dust temperature. The 1.2 mm emission might be not entirely due to thermal dust emission, with the possibility that synchrotron and/or free-free emission make up a non-negligible contribution. By taking radio fluxes into consideration, the synchrotron emission contribution always showed up to be negligible unlike the contribution of the free-free emission. The inferred temperatures for the different regions range from 17 ± 1 K to 24 ± 5 K in the LMC and 17 ± 1 K to 20 ± 2 K in the SMC, with an average value of about 21 K and 18 K, respectively, in the LMC and in the SMC. The derived dust masses range from $50 \pm 26 M_{\odot}$ to $3700 \pm 1800 M_{\odot}$ in the LMC and from $42 \pm 9 M_{\odot}$ to $350 \pm 80 M_{\odot}$ in the SMC.

The virial theorem was used to obtain the gas mass from the associated CO detections. In some of the sources the dust and CO cloud sizes are different. In the two cases of the highest calculated gas-to-dust mass ratio R in the LMC the gas to dust cloud size ratio is also highest. The calculated and the estimated R values show a high dispersion through the individual regions in the LMC as well as in the SMC. The variations in the ratio R show a east-west asymmetry in the 30 Dor central complex, a north-south asymmetry in the 30 Dor southern HII regions, a bimodal behavior in the N 44 complex and a correlation with the cloud size in the N 113 and N 214 regions. In the SMC, the two mapped intense and compact HII regions located in the SW Bar have similar R values, while the other areas show different molecular gas-to-dust ratios.

The IRAS 12, 25 and 60 μm data were used together with IRAS 100 μm and SIMBA 1.2 mm to obtain the FIR luminosity. The ratio $L_{\text{FIR}}/M_{\text{g}}$ is defined in this work as star formation efficiency. The 30 Dor A region has the highest average star formation efficiency among the investigated areas in the MCs with the individual sources indicating a moderate ($10 L_{\odot}/M_{\odot} \leq \text{SFE} < 20 L_{\odot}/M_{\odot}$) to powerful starburst ($\text{SFE} \geq 20 L_{\odot}/M_{\odot}$), another evidence that it is a site of ongoing massive star formation. In the 30 Dor B region as well as in the southern HII regions (N 158, N 159 and N 160) several sources are present with SFEs that suggest a moderate starburst. Unlike the LMC, all regions studied in the SMC show low SFEs ($\text{SFE} < 4 L_{\odot}/M_{\odot}$). This result is in agreement with other studies for the SMC.

7.2 Outlook

It is desirable to enlarge the present data set, as the observations were only carried out for selected star forming regions in the LMC and in the SMC. So, the analysis presented in this work can be considered as a basis for further investigations in the (sub)millimeter wavelength range, in these two dwarf irregular galaxies.

As the SEST has been closed, research using SIMBA is no longer possible. Therefore, the MCs survey with this instrument is considered completed. Further research will be possible in the near future with APEX (Atacama Pathfinder EXperiment) and, later on, with ALMA

(Atacama Large Millimeter Array). APEX is a submillimeter telescope with a diameter of 12 m. In international collaboration, the MPIfR (Max-Planck-Institut für Radioastronomie in Bonn, Germany), the AIRUB (Astronomisches Institut der Ruhr-Universität Bochum, Germany), the ESO (European Southern Observatory) and the OSO (Onsala Space Observatory, Sweden) have started this project. APEX, as implied in the name, will serve as a pathfinder for ALMA, finding target sources for the future interferometer array. On APEX will be installed a new bolometer array (LABOCA: LARge BOLometer CAMera) with 313 channels for 870 μm wavelength, which is being built through a Bonn/Bochum/Jena collaboration. As this new bolometer will have a larger field of view than SIMBA and also a higher spatial resolution, the observing efficiency will be increased. The idea is in the future implement APEX in the ALMA array. Both APEX and ALMA will be built at the best suited site for submillimeter observations, on the Chajnantor Plateau in the Chilean Andes at an altitude of 5000 m, because of its location in the dry Atacama desert and because of its high altitude. APEX operations are expected to start this year. ALMA will be an array comprising 64 (sub)millimeter antennas, each with a diameter like the APEX, with baselines extending up to 10 km. Its receivers will cover the range from 70 to 900 GHz. ALMA will be the largest ground-based astronomy project in the current decade, coming into operation by the end of it. It will only be comparable to the VLA (Very Large Array), which is used at radio wavelengths, offering an incredible increase in spatial resolution if compared with the SEST.

So subsequent studies will improve the understanding of how the local ambient conditions influence the dust clouds, the molecular gas-to-dust ratio and the star formation efficiency. The systematical survey in the LMC and the SMC will provide a good statistical knowledge between the several local parameters and the properties of the dust clouds. A better determined gas-to-dust ratio R for the MCs will help to better establish the distance of galaxies at high redshifts.

Appendix A

Reduction of the Bolometer Data

To reduce the SIMBA data several MOPSI macros were used which were applied in the following shown iterative sequence. The commands used were explained in the section 2.5. The presented reduction procedures are the most used form which suffered only minor alterations in the case of a few regions (e.g. some of the data was reduced with the routine `cdeconv` instead of `deconv` as at the very beginning of the observing time the backend was configured for a DC couple array).

A.1 First generation:

```
!clear file lists
init in-l
init out-l

i-d name of input directory
o-d name of output directory

!load file list
lis name of input list
lis
pause

!reduce given files in a loop
for i 1 to last
read i

init gfit
init histo

del dc
!delete noisy channels
del rc 2 12
init spike

base t 5

set mask
```

```
> 5 rms
< -5 rms
inter blan neigh 4 4
mask

base r az < 1e9 > -1e9
base t 5
base l 0

set mask
deconv
mask

corr ge
tau tau 20000
corr ext

base t 5
base l 4
store weight rms2 az < 1e9 > -1e9

snf no sou dr 105 9999 best 6 < -5 rms > 5 rms
no plots
run

multi cal. Factor

cl
plot
!write channel maps to disk
write .btd +name of region
next

!declare saved files as new input list
repl in-l out-l
!load the first data file as a reference
read 1
!create final map
convert comm
proj <hh:mm:ss> <dd:mm:ss>
ext <Ra> <Dec>
blc < ΔRa> < ΔDec>
pix 8 8
run all
quit

file out name of region.gdf
wri

cl
plo

exit
```

A.2 Second generation:

The polygon used in this second step is shaped from the final map of the first generation.

```
init in-l
init out-l

i-d name of input directory
o-d name of output directory

lis name of input list
lis
pause

for i 1 to last
read i

init gfit
init histo

del dc
del rc 2 12
init spike

pol name of polygon
base r out, sys equa proj <hh:mm:ss> <dd:mm:ss>

base t 5
base l 0

set mask
> 5 rms
< -5 rms
inter blan neigh 4 4
mask

base t 5
base l 0

set mask
deconv
mask

corr ge
tau tau 20000
corr ext

base t 5
base l 4
store weight rms2 out sys equ

snf it 5 0 no sou dr 105 9999 best 6 < -5 rms > 5 rms
no plots
run

multi cal. Factor
```

```

cl
plot
write .btd + name of region
next

repl in-l out-l
read 1
convert comm
proj <hh:mm:ss> <dd:mm:ss>
ext <Ra> <Dec>
blc < $\Delta$ Ra> < $\Delta$ Dec>
pix 8 8
run all
quit

file out name of region.gdf
wri

cl
plo

exit

```

A.3 Third generation:

The creation of a source model is done by neglecting everything outside the polygon shaped from the final map of the second generation and then saving the image.

```

init in-l
init out-l

i-d name of input directory
o-d name of output directory

lis name of input list
lis
pause

for i 1 to last
read i

init gfit
init histo

del dc
del rc 2 12
init spike

pol name of polygon
base r out, sys equa proj <hh:mm:ss> <dd:mm:ss>

base t 5
base l 0

```

```
set mask
> 5 rms
< -5 rms
inter blan neigh 4 4
mask

base t 5
base l 0

set mask
deconv
mask

corr ge
tau tau 20000
corr ext

base t 5
base l 4
store weight rms2 out sys equ

snf
sou name of source model.gdf sb
dr 22 9999
best 6
< -5 rms > 5 rms
no plots
run

multi cal. Factor

cl
plot
write .btd +name of region
next

repl in-l out-l
read 1
convert comm
proj <hh:mm:ss> <dd:mm:ss>
ext <Ra> <Dec>
blc <ΔRa> <ΔDec>
pix 8 8
run all
quit

file out name of region.gdf
wri

cl
plo

exit
```

A.4 Fourth generation:

In a final step a similar reduction as in the third generation is executed. The modification in this step is that a source model which is obtained from the third generation is used.

References

- Albrecht, M., 2000, Ph.D. Thesis, Fakultät für Physik und Astronomie an der Ruhr-Universität Bochum
- Andre, P., Ward-Thompson, D., Barsony, M., 1993, *ApJ* 406, 122
- Assendorp, R., Bontekoe, Tj.R., de Jonge, A.R.W., Kester, D.J.M., Roelfsema, P.R., Wesselius, P.R., 1995, *A&AS* 110, 395
- Bally, J., 2002, *ASP-CS* 267,219
- Bazell, D., Dwek, E., 1990, *ApJ* 360, 142
- Berkhuijsen, E.M., Beck, R., Walterbos, R.A.M., 2000, *The Interstellar Medium in M31 and M33*, Shaker Verlag, Aachen, p.102
- Bloemen, J.B.G.M., Strong, A.W., Blitz, L., Cohen, R.S., Dame, T.M., Grabelsky, D.A., Hermsen, W., Lebrun, F., Mayer-Hasselwander, H.A., Thaddeus, P., 1986, *A&A* 154, 25
- Bolatto, A.D., Jackson, J.M., Israel, F.P., Zhang, X., Kim, S., 2000, *ApJ* 545, 234
- Bonnell, I.A., Bate, M.R., Zinnecker, H., 1998, *MNRAS* 298, 93
- Bonnell, I.A., Bate, M.R., Clarke, C.J., Pringle, J.E., 2001, *MNRAS* 323, 785
- Bontekoe, Tj.R., Koper, E., Kester, D.J.M., 1994, *A&A* 284, 1037
- Booth, R.S., Delgado, G., Hagström, M., Johansson, L.E.B., Murphy, D.C., Olberg, M., Whyborn, N.D., Greve, A., Hansson, B., Lindstroem, C.O., Rydberg, A., 1989, *A&A* 216, 315
- Boreiko, R.T., Betz, A.L., 1991, *ApJ* 380, L27
- Bouchet, P., Lequeux, J., Maurice, E., Prevot, L., Prevot-Burnichon, M.L., 1985, *A&A* 149, 330
- Boulanger, F., Perault, M., 1988, *ApJ* 330, 964
- Braine, J., Krügel, E., Sievers, A., Wielebinski, R., 1995, *A&A* 295, L55
- Brandl, B., Bertoldi, F., Sams, B.J., Eckart, A., Genzel, R., 1997, *RMxAA* 6, 126
- Brandner, W., Grebel, E.K., Barba, R.H., Walborn, N.R., Moneti, A., 2001, *ApJ* 122, 858
- Braun, M., Assendorp, R., Bontekoe, Tj.R., Kester, D.J.M., Richter, G., 1998, in: *The Magellanic Clouds and Other Dwarf Galaxies*, Shaker Verlag, Aachen, p.121
- Brooks, K.J., Whiteoak, J.B., 1997, *MNRAS* 291, 395
- Caldwell, J.A.R., Coulson, I.M., 1986, *MNRAS* 218, 223
- Caplan, J., Ye, T., Deharveng, L., Turtle, A.J., Kennicutt, R.C., 1996, *A&A* 307, 403
- Caswell, J.L., Haynes, R.F., 1981, *MNRAS* 194, 33P
- Caswell, J.L., 1995, *MNRAS* 272, L31
- Chin, Y.-N., Henkel, C., Whiteoak, J.B., Millar, T.J., Hunt, M.R., Lemme, C., 1997, *A&A* 317, 548

- Chin, Y.-N., Henkel, C., Millar, T.J., Whiteoak, J.B., Marx-Zimmer, M., 1998, *A&A* 330, 901
- Chini, R., 1989, *RvMA* 2, 180
- Chini, R., Krügel, E., Kreysa, E., Gemünd, H.-P., 1989, *A&A* 216, 5
- Chini, R., Krügel, E., Haslam, C.G.T., Kreysa, E., Lemke, R., Reipurth, B., Sievers, A., Ward-Thompson, D., 1993, *A&A* 272, L5
- Chini, R., Wargau, W.F., 1998, *A&A* 329, 161
- Chini, R., 2002, *Aufbau der Milchstrasse und Interstellares Medium, Vorlesung an der Ruhr-Universität Bochum, Wintersemester 2001/02*
- Chu, Y.-H., Kennicutt, R.C., 1988, *AJ* 96, 1874
- Chu, Y.-H., 1997, *AJ* 113, 1815
- Chu, Y.-H., Kennicutt, R.C., Snowden, S.L., Smith, R.C., Williams, R.M., Bomans, D.J., 1997, *PASP* 109, 554
- Cohen, R.S., Dame, T.M., Garay, G., Montani, J., Rubio, M., Thaddeus, P., 1988, *ApJ* 331, L95
- Contursi, A., Lequeux, J., Cesarsky, D., Boulanger, F., Rubio, M., Hanus, M., Sauvage, M., Tran, D., Bosma, A., Madden, S., Vigroux, L., 2000, *A&A* 362, 310
- Dall'Oglio, G., Andreani, P., Merluzzi, P., Piccirillo, L., Pizzo, L., Rossi, L., 1993, in: *New Aspects of Magellanic Cloud Research*, Springer Verlag, Berlin, p.169
- Danforth, C.W., Sankrit, R., Blair, W.P., Howk, J.C., Chu, Y.-H., 2003, *ApJ* 586, 1179
- Davies, R.D., Elliott, K.H., Meaburn, J., 1976, *Mem. RAS* 81, 89
- De Boer, K.S., Richter, P., Bomans, D.J., Heithausen, A., Koorneef, J., 1998, *A&A* 338, L5
- Deharveng, L., Caplan, J., 1991, *A&A* 259, 480
- De Marchi, G., Nota, A., Leitherer, C., Ragazzoni, R., Barbieri, C., 1993, *ApJ* 419, 658
- Dickey, J.M., Mebold, U., Stanimirovic, S., Staveley-Smith, L., 2000, *ApJ* 536, 756
- Dickman, R.L., 1975, *ApJ* 202, 50
- Draine, B.T., 1981, *ApJ* 245, 880
- Draine, B.T., Lee, H.M., 1984, *ApJ* 285, 89
- Draine, B.T., 1985, *ApJS* 57, 587
- Draine, B.T., Anderson, N., 1985, *ApJ* 292, 494
- Dufour, R.J., 1984, *IAUS* 108, 353
- Duley, W.W., Jones, A.P., Williams, D.A., 1989, *MNRAS* 236, 709
- Dyson, J.E., Williams, D.A., 1997, *The Physics of the Interstellar Medium*, IOP Publ., Bristol
- Eddington, A.S., 1937, *Observatory* 60, 99
- Elliott, K.H., Goudis, C., Meaburn, J., Tebbutt, N.J., 1977, *A&A* 55, 187
- Epchtein, N., Braz, M.A., Sevre, F., 1984, *A&A* 140, 67
- Fitzpatrick, E.L., Savage, B.D., 1984, *ApJ* 279, 578
- Fitzpatrick, E.L., 1986, *AJ* 92, 1068
- Forest, T.A., Spenny, D.L., Johnson, R.W., 1988, *PASP* 100, 683
- Fujimoto, M., Noguchi, M., 1990, *PASJ* 42, 505
- Fukui, Y., Abe, R., Hara, A., Hayakawa, T., Kato, S., Kawamura, A., Mizuno, A., Mizuno, N., Ogawa, H., Onishi, T., Saito, H., Tachihara, K., Xiao, K.C., Yamaguchi, N., Yamaguchi, R., Yonekura, Y., Rubio, M., 1999, *IAUS* 190, 61

- Gao, Y., Lo, K.Y., Lee, S.-W., Lee, T.-W., 2001, *ApJ* 548, 172
- Garay, G., Johansson, L.E.B., Nyman, L.-Å., Booth, R.S., Israel, F.P., Kutner, M.L., Lequeux, J., Rubio, M., 2002, *A&A* 389, 977
- Gatley, I., Becklin, E.E., Hyland, A.R., Jones, T.J., 1981, *MNRAS* 197, 17P
- Gordon, K.C., Kron, G.E., 1983, *PASP* 95, 461
- Gould, R.J., Salpeter, E.E., 1963, *ApJ* 138, 393
- Greve, A., Castles, J., McKeith, C.D., 1991, *A&A* 251, 575
- Guelin, M., Zylka, R., Mezger, P.G., Haslam, C.G.T., Kreysa, E., Lemke, R., Sievers, A.W., 1993, *A&A* 279, L37
- Gull, S.F., Skilling, J., 1991, *MEMSYS5 Users Manual*, Maximum Entropy Data Consultants Ltd., Suffolk
- Haynes, R.F., Klein, U., Wayte, S.R., Wielebinski, R., Murray, J.D., Bajaja, E., Meinert, D., Buczylowski, U.R., Harnett, J.I., Hunt, A.J., Wark, R., Sciacca, L., 1991, *A&A* 252, 475
- Heikkilä, A., Johansson, L.E.B., Olofsson, H., 1999, *A&A* 344, 817
- Hendrick, S.P., Reynolds, S.P., 2001, *ApJ* 559, 903
- Henize, K.G., 1956, *ApJS* 2, 315
- Herbig, G.H., 1962, *Adv. Astron. Astrophys.* 1, 47
- Herbig, G.H., 1970, *Mem. Soc. R. Sci. Liege*, 19, 13
- Heydari-Malayeri, M., Testor, G., 1982, *A&A* 111, L11
- Heydari-Malayeri, M., Rosa, M.R., Zinnecker, H., Deharveng, L., Charmandaris, V., 1999a, *A&A* 344, 848
- Heydari-Malayeri, M., Charmandaris, V., Deharveng, L., Rosa, M.R., Zinnecker, H., 1999b, *A&A* 347, 841
- Heydari-Malayeri, M., Charmandaris, V., Deharveng, L., Meynadier, F., Rosa, M.R., Schaerer, D., Zinnecker, H., 2002, *A&A* 381, 941
- Heydari-Malayeri, M., Meynadier, F., Charmandaris, V., Deharveng, L., Le Bertre, T., Rosa, M.R., Schaerer, D., 2003, *A&A* 411, 427
- Hildebrand, R.H., 1983, *QJRAS* 24, 267
- Hill, J.K., Bohlin, R.C., Cheng, K.-P., Fanelli, M.N., Hintzen, P., O'Connell, R.W., Roberts, M.S., Smith, A.M., Smith, E.P., Stecher, T.P., 1993, *ApJ* 413, 604
- Hindman, J.V., 1964, *IAUS* 20, 255
- Hodge, P.W., Wright, F.W., 1967, *The Large Magellanic Cloud*, Smithsonian Press, Washington
- Hodge, P.W., 1974, *PASP* 86, 263
- Hodge, P.W., Wright, F.W., 1974, *AJ* 79, 858
- Hodge, P.W., 1985, *PASP* 97, 530
- Hodge, P.W., 1988, *PASP* 100, 346
- Hollenbach, D.J., Werner, M.W., Salpeter, E.E., 1971, *ApJ* 163, 165
- Hubble news release, 2002-12
- Huggins, P.J., Gillespie, A.R., Phillips, T.G., Gardner, F., Knowles, S., 1975, *MNRAS* 173, 69P
- Hunter, D.A., 1992, in: *Star Formation in Stellar Systems*, Cambridge Univ. Press, Cambridge, p.67
- Hunter, D.A., Shaya, E.J., Holtzman, J.A., Light, R.M., O'Neil E.J., Lynds, R., 1995, *ApJ* 448, 179

- Hyland, A.R., Straw, S., Jones, T.J., Gatley, I., 1992, MNRAS 257, 391
- Israel, F.P., De Graauw, T., Van de Stadt, H., De Vries, C.P., 1986, ApJ 303, 186
- Israel, F.P., Koornneef, J., 1988, A&A 190, 21
- Israel, F.P., De Graauw, T., 1991, IAUS 148, 45
- Israel, F.P., Maloney, P.R., 1993, in: *New Aspects of Magellanic Cloud Research*, Springer Verlag, Berlin, p.44
- Israel, F.P., Johansson, L.E.B., Lequeux, J., Booth, R.S., Nyman, L.-A., Crane, P., Rubio, M., De Graauw, Th., Kutner, M.L., Gredel, R., Boulanger, F., Garay, G., Westerlund, B., 1993, A&A 276, 25
- Israel, F.P., 1997, A&A 328, 471
- Israel, F.P., de Graauw, T., Johansson, L.E.B., Booth, R.S., Boulanger, F., Garay, G., Kutner, M.L., Lequeux, J., Nyman, L.-A., Rubio, M., 2003, A&A 401, 99
- Johansson, L.E.B., 1991, IAUS 146, 1
- Johansson, L.E.B., Greve, A., Booth, R.S., Boulanger, F., Garay, G., De Graauw, Th., Israel, F.P., Kutner, M.L., Lequeux, J., Murphy, D.C., Nyman, L.-A., Rubio, M., 1998, A&A 331, 857
- Johansson, L.E.B., 2002, priv. comm.
- Johnston, M.D., Bradt, H.V., Doxsey, R.E., Gursky, H., Schwartz, D.A., Schwartz, J., Van Paradijs, J., 1978, ApJ 225, L59
- Jones, T.J., Hyland, A.R., Straw, S., Harvey, P.M., Wilking, B.A., Joy, M., Gatley, I., Thomas, J.A., 1986, MNRAS 219, 603
- Kahabka, P., de Boer, K.S., Brüns, C., 2001, A&A 371, 816
- Kennicutt, R.C., Hodge, P.W., 1986, ApJ 306, 130
- Kennicut, R.C., Bresolin, F., Bomans, D.J., Bothun, G.D., Thompson, I.B., 1995, ApJ 109, 594
- Kim, S., 1998, A&AS 193, 1287
- Kim, S., Chu, Y.-H., Staveley-Smith, L., Smith, R.C., 1998, ApJ 503, 729
- Klein, U., priv. comm.
- Knapp, G.R., 2001, ASP Conf. Series 231, 127
- Koornneef, J., Code, A.D., 1981, ApJ 247, 860
- Koornneef, J., 1982, A&A 107, 247
- Kreysa, E., Gemünd, H.-P., Gromke, J., Haslam, C.G.T., Reichertz, L., Haller, E.E., Beeman, J.W., Hansen, V., Sievers, A., Zylka, R., 1998, Proc. SPIE 3357, 319
- Kreysa, E., Beeman, J.W., Haller, E.E., priv. comm.
- Krügel, E., Chini, R., Kreysa, E., Sherwood, W.A., 1988, A&A 190, 47
- Krügel, E., Siebenmorgen, R., 1994, A&A 288, 929
- Kurt, C.M., Dufour, R.J., Garnett, D.R., Skillman, E.D., Mathis, J.S., Peimbert, M., Torres-Peimbert, S., Ruiz, M.-T., 1999, ApJ 518, 246
- Kutner, M.L., Rubio, M., Booth, R.S., Boulanger, F., De Graauw, Th., Garay, G., Israel, F.P., Johansson, L.E.B., Lequeux, J., Nyman, L.-A., 1997, A&ASS 122, 255
- Lada, C.J., Wilking, B.A., 1984, ApJ 287, 610
- Lada, C.J., 1987, IAUS 115, 1

- Lada, C.J., 1999, in: *The Origin of Stars and Planetary Systems*, Kluwer Acad. Publ., Dordrecht, p.143
- Lequeux, J., Le Bourlot, J., Pineau des Forets, G., Roueff, E., Boulanger, F., Rubio, M., 1994, *A&A* 292, 371
- Li, A., Greenberg, J.M., 1997, *A&A* 323, 566
- Lindsay, E.M., 1958, *MNRAS* 118, 172
- Lortet, M.-C., Testor, G., 1984, *A&A* 139, 330
- Lucke, P.B., Hodge, P.W., 1970, *AJ* 75, 171
- Lucke, P.B., 1974, *ApJS* 28, 73
- Luks, Th., Rohlf, K., 1992, *A&A* 263, 41
- MacLaren, I., Richardson, K.M., Wolfendale, A.W., 1988, *ApJ* 333, 821
- Maeder, A., Behrend, R., 2002, *ASP-CS* 267, 179
- Malamuth, E.H., Heap, S.R., 1994, *AJ* 107, 1054
- Maloney, P., 1990, *ApJ* 348, L9
- Marshall, F.E., Gotthelf, E.V., Zhang, W., Middleditch, J., Wang, Q.D., 1998, *ApJ* 499, 179
- Martins, F., Schaerer, D., Heydari-Malayeri, M., 2003, *IAUS* 212, 564
- Marx, M., Dickey, J.M., Mebold, U., 1997, *A&AS* 126, 325
- Marx-Zimmer, M., Herbstmeier, U., Dickey, J.M., Zimmer, F., Staveley-Smith, L., Mebold, U., 2000, *A&A* 354, 787
- Massey, P., Parker, J.W., Garmany, C.D., 1989, *AJ* 98, 1305
- Mathewson, D.S., Ford, V.L., 1984, *IAUS* 108, 125
- Mathis, J.S., Ruml, W., Nordsieck, K.H., 1977, *ApJ* 217, 425
- Mathis, J.S., Mezger, P.G., Panagia, N., 1983, *A&A* 128, 212
- Mathis, J.S., Whiffen, G., 1989, *ApJ* 341, 808
- McGee, R.X., Brooks, J.W., Batchelor, R.A., 1972, *Austr. J. Phys* 25, 581
- Meaburn, J., 1980, *MNRAS* 192, 365
- Meaburn, J., Marston, A.P., McGee, R.X., Newton, L.M., 1987, *MNRAS* 225, 591
- Meaburn, J., Laspas, V.N., 1991, *A&A* 245, 635
- Meikle, W.P.S., Spyromilio, J., Allen, D.A., Varani, G.-F., Cumming, R.J., 1993, *MNRAS* 261, 535
- Melnick, J., 1985, *A&A* 153, 235
- Mezger, P.G., Smith, L.F., 1977, *IAUS* 75, 133
- Mills, B.Y., Turtle, A.J., Watkinson, A., 1978, *MNRAS* 185, 263
- Nandy, K., Morgan, D.H., Willis, A.J., Wilson, R., Gondhalekar, P.M., 1981, *MNRAS* 196, 955
- Naze, Y., Hartwell, J.M., Stevens, I.R., Corcoran, M.F., Chu, Y.-H., Königsberger, G., Moffat, A.F.J., Niemela, V.S., 2002, *ApJ* 580, 225
- Nielbock, M., Chini, R., Jütte, M., Manthey, E., 2001, *A&A* 377, 273
- Oey, M.S., Massey, P., 1995, *ApJ* 452, 210
- Ossenkopf, V., 1993, *A&A* 280, 617
- Papoular, R., Guillois, O., Nenner, I., Reynaud, C., 1995, *A&A* 293, 562

- Parker, J.W., Garmany, 1993, AJ 106, 1471
- Peck, A.B., Goss, W.M., Dickel, H.R., Roelfsema, P.R., Kesteven, M.J., Dickel, J.R., Milne, D.K., Points, S.D., 1997, ApJ 486, 329
- Pei, Y.C., 1992, ApJ 395, 130
- Rapley, C.G., Tuohy, I.R., 1974, ApJ 191, L113
- Reach, W.T., Dwek, E., Fixsen, D.J., Hewagama, T., Mather, J.C., Shafer, R.A., Banday, A.J., Bennett, C.L., Cheng, E.S., Eplee Jr., R.E., Leisawitz, D., Lubin, P.M., Read, S.M., Rosen, L.P., Shuman, F.G.D., Smoot, G.F., Sodroski, T.J., Wright, E.L., 1995, ApJ 451, 188
- Reichert, L.A., Weferling, B., Esch, W., Kreysa, E., 2001, A&A 379, 735
- Richter, P., Widmann, H., De Boer, K.S., Appenzeller, I., Barnstedt, J., Goelz, M., Grewing, M., Gringel, W., Kappelmann, N., Krämer, G., Mandel, H., Werner, K., 1998, A&A 338, L9
- Richter, P., De Boer, K.S., Bomans, D.J., Chin, Y.-N., Heithausen, A., Koornneef, J., 1999, A&A 351, 323
- Richter, P., 2000, A&A 359, 1111
- Rodrigues, C.V., Magalhaes, A.M., Coyne, G.V., Pirola, V., 1997, ApJ 485, 618
- Rossa, J., 2001, Ph.D. Thesis, Fakultät für Physik und Astronomie an der Ruhr-Universität Bochum
- Rownd, B.K., Young, J.S., 1999, AJ 118, 670
- Rubio, M., Roth, M., Tapia, M., 1990, RMxAA 21, 249
- Rubio, M., Garay, G., Montani, J., Thaddeus, P., 1991, ApJ 368, 173
- Rubio, M., Roth, M., Garcia, J., 1992, A&A 261, L29
- Rubio, M., Lequeux, J., Boulanger, F., Booth, R.S., Garay, G., De Graauw, Th., Israel, F.P., Johansson, L.E.B., Kutner, M.L., Nyman, L.-A., 1993, A&A 271, 1
- Rubio, M., Lequeux, J., Boulanger, F., 1993, A&A 271, 9
- Rubio, M., Lequeux, J., Boulanger, F., Booth, R.S., Garay, G., De Graauw, Th., Israel, F.P., Johansson, L.E.B., Kutner, M.L., Nyman, L.-A., 1996, A&AS 118, 263
- Rubio, M., 1997, IAUS 170, 265
- Rubio, M., Barba, R.H., Walborn, N.R., Probst, R.G., Garcia, J., Roth, M.R., 1998, ApJ 116, 1708
- Rubio, M., Contursi, A., Lequeux, J., Probst, R., Barba, R., Boulanger, F., Cesarsky, D., Maoli, R., 2000, A&A 359, 1139
- Rubio, M., 2002, priv.comm.
- Sakata, A., Wada, S., Onaka, T., Tokunaga, A.T., 1987, ApJ 320, L63
- Sandford, S.A., 1996, M&PS 31, 449
- Sauvage, M., Vigroux, L., 1991, IAUS 148, 407
- Sauvage, M., 1997, in: The Interstellar Medium in Galaxies, Kluwer Acad. Publ., Dordrecht, p.1
- Savage, B.D., Mathis, J.S., 1979, ARA&A 17, 73
- Savage, B.D., De Boer, K.S., 1981, ApJ 243, 460
- Scalise, E., Braz, M.A., 1981, Nature, 290, 36
- Scalo, J.M., 1986, Fundam. Cosmic Phys. 11, 1
- Schild, H., Testor, G., 1992, A&AS 92, 729
- Schlegel, D.J., Finkbeiner, D.P., Davis, M., 1998, ApJ 500, 525

- Schwering, P.B.W., 1988, Ph.D. Thesis, Rijksuniversiteit te Leiden
- Schwering, P.B.W., Israel, F.P., 1990, Atlas and Catalogue of Infrared Sources in the Magellanic Clouds, Kluwer Acad. Publ., Dordrecht
- Sellgren, K., Allamandola, L.J., Bregman, J.D., Werner, M.W., Wooden, D.H., 1985, ApJ 299, 416
- Siebenmorgen, R., Krügel, E., 1992, A&A 259, 614
- Sievers, A.W., Reuter, H.-P., Haslam, C.G.T., Kreysa, E., Lemke, R., 1994, A&A 281, 681
- SIMBA Observers Handbook, 2002, version 1.8
- Solomon, P.M., Sanders, D.B., 1985, in: Protostars and Planets II, Univ. Arizona Press, Tucson, p.81
- Sorai, K., Hasegawa, T., Booth, R.S., Rubio, M., Morino, J.-I., Bronfman, L., Handa, T., Hayashi, M., Nyman, L.-A., Oka, T., Sakamoto, S., Seta, M., Usuda, K.S., 2001, ApJ 551, 794
- Stanimirovic, S., 1999, Ph.D. Thesis, University of Western Sydney Nepean
- Staveley-Smith, L., Sault, R.J., McConnell, D., Kesteven, M.J., Hatzidimitriou, D., Freeman, K.C., Dopita, M.A., 1995, PASAu 12, 13
- Strömgren, B., 1939, ApJ 89, 526
- Takahashi, J., Masuda, K., Nagaoka, M., 1999, MNRAS 306, 22
- Testor, G., Pakull, M., 1985, A&A 145, 170
- Testor, G., Lortet, M.-C., 1987, A&A 178, 25
- Testor, G., Niemela, V., 1998, A&AS 130, 527
- Testor, G., Rola, C.S., Whiting, A.B., 1999, IAUS 190, 132
- Thum, C., Kreysa, E., John, D., Gemuend, H.-P., Brunswig, W., Greve, A., Haslam, G., Lemke, R., Reuter, H.P., Ruiz, M., Sievers, A., Steppe, H., 1992, IRAM Working Report 212/92
- Torres, G., Carranza, G.J., 1987, MNRAS 226, 513
- Vermeij, R., Peeters, E., Tielens, A.G.G.M., Van der Hulst, J.M., 2002, A&A 382, 1042
- Walborn, N.R., Blades, J.C., 1987, ApJ 323, L65
- Walborn, N.R., 1991, in: Massive Stars in Starbursts, Cambridge Univ. Press, Cambridge, p. 145
- Walborn, N.R., Blades, J.C., 1997, ApJS 112, 457
- Walborn, N.R., Barba, R.H., Brandner, W., Rubio, M., Grebel, E.K., Probst, R.G., 1999, ApJ 117, 225
- Wang, Q., Helfand, D.J., 1991, ApJ 370, 541
- Watson, W.D., Salpeter, E.E., 1972, ApJ 174, 321
- Westerlund, B.E., 1997, The Magellanic Clouds, Cambridge Univ. Press, Cambridge
- Wheelock, S.L., Gautier, T.N., Chillemi, J., Kester, D., McCallon, H., Oken, C., White, J., Gregorich, D., Boulanger, F., Good, J., 1994, IRAS Sky Survey Atlas Explanatory Supplement (ISSA), JPL 94-11
- Whiteoak, J.B., Gardner, F.F., 1986, MNRAS 222, 513
- Whittet, D.C.B., 1991, Dust in the Galactic Environment, Inst. of Phys. Publ., Philadelphia
- Wilke, K., Stickel, M., Haas, M., Herbstmeier, U., Klaas, U., Lemke, D., 2003, A&A 401, 873
- Wiling, B.A., Lada, C.J., 1983, ApJ 274, 698
- Xu, C., Klein, U., Meinert, D., Wielebinski, R., Haynes, R.F., 1992, A&A 257, 47

- Ye, T., Turtle, A.J., Kennicutt, R.C., 1991, MNRAS 249, 722
Yorke, H.W., Sonnhalter, C., 2002, ApJ 569, 846
Zhang, X., Wright, M., Alexander, P., 1993, ApJ 418, 100
Zinnecker, H., 2003, IAUS 212, 80

Acknowledgements

First of all, I owe many thanks to Prof. Dr. Rolf Chini, my Ph.D. thesis supervisor, who allowed me to start and perform this project. My gratitude to him for giving me freedom regarding the contents of my Ph.D. thesis, as well as for the new insights in the world of Astrophysics.

Particularly I wish to thank Prof. Dr. Ulrich Mebold, for acting as the second referee for this Ph.D. thesis.

I am also grateful to the GK "The Magellanic System, Galaxy Interaction and the Evolution of Dwarf Galaxies" for its financial support. And the ESO, for making possible the observing trips to La Silla/Chile.

In relation to the bolometer's observations, I wish to thank Dr. Lars E.B. Johansson who provided me with part of the SMC's data, as well as Dr. Marcus Albrecht and Zita Banhidi who carried out part of my first and fourth observing run of the SIMBA survey at SEST. Also, my thanks to the SEST's staff, specially Dr. Markus Nielbock, for their competent support.

Special thanks goes also to Dr. Michael Braun who provided me with the MCs' IRAS maps.

Many thanks to my office-mates, Dr. Marcus Albrecht and Katrin Kämpgen, for the motivating working atmosphere. I am grateful to Dr. Marcus Albrecht for the enlightening discussions on various topics, which I have covered in my Ph.D. thesis.

For solving problems associated with LINUX, I thank Dr. Sven Müller.

I also wish to express my thanks to all AIRUB colleagues, who contributed to the good working atmosphere during the last three years.

Last but not least, I want to thank my parents and my grandmother for their continuing support in my professional life.

Curriculum Vitae

Name: Elisa Merkel Ferreira
Date of birth: 10.03.1975
Place of birth: Recife, Brazil

School education

Elementary school: 1981 - 1985 (Recife)
Secondary school: 1986 - 1992 (Recife)

Undergraduate studies: Physics at the Universidade Federal de Pernambuco (UFPE)
Recife (1993 - 1996)

Graduate studies

Master thesis: *Estudo da absorcao de radiacao de baixas frequências em $YBa_2Cu_3O_{7-\delta}$ dopado com MS ($M = Fe, Ni$ ou Zn)*
(Low frequency absorption study in $YBa_2Cu_3O_{7-\delta}$ doped with MS ($M = Fe, Ni$ or Zn))
at the UFPE/Recife (1997 - 1999)

Thesis supervisor: Prof. Dr. Jose Marcilio Ferreira
Ph.D. thesis: *Star Formation in the Magellanic Clouds based on 1.2 mm Continuum Observations*
at the Astronomisches Institut der Ruhr-Universität Bochum
(2000 - 2004)

Thesis supervisor: Prof. Dr. Rolf Chini, second referee: Prof. Dr. Ulrich Mebold
Research stays: Chile, USA
Observing runs: European Southern Observatory-SEST/Chile

I sincerely claim, to my best knowledge, that I have independently done this Ph.D. thesis
and have not used other resources than those given credit.

Bochum, May 6, 2004 Elisa Merkel Ferreira